NANYANG TECHNOLOGICAL UNIVERSITY

TUNING STRUCTURES AND MORPHOLOGY OF M_OS_2/CARBON NANOCOMPOSITES FOR THEIR APPLICATIONS AS LITHIUM-ION BATTERY ANODE

ZHAO CHENYANG

SCHOOL OF MATERIALS SCIENCE AND ENGINEERING

2016

TUNING STRUCTURES AND MORPHOLOGY OF M_OS_2/CARBON NANOCOMPOSITES FOR THEIR APPLICATIONS AS LITHIUM-ION BATTERY ANODE

ZHAO CHENYANG

SCHOOL OF MATERIALS SCIENCE AND ENGINEERING

A thesis submitted to the Nanyang Technological University
in partial fulfilment of the requirement for the degree of
Doctor of Philosophy

2016

Statement of Originality

I hereby certify that the work embodied in this thesis is the result of original research and has not been submitted for a higher degree to any other University or Institution.

12/12/2016
.....
Date

Zhao CY
.....
Student Name

Abstract

In recent years, lithium ion batteries (LIBs) have attracted more and more attention due to the high energy density, low gravimetric density, long cycle life and flexible design. The fast-growing market for portable electronic devices and the development of hybrid electric vehicles create a strong driving force for the development of advanced anode materials, because the commercial anode material, graphite, has a theoretical specific capacity of only 372 mAh/g, which is too low to meet the rising demands of these new applications. As an analogue of graphite, molybdenum disulfide (MoS_2) shows great promise as an alternative in virtue of its predominant merits in capacity and relatively small volume change in cycling. MoS_2, however, suffers from sluggish kinetics due to its semiconductor nature, especially along the direction perpendicular to the basal plane, leading to unsatisfied rate capability. In addition, the shuttle effect caused by the soluble intermediates, polysulfides (PS), results in a loss of active material and continuous capacity decay.

Aimed to overcome the inherent weaknesses of MoS_2-based anodes (sluggish kinetics and capacity fading), in my PhD work, ultrathin MoS_2 nanosheets and their hybrids are prepared through novel morphology and structure design. The effects of layer number, interlayer distance, conductive additive (carbon) and crystal interfaces on the electrochemical properties of MoS_2 are investigated.

First, the effect of layer number is studied by aqueous exfoliation of MoS_2 with the aid of alkali lignin (AL), a low-cost, environmentally benign and bio-renewable feedstock. It is found that, AL has strong stabilization effect on MoS_2 nanosheets, as well as other two dimensional (2D) materials. The stabilization mechanism and disperse conditions of AL are explored. Compared to bulk MoS_2, the exfoliated MoS_2 nanosheets exhibit improved electrochemical performance both as cathode and anode. However, their cycling stability is still not satisfied as the dissolution of PS is inevitable.

In order to confine the active materials, disordered graphene-like MoS_2 nanosheets are embedded in amorphous carbon nanofibers through hydrothermal treatment and electrospinning. The obtained binder-free, self-standing nanofibrous mats can be directly used as anodes after simply punching into suitable size and shape. The hydrothermally

synthesized MoS_2 exhibits expanded interlayer spacing, which accommodates extra Li^+ and improves the Li^+ storage capacity. The carbon mats alleviates the loss of PS, leading to excellent cycling stability. What's more, thanks to the electrospinning technique and 2D layered structure of MoS_2, high flexibility of the hybrid mats are achieved, enabling realization of diverse flexible devices.

Nevertheless, the rate performance of the hybrid mats is still limited by the thick carbon shell and MoS_2 nanosheets. To further increase the electronic and ionic diffusion, single-layer MoS_2 (SL-MoS_2) with specially designed architecture is of great potential. Based on the coordination chemistry, a universal method for the fabrication of defect-rich, ultrafine crystals in carbon matrix is developed. Unique SL-MoS_2/C sandwich structure is facilely prepared by simply mixing dopamine (DOPA) and Na_2MoO_4 aqueous solutions, followed by hydrothermal treatment and annealing. The coordination complex formed between DOPA and Mo^{VI} is found crucial for the formation of the unique structure. The structural features of the nanocomposites, large interlayer spacing, sandwich structure and crumpled naosheet morphology, render the SL-MoS_2/C an excellent anode material, showing a reversible capacity of 500 mAh/g at 5 A/g.

The engineering of SL-MoS_2 with 2D carbon sheet is fascinating and may generate new class nanocomposite with idea atomic interface for high capacity and rate capability. In this regard, an electrostatic attraction-induced self-assembly strategy is developed for the fabrication of nitrogen-doped graphene (NDG)/MoS_2 nanocomposite with well-defined alternating structure (van der Waals heterostructure). The maximized atomic contact triggers synergistic effect between the two components, endowing the NDG/MoS_2 nanocomposite with low charge-transfer resistance, high sulfur reservation and structural robustness. A reversible capacity of 820 mAh/g can be achieved at 1 A/g after high-rate charge-discharge. This self-assembly approach may also be adopted for surface modification of MoS_2 or fabrication of other NDG intercalated 2D materials.

In summary, the electrochemical properties of MoS_2 could be greatly improved by reducing the layer number, increasing interlayer distance, adding conductive and protective additive and creating interfaces. The knowledge obtained from this work provides useful insights for further studies on MoS_2 or other metal sulfides as LIB anodes.

Acknowledgements

First of all, I would like to express my heartfelt gratitude to my supervisor, Associate Professor Lu Xuehong, for her great guidance during my PhD study. I am very lucky to join her group and spent wonderful four years here.

I would like to sincerely thank my co-supervisor Dr. Liu Zhao Lin from Institute of Materials Research and Engineering (IMRE), A-STAR. His wealth of knowledge really impressed me and I learned a lot from the conversation with him.

I would also like to sincerely thank my thesis advisory committee members, Dr. Long Yi, Associate Professor Alex Yan for their precious suggestions and time for the examination.

I would like to extend my sincere thankfulness to my lab mates, including Liping, Junhua, Wu Aik, Silei, Joan, Bai Yu, Guoqiang, Zhou Dan, Wanshuang, Chuanxiang, Jinlin, Zhou Rui, Ling Han, Yuliang, Huang Shu, Boyang, Fenggui, Huiqing, Xiayin, Xiaosheng Jia Ming, Ismail, Shanxin and those who ever worked with me, including Yuefan, Li Bing, Wang Xu, Xiaoming, Jingwei, Shaohui, Chen Ye, Yubin, etc., for their great support and assistance in progressing my PhD project.

My great appreciation also goes to Dr. Li Shuzhou, Dr. Huang Yizhong, Dr. Chen Zhong and many more who ever gave me kind help. The technical and administrative teams of MSE are the best I ever met. Thanks for their kind assistance of my study.

Family is always the most important for me. I would like to give my deepest gratitude to my parents, Mr. Zhao Qingchun and Ms. Li Xiulan and also my fiancée Misss Xie shuying, who always stand firm behind me no matter what happens. Their love is my power to move forward.

Table of Contents (Times New Roman, Size 14)

Table Captions

Figure Captions

were prepared by ultrasonic treatment for 5 h and centrifugation at 2000 rpm for 1 h. The concentration of AL was 0.5 mg mL^{-1}. The feed contents of bulk WS_2 and BN were 5 mg mL^{-1}.

Figure 5.1 Schematics showing the fabrication process for the highly flexible free-standing MoS_2/C nanofibrous mats. The sample in the picture contains 47% MoS_2.

Figure 5.2 Repeated bending tests of (a) the neat carbon mat and (b) MoS_2/C-95 hybrid mat.

Figure 5.3 (a, b) TEM images and (c) XRD patterns of the hydrothermally synthesized MoS_2 nanoflakes; the inset in (b) shows the corresponding SAED pattern.

Figure 5.4 (a) XRD patterns and (b) TGA curves of MoS_2/C-47, MoS_2/C-73 and MoS_2/C-95.

Figure 5.5 SEM (left, as-spun; middle, carbonized) and TEM (right) images of the hybrid nanofibers. The final MoS_2 contents for (a), (b) and (c) are 47, 73 and 95 wt%, respectively.

Figure 5.6 (a) Cyclic voltammograms of MoS_2/C-47 between 0.01 V and 3.0 V at a scan rate of 0.1 mV/s, (b) Discharge–charge profiles of MoS_2/C-47 for the 1^{st}, 2^{nd}, 10^{th}, 50^{th} and 100^{th} cycles, (c) cycling performances of MoS_2/C-47, MoS_2/C-73 and MoS_2/C-95 at current density of 50 mA/g and (d) rate capabilities of the three samples.

Figure 5.7 (a) Cyclic voltammograms between 0.01 V and 3.0 V at a scan rate of 0.1 mV/s and (b) cycling performances at current density of 50 mA/g of the neat electrospinning-derived carbon mat.

Figure 5.8 Cycling performances of MoS_2 nanoflake and MoS_2 powder electrodes prepared by casting. Both electrodes suffered rapid capacity fading due to structure destruction on cycling. However, the MoS_2 nanosheets showed a higher capacity at all cycles due to the larger interlayer spacing.

Figure 5.9 Nyquist plot of MoS_2/C-47, MoS_2/C-73 and MoS_2/C-95 measured at OCPs (a) before and (b) after cycles.

Figure 5.10 SEM (left) and TEM (right) images of (a) MoS_2/C-47 and (b) MoS_2/C-95 after the cycling test.

Abbreviations

LIBs	Lithium ion batteries
1D	One dimensional
2D	Two dimensional
3D	Three dimensional
MoS_2	Molybdenum disulfide
Mo	Molybdenum
SL-MoS_2	Single-layer MoS_2
FTIR	Fourier Transform Infrared Spectroscopy
TEM	Transmission Electron Microscopy
XRD	X-ray Diffraction
SAED	Selected Area Electron Diffraction
SEM	Scanning Electron Microscope
XPS	X-Ray Photoelectron Spectroscopy
TGA	Thermogravimetric Analysis
CV	Cyclic Voltammetry
EIS	Electrochemical Impedance Spectroscopy
GCD	Galvanostatic charge/discharge
NMP	N-methyl-2-pyrrolidone
TMD	Transition metal dichalcogenide
S	Sulfur
Li_2S	Lithium sulfide
CNF	Carbon nanofibers
GO	Graphene oxide
DOPA	Dopamine
DOPA-HCl	Dopamine.hydrochloride
PDOPA	Polydopamine
NDG	*N*-doped graphene
n-BuLi	N-Butyllithium
$LiBH_4$	Lithium borohydride
ATM	Ammonium thiomolybdate

Ar	Argon
H_2	Hydrogen
DMF	Dimethylformamide
CVD	Chemical vapor deposition
V	V *versus* Li/Li^+
CNT	Carbon nanotube
PVP	Poly(vinylpyrrolidone)
PEO	Poly(ethylene oxide)
PAN	Polyacrylonitrile
TAA	Thioacetamide
Na_2MoO_4	Sodium molybdate dehydrate
$Na_2WO_4.2H_2O$	Sodium tungstate dihydrate
$FeCl_3.6H_2O$	Ferric chloride hexahydrate
AL	Alkali lignin
WS_2	Tungsten disulfide
BN	Boron nitride
DMC	DOPA-Mo^{VI} complex
SEI	Solid electrolyte interphase

Chapter 1

Introduction

In this chapter, firstly the rationale for selection of MoS_2 as alternative anode material (predominant merits in capacity and relatively small volume change in cycling) for the lithium ion batteries (LIBs) and the problems (sluggish kinetics and capacity fading) that MoS_2-based anodes are facing are introduced. On the basis of above, the objectives and scope of my PhD work, as well as the organization of the thesis are presented, followed by a highlight of the main findings and outcomes of this work.

1.1 Problem Statement and Hypothesis

1.1.1 Problem statement

With the continuous depletion of oil, energy and environment crises become the top global problems faced by our society. The fast-growing market for portable electronic devices and the development of hybrid electric vehicles require the use of clean energy storage and conversion devices at a much higher level than that are presently in force. This calls for intensive research efforts in developing high-performance energy materials and devices.

Among various established energy-storage techniques, lithium-ion batteries (LIBs) have received greatly increased attention from both the academic and the industrial world because of their high energy density, low gravimetric density, long cycle life, and flexible design. According to the reaction mechanism with Li^+, the storage modes of electrode materials can be categorized into insertion, alloying, conversion (redox reaction) and interfacial storage. The commercial LIB anode material, graphite, is based on the insertion storage of Li^+, showing a theoretical specific capacity of only 372 mAh/g, which is too low to meet the rising demands for the emerging applications. By contrast, the electrode materials based on both conversion and interfacial storage of Li^+ show great promise as alternatives in virtue of their predominant merits in capacity. [1-3] Among them, molybdenum disulfide (MoS_2) has attracted great attention owing to its tunable structures and multiple Li^+ storage behaviors.[4-8]

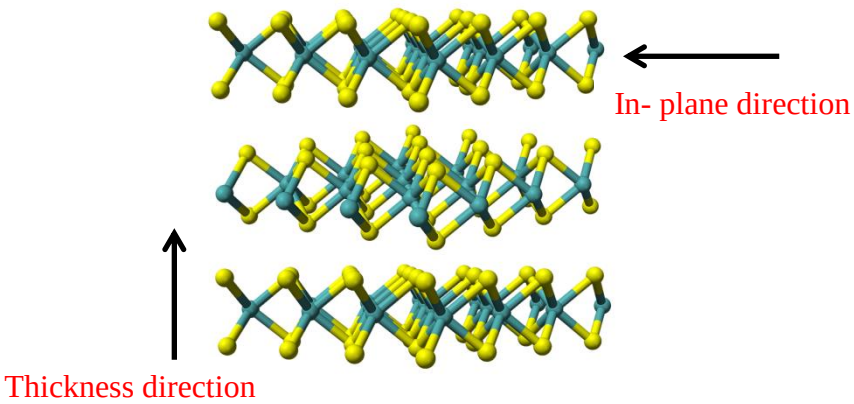

Figure 1.1 Structure illustration of MoS_2.

As a typical transition metal dichalcogenide (TMD), MoS_2 has two-dimensional (2D) layered structure, analogous to that of graphite. The covalent bonded S-Mo-S three atom layers are stacked together through van der Waals forces with an interlayer distance of 0.62 nm (Figure 1.1). Such structural features facilitate the insertion and extraction of foreign species,[9] making MoS_2 an attractive host material for energy storage.[10-13] In addition to insertion, MoS_2 can be converted to Mo and Li_2S when further discharged, leading to a substantial gain in capacity resulting from the conversion and interfacial storage of Li^+.[14-16]

$$MoS_2 + Li^+ + e^- = LiMoS_2 \quad (1.1)$$

$$LiMoS_2 + 3Li^+ + 3e^- = 2Li_2S + Mo \quad (1.2)$$

Volumetric expansion is a common problem that limits the cycling stability of electrode materials, which causes degradation and even pulverization of electrodes. Compare to other emerging anode materials, silicon for example, the expansion of MoS_2 is "only" 103%, which is quite attractive from a practical perspective.

Nevertheless, MoS_2 suffers from sluggish kinetics due to its semiconductor nature, especially along the thickness direction, leading to unsatisfied rate capabilities. In addition, as can be seen from equation 1.2, MoS_2 converts to a mixture of lithium sulfide and Mo metal after the first cycle, and the Li_2S/ sulfur (S) couple dominates the redox process in the following cycles.[17]

$$S + 2Li^+ + 2e^- \leftrightarrow Li_2S \quad (1.3)$$

Thus, similar to the lithium-sulfur batteries, the shuttle effect caused by the soluble polysulfide intermediates will result in a loss of active material and continuous capacity decay during repeated charge/discharge.[18,19]

1.1.2 Hypothesis

Since the bulk MoS_2 displays limited rate capabilities and cycling stability, its single-layer or multilayered counterparts are the focus of our attention. Similar to graphite, the properties of MoS_2 are thickness dependent. For example, bulk MoS_2 is an n-type semiconductor with an indirect band gap of ~1.2 eV, while single-layer MoS_2 is a direct-band gap semiconductor with a gap of ~1.8 eV.[20,21] The fundamental property change

from graphite to graphene has inspired us to investigate the electrochemical properties of ultrathin MoS_2 nanosheets. The lithium storage properties of the single-layer or multilayered MoS_2 will be much enhanced compared to its bulk equivalents due to the large surface area, short diffusion length in the thickness direction as well as the abundant voids and defects at the interfaces.

Liquid-phase exfoliation is a suitable route for large scale production of MoS_2 nanosheets, especially in environmental friendly solvent, for example, the water. Due to its hydrophobic nature, however, exfoliation of MoS_2 in in aqueous media is quite challenging. The electrochemical properties of aqueous exfoliated MoS_2 are seldom reported. Therefore, the study of aqueous exfoliation of MoS_2 as well as its application in the LIBs is of great significance in both academic and industry. It is hypothesized the addition of surfactant will greatly increase the exfoliation efficiency and the stability of the MoS_2 dispersion. Lignin, which is the second abundant polymer in nature, may be a promising candidate due to its good affinity, charged molecule and low cost.

Besides reducing the number of layers, the electron and Li^+ transports of MoS_2 can also be largely meliorated by integrating with carbonaceous materials[22-25] or conductive polymers[26,27] to fabricate nanocomposites with specially designed architectures. Electrospinning, a powerful technique for mass production of nanofibers, is an attractive approach for large-scale fabrication of one-dimensional (1D) hybrid carbon nanofibers (CNF). The features of electrospun-derived CNF, such as high aspect ratio and large surface area, render the obtained hybrids with high electrical conductivity and structural stability, while the carbon matrix could accommodate the volume change in cycling. Therefore，it is hypothesized that the combination of 1D electrospinning-derived CNF with 2D thin MoS_2 nanosheets could be an effective way to overcome the shortcomings of MoS_2-based anodes, thus resulting in higher specific capacity and cycling stability. Moreover, the production of flexible and self-standing membrane is another feature of the electrospinning technique. Since thin MoS_2 nanosheets are flexible, similar to that of multilayer graphene, they may act as fillers when dispersed in CNF and enhance the flexibility of the self-standing nanofibrous mats, enabling realization of flexible LIBs.

Based on equations 1.1 and 1.2, the theoretical specific capacity of MoS_2 is 670 mAh/g, however, specific capacities of higher than 900 mAh/g are commonly reported for the MoS_2-based systems. Though some explanations have been raised, such as alloying with Mo or surface absorption, the interfacial storage of Li^+ at the carbon and MoS_2 interfaces is believed to contribute most of the net charge storage. In this regards, the single-layer MoS_2 (SL-MoS_2) is an ideal candidate for lithium storage because of the largest surface area. Therefore, the engineering of SL-MoS_2/C nanocomposites with ideal interface is of great significance in terms of maximizing the specific capacity.

However, the large scale production of SL-MoS_2 is of big challenge due to its strong spontaneous tendency of restacking. Hydrothermal reaction is a popular approach to produce nanostructured MoS_2.[28] The hydrothermal growth of MoS_2 in the presence of glucose typically gives few-layer MoS_2 embedded in carbon because of the poor compatibility between the MoS_2 and glucose.[29] The addition of surfactant, such as CTAB can somewhat regulate the formation of MoS_2/C nanocomposites due to the improved interface interaction.[30] However, due to the weak van der Waals interaction, it typically gave a mixture of single-layer and few-layer MoS_2 in carbon. Building covalent linkage between the precursors may be an effectively solution. It is hypothesized the stable covalent bonds formed will greatly restrict the growth of MoS_2 crystals and benefits the formation of highly disordered single-layer MoS_2.

The van der Waals' heterostructure, which consists of layer by layer stacked 2D single-layer crystals, has been proved to reveal some unusual properties and phenomena.[31-33] For LIBs, this layer by layer architecture is also highly effective because of the strong coupling effect between atomic planes[34]. What's more, due to the large percentage of edges atoms, different storage mechanisms, insertion, conversion and interfacial storage of Li^+ could be reversibly combined, leading to remarkable improvement in electrochemical performances.[35] The alternating stacking of SL-MoS_2 with other isolated monolayers, graphene for example, will not only promotes the electron transport, but also immobilizes soluble polysulfide intermediates and tolerates the volume change during cycling. It is hypothesized that this intimate "face-to-face" contact between MoS_2

and graphene may trigger synergistic effects and maximize the Li^+ storage potential of both components.

1.2 Objectives and Scope

The main objective of this thesis is to overcome the inherent weaknesses of MoS_2-based anodes (sluggish kinetics and capacity fading) through design of novel morphology and structure and explore the potential of MoS_2-based nanocomposites as advanced anode materials. To achieve this target, the effects of layer numbers, interlayer distance, conductive additives (carbon) and crystal interfaces are investigated though the fabrication of ultrathin MoS_2 nanosheets as well as their hybrids, including: 1) aqueous exfoliated MoS_2 nanosheets; 2) MoS_2/C hybrid CNF; 3) sandwich-like SL-MoS_2/C nanocomposite and 4) alternately stacked SL-MoS_2 and *N*-doped graphene (NDG) heterostructure. The structural and morphological evolutions of the hybrids as well as the underlying formation mechanisms were investigated. On the basis of the above, their electrochemical properties, including rate capabilities and cycling stability, were evaluated via cyclic voltammetry (CV), galvanostatic charge/discharge (GCD), electrochemical impedance spectroscopy (EIS), etc. to correlate structures/morphologies with properties. The obtained knowledge will provide insightful information to facilitate future studies, especially in designing MoS_2 or other metal sulfides based electrodes.

1.3 Dissertation Overview

In *Chapter 1*, the rationale for selection of MoS_2 as well as the problems that MoS_2-based anodes are facing is introduced. The objectives and scope of this thesis are provided, followed by the main findings and outcomes.

In *Chapter 2*, the current research progress of MoS_2 in the literature is reviewed, covering from structure to synthesis, and also applications in LIBs. It starts with a short introduction of the three polytypes of MoS_2, emphasizing on the difference in their crystal structures and the resulting distinct properties. The preparation methods of MoS_2 nanosheets, including the top down and bottom up strategies, are then summarized. The use of MoS_2 as active components in the LIBs is discussed both in terms of cathode and anode, including their reaction mechanisms and state-of-art developments.

In *Chapter 3*, all the experimental details of this work are presented. It starts with the rationale for selection of synthetic methods, exfoliation, electrospinning and hydrothermal. Their advantages and the underlying mechanisms are demonstrated. Follows are the basic principles of some important characterization techniques. The detailed synthesis procedures, including the aqueous exfoliation of bulk MoS_2, the synthesis of MoS_2/C hybrid nanofibrous mats, SL-MoS_2/C nanocomposite and SL-MoS_2/NDG heterostructure, are then present.

In *chapter 4*, we disclose that alkali lignin, a low-cost, environmentally benign and bio-renewable feedstock, is an excellent surfactant for direct exfoliation of bulk MoS_2 to nanosheets via sonication in water. The stabilization mechanism and disperse conditions of lignin are explored. We demonstrate that the exfoliated MoS_2 nanosheets have great potential for application as low-cost LIB electrode materials because of the enhanced ion and electron transport kinetics. Our results also show that alkali lignin is a versatile surfactant for aqueous exfoliation of many other types of layered materials, including graphite, tungsten disulfide (WS_2) and boron nitride (BN).

In Chapter 5, highly flexible and free-standing MoS_2-based mat, consisting of disordered graphene-like MoS_2 nanosheets encapsulated in amorphous carbon nanofibers, were fabricated through hydrothermal route followed by electrospinning and annealing for the first time. The obtained binder-free self-standing nanofibrous mats can be directly used as an anode after simply punching the mats into suitable size and shape. The morphologies and mechanical properties of the mats vary with the MoS_2 contents, and its effect on the electrochemical performances is investigated. The high flexibility of the hybrid mat, which is ascribed to the multi-layered MoS_2 nanosheets as well as the resulting thin carbon sections, offers great opportunity for its practical use in various areas.

In Chapter 6, a unique SL-MoS_2/C sandwich structure is facilely prepared by simply mixing dopamine (DOPA) and Na_2MoO_4 aqueous solutions, followed by hydrothermal treatment and annealing. The complexation between DOPA and Mo^{VI} species is found crucial for the formation of the sandwich structure. Its structural and morphological evolution, as well as the growth mechanism is investigated. The large interlayer spacing, sandwich structure and crumpled nanosheet morphology of SL-MoS_2/C render it an

excellent anode material for LIBs. This solvent-free synthesis strategy is simple and scalable, and can be extended to prepare a series of metal oxide/sulphide and carbon composites, where defects-rich structures with ultrafine crystals are needed.

In Chapter 7, we present a facile self-assembly strategy for fabricating van der Waals heterostructures from isolated two-dimensional atomic crystals for the first time. Specifically, a novel NDG/MoS_2 heterostructure well-defined alternating structure was prepared through electrostatic attraction-induced self-assembly and subsequent carbonization. The fabrication, structural verification and morphology of the NDG/MoS_2 are studied. When used as an anode for the LIBs, it exhibits excellent cycling stability and high rate capability because the synergistic effect between the two components. This self-assembly approach can be easily transferred to other systems for surface modification of MoS_2 or fabrication of MoS_2-based nanocomposites (e.g. $Ni(OH)_2/MoS_2$, TiO_2/MoS_2), and their applications are not limited in batteries.

In *Chapter 8*, the threads of this thesis are drawn together. The main conclusions are summarized to show that the objectives stated in Chapter 1 are realized by engineering the morphology, structure and composition of the anodes, and the hypotheses are verified. The implications of the significant findings and outcomes obtained in this work are discussed. In addition, the recommendations for future works are proposed. Some reconnaissance works that did not warrant a complete chapter are also included.

1.4 Findings and Outcomes

Briefly, this research led to several novel outcomes by:

1) Alkali lignin, a low-cost, environmentally benign and bio-renewable feedstock is discovered for the first time an excellent surfactant for direct aqueous exfoliation of 2D materials via sonication. Various 2D materials, including graphene, MoS_2, BN and WS_2 have been successfully exfoliated with the assistance of lignin into ultrathin layers. The high concentrated suspensions are stable for months. This facile, scalable and eco-friendly aqueous-based process in combination with renewable and ultra-low-cost lignin opens up possibilities for large-scale fabrication of 2D materials based nanocomposites and devices.

2) Highly flexible and free-standing nanofibrous mats are produced by combining 1D electrospinning-derived CNF with 2D thin MoS_2 nanosheets. The hybrid mats the highly flexible and can maintain the structural integrity even after repeated bending, offering great opportunity for practical application in flexible and light weight devices.

3) A complexation-assisted approach for large-scale aqueous synthesis of SL-MoS_2/C sandwich structure is developed for the first time. It is found that the formation of complex (strong coordination bonding) between DOPA and MoO_4^{2-} can greatly restrict the growth of MoS_2 crystals, giving disordered single-layer MoS_2. This solvent-free synthesis strategy is proved to be a universal method to prepare metal oxide/sulfide ultrafine crystals embedded in carbon matrix. The Fe_3O_4/C and WO_2/C nanocomposites have been successfully synthesized with particles sizes of only ca. 7 nm and 4 nm, respectively.

4) The presence of atomic interfaces plays an important role in Li^+ storage. In this regard, the stacking of SL-MoS_2 with other 2D monolayers (graphene for example) is an ideal superstructure for high electrochemical performance. In this work, an electrostatic attraction-induced self-assembly strategy is adopted for the fabrication of MoS_2/NDG van der Waals heterostructures. The MoS_2/NDG nanocomposites exhibit excellent cycling stability and rate capability. This novel self-assembly approach is facile and scalable, and could also be applied to other systems for surface modification of MoS_2 or fabrication of MoS_2-based nanocomposites. As a demonstration, preliminary work on the fabrication of polyaniline/MoS_2 alternating structure and its application in supercapacitors is shown in chapter 8.

References:

[1] R. Mukherjee, A. V. Thomas, D. Datta, E. Singh, J. Li, O. Eksik, V. B. Shenoy and N. Koratkar. *Nat. Commun.* **2014**, 5.

[2] J. Liu, N. Li, M. D. Goodman, H. G. Zhang, E. S. Epstein, B. Huang, Z. Pan, J. Kim, J. H. Choi, X. Huang, J. Liu, K. J. Hsia, S. J. Dillon and P. V. Braun. *ACS nano*. **2015**, 9, 1985-1994.

[3] M. Agostini, J. Hassoun, J. Liu, M. Jeong, H. Nara, T. Momma, T. Osaka, Y.-K. Sun and B. Scrosati. *ACS Appl. Mater. Interfaces*. **2014**, 6, 10924-10928.

[4] T. Stephenson, Z. Li, B. Olsen and D. Mitlin. *Energy Environ. Sci.* **2014**, 7, 209-231.

[5] M.-R. Gao, Y.-F. Xu, J. Jiang and S.-H. Yu. *Chem. Soc. Rev.* **2013**, 42, 2986-3017.

[6] C.-H. Lai, M.-Y. Lu and L.-J. Chen. *J. Mater. Chem.* **2012**, 22, 19-30.

[7] X. Huang, Z. Zeng and H. Zhang. *Chem. Soc. Rev.* **2013**, 42, 1934-1946.

[8] D. Chen, W. Chen, L. Ma, G. Ji, K. Chang and J. Y. Lee. *Materials Today*. **2014**, 17, 184-193.

[9] E. Benavente, M. Santa Ana, F. Mendizábal and G. González. *Coord. Chem. Rev.* **2002**, 224, 87-109.

[10] J. Kong, C. Zhao, Y. Wei and X. Lu. *ACS Appl. Mater. Interfaces*. **2015**, 7, 24279-24287.

[11] U. K. Sen and S. Mitra. *ACS Appl. Mater. Interfaces*. **2013**, 5, 1240-1247.

[12] M. Wang, G. Li, H. Xu, Y. Qian and J. Yang. *ACS Appl. Mater. Interfaces*. **2013**, 5, 1003-1008.

[13] G. S. Bang, K. W. Nam, J. Y. Kim, J. Shin, J. W. Choi and S.-Y. Choi. *ACS Appl. Mater. Interfaces*. **2014**, 6, 7084-7089.

[14] X. Fang, X. Guo, Y. Mao, C. Hua, L. Shen, Y. Hu, Z. Wang, F. Wu and L. Chen. *Chem. - Asian J.* **2012**, 7, 1013-1017.

[15] U. K. Sen, P. Johari, S. Basu, C. Nayak and S. Mitra. *Nanoscale*. **2014**, 6, 10243-10254.

[16] J. Xiao, X. Wang, X.-Q. Yang, S. Xun, G. Liu, P. K. Koech, J. Liu and J. P. Lemmon. *Adv. Funct. Mater.* **2011**, 21, 2840-2846.

[17] X. Fang, X. Yu, S. Liao, Y. Shi, Y.-S. Hu, Z. Wang, G. D. Stucky and L. Chen. *Microporous Mesoporous Mater.* **2012**, 151, 418-423.

[18] L. Ji, M. Rao, H. Zheng, L. Zhang, Y. Li, W. Duan, J. Guo, E. J. Cairns and Y. Zhang. *J. Am. Chem. Soc.* **2011**, 133, 18522-18525.

[19] X. Ji, K. T. Lee and L. F. Nazar. *Nat. Mater.* **2009**, 8, 500-506.

[20] RadisavljevicB, RadenovicA, BrivioJ, GiacomettiV and KisA. *Nat. Nanotechnol.* **2011**, 6, 147-150.

[21] K. F. Mak, C. Lee, J. Hone, J. Shan and T. F. Heinz. *Phys. Rev. Lett.* **2010**, 105, 136805.

[22] J. Z. Wang, L. Lu, M. Lotya, J. N. Coleman, S. L. Chou, H. K. Liu, A. I. Minett and J. Chen. *Adv. Energy Mater.* **2013**, 3, 798-805.

[23] C. Zhao, J. Kong, X. Yao, X. Tang, Y. Dong, S. L. Phua and X. Lu. *ACS Appl. Mater. Interfaces*. **2014**, 6, 6392-6398.

[24] C. Zhang, Z. Wang, Z. Guo and X. W. Lou. *ACS Appl. Mater. Interfaces*. **2012**, 4, 3765-3768.

[25] Y.-E. Miao, Y. Huang, L. Zhang, W. Fan, F. Lai and T. Liu. *Nanoscale*. **2015**, 7, 11093-11101.

[26] L. Yang, S. Wang, J. Mao, J. Deng, Q. Gao, Y. Tang and O. G. Schmidt. *Adv. Mater.* **2013**, 25, 1180-1184.

[27] L. Hu, Y. Ren, H. Yang and Q. Xu. *ACS Appl. Mater. Interfaces*. **2014**, 6, 14644-14652.

[28] I. Song, C. Park and H. C. Choi. *RSC Adv.* **2015**, 5, 7495-7514.

[29] K. Chang and W. Chen. *J. Mater. Chem.* **2011**, 21, 17175-17184.

[30] Z. Wang, T. Chen, W. Chen, K. Chang, L. Ma, G. Huang, D. Chen and J. Y. Lee. *J. Mater. Chem. A*. **2013**, 1, 2202-2210.

[31] A. K. Geim and I. V. Grigorieva. *Nature*. **2013**, 499, 419-425.

[32] S. Haigh, A. Gholinia, R. Jalil, S. Romani, L. Britnell, D. Elias, K. Novoselov, L. Ponomarenko, A. Geim and R. Gorbachev. *Nat. Mater.* **2012**, 11, 764-767.

[33] L. Ponomarenko, A. Geim, A. Zhukov, R. Jalil, S. Morozov, K. Novoselov, I. Grigorieva, E. Hill, V. Cheianov and V. Fal'Ko. *Nat. Phys.* **2011**, 7, 958-961.

[34] Y. Dou, J. Xu, B. Ruan, Q. Liu, Y. Pan, Z. Sun and S. X. Dou. *Adv. Energy Mater.* **2016**, 6, 1501835.

[35] C. Zhu, X. Mu, P. A. van Aken, Y. Yu and J. Maier. *Angew. Chem., Int. Ed.* **2014**, 53, 2152-2156.

.

Chapter 2

Literature Review

In this chapter, the current research progress on MoS_2 reported in literatures is reviewed, with the focuses on its structure, synthesis and applications in LIBs. It starts with a short introduction of the three polytypes of MoS_2, emphasizing on the difference in their crystal structures and the resulting distinct properties. The preparation methods of MoS_2 nanosheets, including the top down and bottom up strategies, are then summarized. The use of MoS_2 as active components in the LIBs is discussed both in terms of cathode and anode, including their reaction mechanisms and state-of-art developments. Based on the literature, however, the large-scale aqueous synthesis of MoS_2, especially SL-MoS_2 is still challenging, and the application of MoS_2 as flexible devices is also seldom reported.

2.1 Structure and Properties of MoS_2

As briefly discussed in Chapter 1, bulk MoS_2 is a 2D layered material, similar to that of graphite. The concept of MoS_2 "monolayer", however, is different from graphene, as each layer of MoS_2 is actually composed of three atomic layers (S–Mo–S) that are covalently bonded. The MoS_2 monolayer or SL-MoS_2 usually refers to this S–Mo–S "triple layer" by convention.

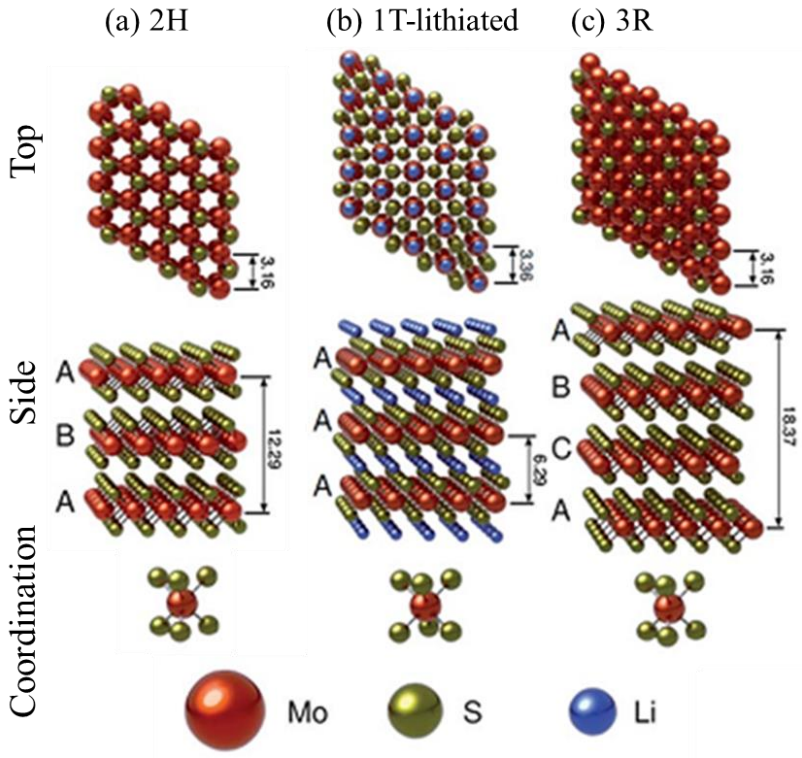

Figure 2.1 Top and side views of the (a) 2H, (b) 1T and (c) 3R of MoS_2 as well as the coordination of Mo atoms. Notes that the 1-T MoS_2 is metastable and is usually prepared by Li^+ intercalation. Dimensions are in Angstroms.

So far, three polytypes of MoS_2 have been identified: 2H, 3R and 1T, which are classified according to the stacking order of MoS_2 monolayers and the coordination of central Mo cations. The top and side views of the three polytypes are shown in Figure 2.1. In 2H and 3R polytypes, the Mo atoms are both in trigonal prismatic coordination, but the stacking sequences of the MoS_2 monolayers are different. The 2H polytype has a stacking order of ABAB, and each unit cell contains two S-Mo-S layers, thus falling into the hexagonal

crystal system, with lattice parameters of a = 3.15 Å, c = 12.30 Å.[1] The 3R polytype, however, belongs to rhombohedral crystal system. Each unit cell contains three S-Mo-S layers with a stacking order of ABC. The lattice parameters of 3R MoS_2 are a = 3.17 Å, c = 18.38 Å.[2] Both the 2H and 3R MoS_2 can be found in nature as minerals, but the 2H polytype is much more abundant. Therefore, if not specialized, the expression "MoS_2" will refers to its 2H polytype in the literature.

The 1T polytype, on the contrary, is synthetic and metastable. Alkali intercalation followed by hydrolysis and oxidation is the most widely used method for the preparation 1T MoS_2. When Li^+ intercalate into the van der waals gap of 2H MoS_2, they occupy the vacant octahedral/tetrahedral interstices.[3,4] The coordination of Mo cations therefore, changes from trigonal prismatic to octahedral, accompanied by a phase change from 2H to 1T, as shown in Figure 2.1(b). Meanwhile, the electrons transfer from Li to MoS_2 and stabilize the 1T structure. The 1T polytype belongs to trigonal crystal system, and each unit cell contains only one S-Mo-S layers with a stacking order of AAA. The crystal structures of the three polytypes of MoS_2 are summarized in Table 2.1. The lithiated 1T MoS_2 will be hydrolyzed and oxidized when in contact with water, during which 1T MoS_2 is exfoliated to single layers.[5-7] The existence of excess electrons prevent the instant transition back to 2H phase, but slight distortion of the Mo coordination were observed.[8]

Table 2.1 Structure and properties of the three polytypes of MoS_2.

Polytype	Crystal system	Stacking order	Lattice parameters	Properties
1T	trigonal	AAA	a = 3.36 Å, c = 6.29 Å	metastable, metallic[9]
2H	hexagonal	ABAB	a = 3.16 Å, c = 12.29 Å	stable, semiconductor
3R	rhombohedral	ABCABC	a = 3.16 Å, c = 18.37 Å	stable, semiconductor

The properties of MoS_2 are closely related to its structure and bonding. The 2H MoS_2 is a semiconductor with an indirect bandgap of 1.29 eV,[10] therefore a very promising material in semiconductor industry as an alternative of silicon.[11] The weak van der Waals force between layers renders the 2H MoS_2 an excellent dry lubricant, especially under high vacuum and load.[12,13] Due to the strong S-Mo-S bonds and inactivity of S basal planes, the 2H MoS_2 is chemically and thermally inert. Under vacuum or argon (Ar)

atmosphere, it is stable up to 1200 ^{o}C, [14] and it doesn't dissolve in most of the solvents except aqua regia and hot concentrated sulfuric acid. The 3R polytype has similar properties to that of 2H, while the 1T MoS_2 is metallic due to the octahedral coordination of Mo cations. The 1T phase is not stable, and can be easily transforms back to 2H after long tine aging or simple annealing.[5,15]

2.2 Preparation of 2D MoS_2 Nanosheets

In order to utilize the valuable properties of monolayer or few-layer MoS_2, different exfoliation techniques (top down) or synthesis methods (bottom up) have been developed, including micromechanical exfoliation,[16] chemical exfoliation through intercalation,[17,18] liquid-phase exfoliation,[19] thermal ablation method,[20] chemical vapor deposition (CVD) on substrates[21] and direct solvothermal synthesis[22], etc.

2.2.1 Top down methods

2.2.1.1 Mechanical exfoliation

The successful mechanical cleavage of graphene from graphite has inspired the research to obtain MoS_2 monolayers using the same way.[23] In 2005, 2D MoS_2 monolayers were first isolated by a simple rubbing procedure.[24] The obtained MoS_2 monolayers are of high crystal quality and stable in ambient conditions. Using the way, the authors successfully isolated various 2D atomic crystals, including graphite, BN, $NbSe_2$, etc. The scotch-tape micromechanical cleavage technique was also applied for the production of SL-MoS_2. A SL-MoS_2 filed effect transistor was fabricated in 2012, which showed a carrier mobility of more than 200 cm^2/Vs and a current on/off ratio of 10^8 at room temperature.[25] In the same year, a modified scotch-tape cleavage method, which is called anodic bonding, was proposed. A bonding force was first introduced between the MoS_2 precursor and the glass substrate by high voltage (200-1500 V) and temperature (130-200 ^{o}C). Single layer or few layered MoS_2 flakes were then obtained by peeling off the unbonded materials.

2.2.1.2 Chemical exfoliation

Though high qualitied 2D SL-MoS_2 crystals can be obtained by mechanical exfoliation,

this method is of extremely low efficiency and is only applicable to fundamental research in the lab. In contrast, chemical exfoliation is an effective way for high yield production SL-MoS_2 and SL-MoS_2 based nanocomposites.

As early as 1986, SL-MoS_2 was first prepared by Joensen et al. via Li^+ intercalation followed by reaction with water.[25] The intercalation of Li^+ is found to be a Li^+/e^- transfer topotactic reaction. Accompanied by the Li^+ intercalation, electrons are transferred to the 4d orbit of Mo,[7] leading to negative charged MoS_2 layers.[6] Once in contact with water, the Li^+ ions were hydrated, causing an expansion of the interlayer space, while water was reduced to H_2 and OH^- by the negatively charged MoS_2.[26] The microbubbles formed further pushed the expanded MoS_2 layers apart, yielding a stable colloidal dispersion of MoS_2 monolayers The as-prepared SL-MoS_2 dispersion was stable at neutral pH for weeks while flocculates immediately when the pH is lower than 2. However, due to the chemical inertness of MoS_2, only very strong reducing agents can reduce the Mo and allows the intercalation of Li^+. Among them, N-Butyllithium (n-BuLi) or lithium borohydride ($LiBH_4$) are commonly used.

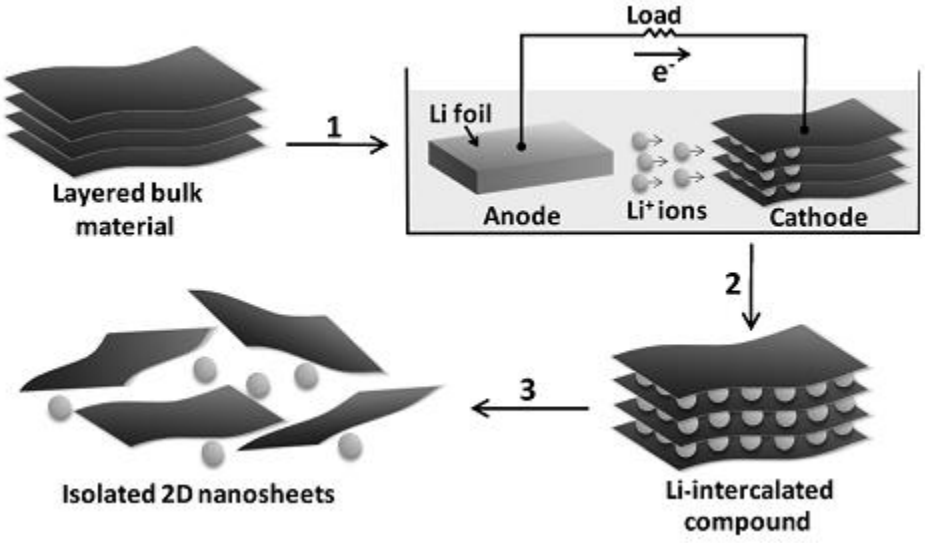

Figure 2.2 The fabrication of SL-MoS_2 via electrochemical lithiation and exfoliation.

The intercalation of Li^+ could also be accomplished through an electrochemical way.[27] In 2011, Zeng et al. reported an effective preparation method for the SL-MoS_2 through controllable lithiation and exfoliation.[28] The fabrication process was shown in Figure

2.2. A typical coin cell was first assembled, with bulk MoS_2 as the cathode and a lithium foil as the anode. The cell was galvanostatically discharged until complete intercalation of Li^+ was achieved, which could be monitored by the slope change of the discharge curve. The cell was then de-assembled and the Li-intercalation compound (Li_xMoS_2) was ultrasonically treated in water. The isolated 2D MoS_2 monolayers were finally collected by centrifugation. Compared to direct chemical intercalation, the electrochemical intercalation of Li^+ greatly shortens the reaction time, from days to hours. Nevertheless, only submicron sized SL-MoS_2 could be obtained in both cases.

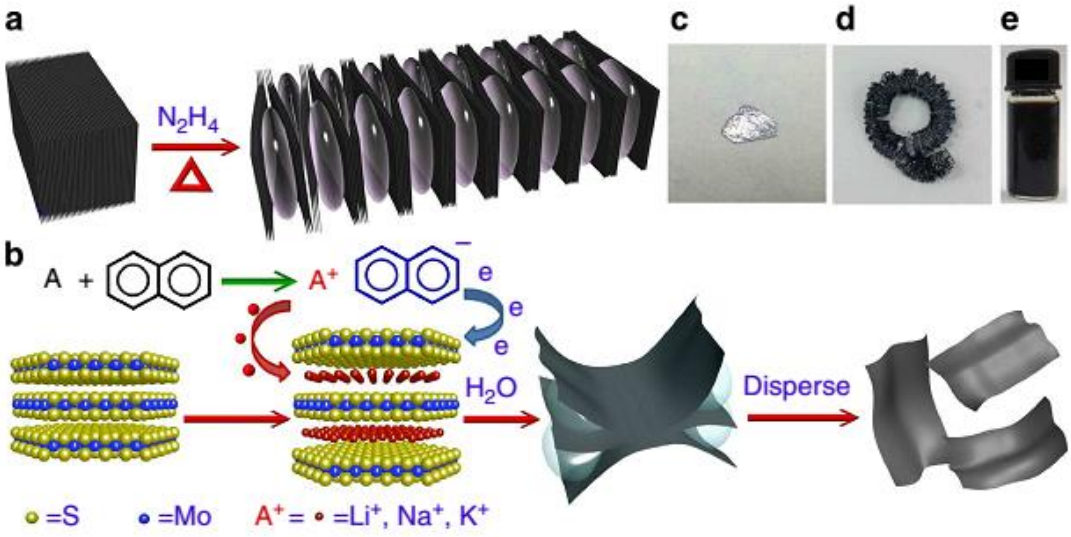

Figure 2.3 Schematic of the fabrication process of SL-MoS_2. (a) Pre-exfoliated of bulk MoS_2 by N_2H_4. (b) Alkali ion intercalation of sample (a) followed exfoliation in water. Photograph of (c) bulk MoS_2, (d) pre-exfoliated MoS_2 and (e) exfoliated SL-MoS_2 dispersion.

Later in 2014, a two-step intercalation and exfoliation method was reported by Zheng et al.[29] The fabrication process is illustrated in Figure 2.3. Bulk MoS_2 was first pre-intercalated by N_2H_4 under hydrothermal conditions. The intercalated $N_2H_5^+$ cations expanded the interlaying spacing of MoS_2, which facilitated the following intercalation of alkali ions. SL-MoS_2 sheets with lateral size around 10 μm were produced after exfoliation in water. This could be attributed to the reduced reaction intensity between the naphthalene radical anion and MoS_2, as well as the low powder sonication.

2.2.1.3 Liquid exfoliation

Chemical exfoliation is an ideal way to produce SL-MoS_2 with high yield, its application, however, is still limited by the low productivity (usually in mg) and complicated procedures (intercalation, exfoliation, etc.). Recently, a simple liquid exfoliation method was developed by Coleman et al, which makes the mass production of 2D MoS_2 nanosheets possible.[30-32] Single or few-layered nanosheets could be produced by sonication of layered materials in various solvents. However, the stability and concentration of the dispersion varies. For MoS_2, solvents like N-methyl-pyrrolidone (NMP) is promising due to their close matched surface energy, which minimizes the mixing enthalpy and therefore leads to high concentrated dispersion (~0.3 mg/ml).[30,33] This solution processing route is of extreme simplicity. The obtained nanosheets could be processed into films or devices directly after the removal of NMP.

However, the removal of NMP is difficult due to its high boiling point. The cost and post-treatment of NMP may be other issues that have to be considered. To solve these problems, a mixed solvent strategy based volatile solvents was proposed by Zhou et al.[34] The solubility of MoS_2 in various solvents or solvent mixtures was predicted by the Hansen solubility parameters. It was found that two poor solvents could be combined into a good one under appropriate proportion. Specifically, a mixture of 45 vol% ethanol- 55 vol% water gave the best solubility of MoS_2, with the highest concentration of ~0.018 mg/ml. Though this value is still too low compared with that in NMP, it was much higher than those in pure water or ethanol. Later, Yao et al. reported a two-step exfoliation method to prepare high concentration dispersion of MoS_2.[35] Bulk MoS_2 was first ground with the assistant of NMP and pre-exfoliated into thin layers. The subsequent sonication in ethanol/water further exfoliated the MoS_2 thin layers and broke large crystals. As a result, high concentration up to ~27 mg/ml was achieved under optimized conditions. The dispersion was stable over days due to the electrostatic repulsion between MoS_2 nanosheets.

The exfoliated MoS_2 nanosheets can not only be stabilized by the interaction with solvent but also a coating of surfactant.[36-38] Compare to the former, the surfactant-assisted exfoliation extends the choice of solvent and endows the dispersion with better stability. Among various kinds of surfactants, the ionic type is preferred because of their strong

affinity with the exfoliated nanosheets and subsequent electrostatic stabilization.[39] For example, when bulk MoS_2 was sonicated in water with sodium cholate as the surfactant, the dispersion concentration increased to ~0.5 mg/ml, and it was stable over a wide range of pH.[40] The concertation of the MoS_2 dispersion increases with surfactant concentration, sonication time as well as the initial concentration of MoS_2.

2.2.2 Bottom up methods

From the perspective of chemistry, the synthesis of MoS_2 nanosheets can be categorized into two groups: thermal decomposition of thiosalts and sulfurization of various molybdenum compounds.

2.2.2.1 Thiosalt decomposition

Ammonium thiomolybdate ($(NH_4)_2MoS_4$, ATM) is the most widely used thiosalt for the preparation of MoS_2 nanosheets.[41,42] The thermolysis of ATM occurs at relatively low temperature in inert atmosphere (equation 2.1).

$$(NH_4)_2MoS_4 \rightarrow 2NH_3 + H_2S + MoS_3 \qquad (2.1)$$

When the temperature further increases, the MoS_3 is decomposed into MoS_2 at around 800 ^oC (equation 2.2).[43]

$$MoS_3 \rightarrow MoS_2 + S \qquad (2.2)$$

The formation of MoS_2 happens at much lower temperature ~425 ^oC in the presence of hydrogen (H_2).[43]

$$(NH_4)_2MoS_4 + H_2 \rightarrow 2NH_3 + 2H_2S + MoS_2 \qquad (2.3)$$

However, a slight decompose is observed when the MoS_2 was annealed in H_2 at around 500 ^oC, and direct thermolysis of ATM usually can't get high qualitied MoS_2 thin layers as it is very sensitive to the trace oxygen at high temperature.[44] Therefore, a two-step annealing process was proposed by Liu et al, for the preparation of highly crystalline MoS_2 thin layers, as illustrated in Figure 2.4. ATM was first dissolved in dimethylformamide (DMF) and dip-coated on sapphire or silicon wafer. The sample was annealed at 500 ^oC for 1 hour in a mixture of Ar and H_2, and then at 1000 ^oC for 30 minutes in Ar and S. The addition of S was found crucial in enhancing the crystallinity of MoS_2, which acted as a protection gas against oxidation. [44]

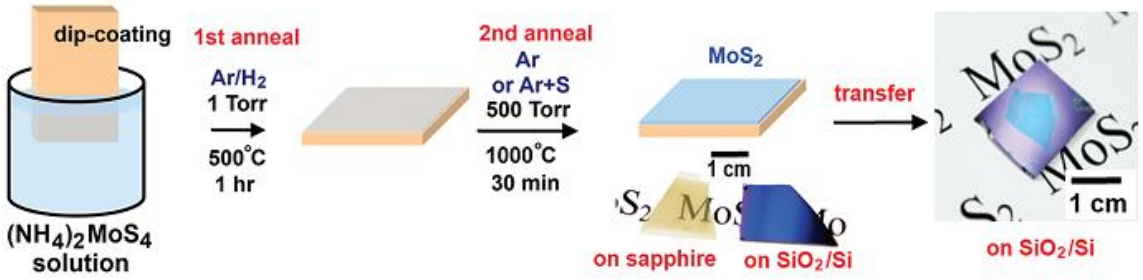

Figure 2.4 Fabrication of highly crystalline MoS_2 thin layers via a two-step process.

Later, a MoS_2/graphene heterostrucute was reported by Shi et al. via CVD.[45] An ATM/DMF vapor was carried by Ar into the growth chamber and subsequently deposited on the surface of graphene. MoS_2 flakes were in-situ synthesized at a much lower temperature of 400 ^oC, even though the lattice mismatch may hinder the growth of single crystals. The thickness of the MoS_2 layers could be controlled by the deposition time and concentration of the ATM solution. More importantly, the directly deposition of MoS_2 on a conductive substrate make it suitable for a variety of functional electronics because of the cooperative action.

In addition to the solid state approaches, a novel wet chemistry route was proposed by Altavilla et al. for the production of 2D MoS_2 nanosheets.[46] ATM was dissolved in oleylamine under N_2 and thermally decomposed in at 360 ^oC. The obtained singe or few layer MoS_2 nanosheets were stabilized by the oleylamine coating, so that both aggregation and oxidation could be avoided.

2.2.2.2 Sulfurization of molybdenum compounds

Sulfurization of molybdenum compounds is the most widely used method for the preparation of 2D MoS_2 nanosheets because of the abundance of molybdenum (Mo) and S sources as well as their flexible combination. So far, various Mo and S sources have been reported, including Mo,[47] $MoCl_5$,[48] MoO_3,[49,50] $Mo(CO)_6$,[51] $H_3PMo_{12}O_{40}$,[52] $(NH_4)_6Mo_7O_{24}$,[53] Na_2MoO_4,[54] S,[55,56] H_2S,[57] Na_2S,[58] CH_3CSNH_2,[59] NH_2CSNH_2,[60] and L-cysteine.[61]

In 2012, large-Area MoS_2 thin layers were synthesized on SiO_2/Si by Lee et al. via CVD for the first time, based on the volatile nature of MoO_3 and S.[49] Similarly, a two-step

thermal treatment of MoO_3 in the presence of S was reported by Lin et al.[50] The deposited MoS_2 could be further thinned by mechanical exfoliation.[62] Zhan et al. reported a direct vapor phase growth of MoS_2, which involved pre-depositing of Mo followed by reaction with S vapor.[47] Interestingly, a new vapor-solid growth method using bulk MoS_2 itself as the precursor was reported by Wu et al.[63] High optical MoS_2 monolayers up to up to 25 μm were synthesized.

The fabrication of MoS_2 heterostructures could also be realized by sulfurization.[48,55,56] Lin et al. prepared SL-MoS_2 on graphene via sulfurization of MoO_3 (Figure 2.5(a)).[56] It was found that the nucleation and growth of MoS_2 was strongly influenced by the residual strain and wrinkle of the graphene substrates. McCreary et al. prepared uniform MoS_2 thin films on graphene with centimeter scale using $MoCl_5$ as precursor instead of MoO_3.[48] A MoS_2-$MoSe_2$ lateral heterostructure was fabricated by Duan et al. by controlling the growth fronts. A domain of MoS_2 was first grown by sulfurization of MoO_3, during which the S was in-situ replaced by Se. The subsequent lateral growth of $MoSe_2$ occurred at the peripheral edges of MoS_2 where the unsaturated dangling bonds were predominant, thus facilitating the relaxation of strain force (Figure 2.5(b)).[55]

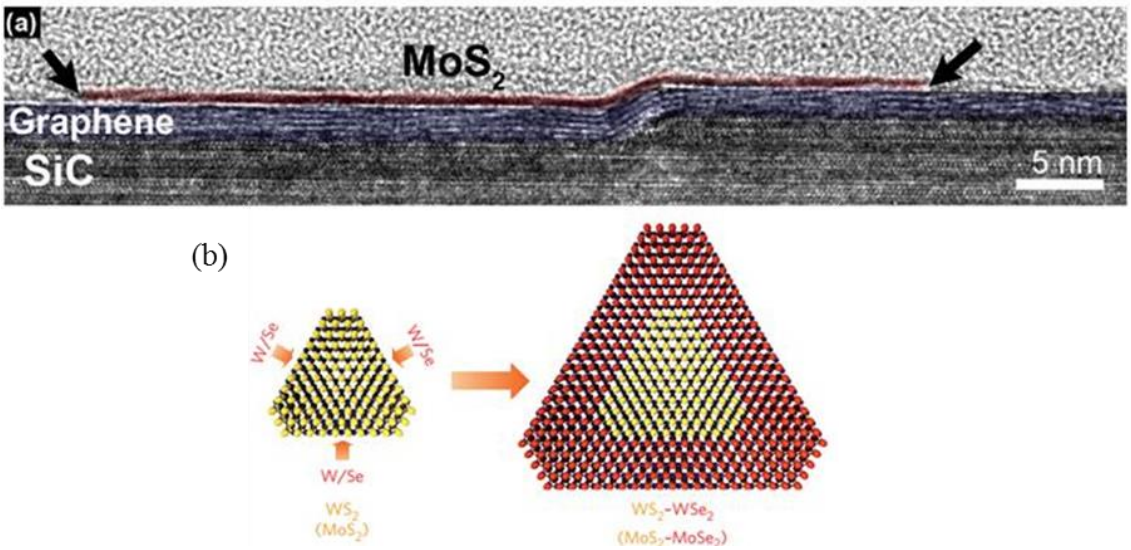

Figure 2.5 Illustration of the (a) MoS_2/graphene heterostructure and (b) MoS_2-$MoSe_2$ lateral heterostructure.

The hydrothermal method is another useful technique that widely used in the preparation

of MoS_2. Various nanostructures, including monolayers,[64] nanosheets,[65] nanorods,[66] fiber bundles,[58] nanoparticles,[67,68] and nanoflowers[69,70] have been reported so far.

MoS_2 monolayers were synthesized by Peng et al in 2001.[64] Ammonium molybdate ($(NH_4)_6Mo_7O_{24}$) and sulfur were used as raw materials and hydrazine was added as the reductant. The obtained MoS_2 exhibited large surface area of 240 m^2/g, and no stacking was detected in XRD. MoS_2 nanoparticles were synthesized on fluorine-doped tin oxide (FTO) directly with NH_2CSNH_2 as the S source.[67] The structure of MoS_2 varied with the hydrothermal temperature and molar ratio of precursors. Flower-like MoS_2 was synthesized if the FTO template was removed, as corrugation and scrolling reduces the surface energy of MoS_2.[70] The addition of additives/surfactant also significantly affects the morphology and structure of MoS_2. MoS_2 nanofibers and nanorods were fabricated by adding citric acid and sillicontungstic acid as the morphology regulators respectively.[58,66] The defects play an important role in enhancing electrochemical properties of materials as the edge sits can act as active redox centers. Engineering defects into MoS_2 could be accomplished with high concentration of thiourea, as shown in Figure 2.6. The functions of thiourea were multiple: 1) a reductant that reduced the Mo^{6+} to Mo^{4+}; 2) a S source that decomposed into H_2S under hydrothermal conditions and 3) a surfactant that hindered the growth of MoS_2 nanocrystallites and stabilized the defect rich structure.

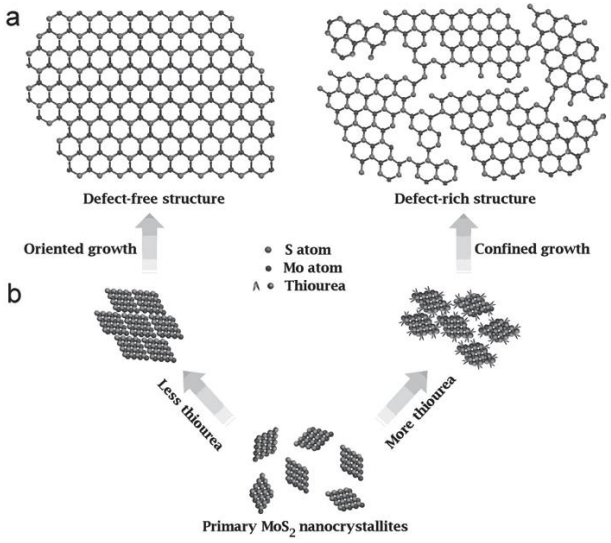

Figure 2.6 Structural illustrations of (a) defect-free and (b) defect-rich structures of MoS_2 prepared by varying the concentrations of thiourea.

2.3 Application of MoS_2 as LIB Electrodes

The research of MoS_2 crosses a broad range of discipline. Its unique properties render it exquisite versatility, and enable its use in various scientific fields, such as energy storage, sensing, catalyst, etc., many of which have been summarized in recent reviews.[71-73] In this chapter, we will focus on MoS_2 or MoS_2 based hybrids as active component in the LIBs, both in terms of cathode and anode.

2.3.1 Operating principle of LIBs

Energy storage devices have attracted great attention in recent years because of the growing demand for portable energy storage devices such as laptops, cell phones and electric vehicles. Among the myriad energy-storage technologies (for example, nickel-cadmium, nickel-metal hydride, etc.), LIBs play an increasingly important role because of their high specific energy (energy per unit weight) and energy density (energy per unit volume) (Figure 2.7).

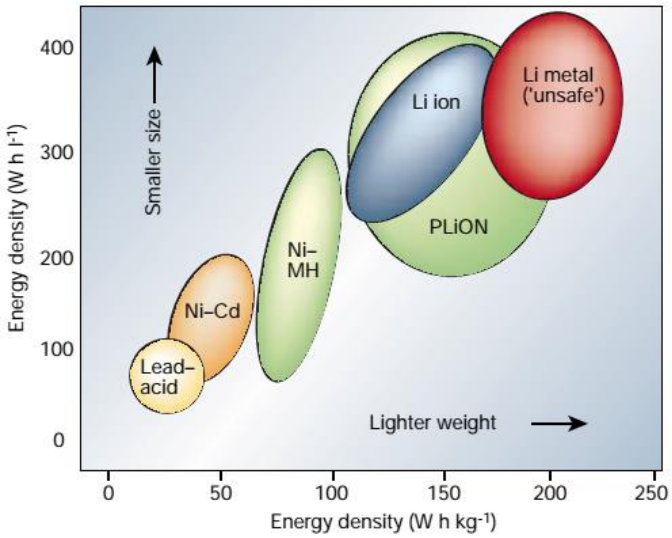

Figure 2.7 Comparison of various energy storage technologies in terms of volumetric and gravimetric energy density (PLiON: polymer lithium ion battery).

In commercial, a battery is a combination of several cells that are in parallel or series connection to output the required voltage or capacity. Each cell, the power-generating compartment of LIB, consists of two electrodes (cathode and anode) that are separated by

electrolyte. The capacity of the cell depends on the adsorption ability of electrode materials to Li^+ ions, while the cell potential is determined by the voltage difference between the two electrodes. As a secondary battery, cyclability is an important parameter to judge the performance of a cell, which relies on structural stability of the electrodes, that is, the repeatability of Li^+ insertion/extraction.

Briefly speaking, the electrochemical process of LIB is essentially a repeatable insertion/extraction of small ions into/from electrodes, accompanied by a flow of electrons in the external circuit. The operating principle of LIBs is illustrated in Figure 2.8. When a cell is charged, the Li^+ move from the cathode to the anode through the electrolyte and remain there. The cell takes in energy (electrons) through the external circuit and the cell potential increases until a cutoff value. This process is reversed during discharge, and the current produced is collected by the use. In order to improve the electrochemical properties of the electrodes, efforts should be put on following critical parameters: proper materials, good structure and architecture stability, improved electrical conductivity, etc.

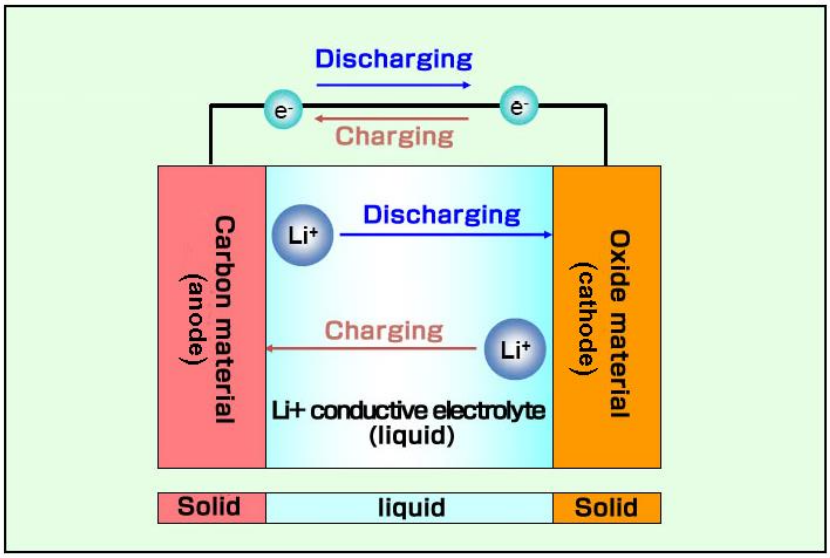

Figure 2.8 Operating principle of lithium-ion batteries

2.3.2 Cathode (1-3 V)

MoS_2 was first considered as a cathode material in the secondary lithium metal batteries

because of its intermediate voltage profile.[74-77] Between 1-3 V *versus* Li/Li^+ (V), the lithiation/delithiation of MoS_2 is highly reversible, and the redox reaction is shown in equation 2.4 with x ($0 \leq x \leq 1$) indicates the degree of lithiation.

$$MoS_2 + xLi^+ + xe^- \leftrightarrow Li_xMoS_2 \quad (2.4)$$

During discharge, Li^+ gradually insert into the van der Waals gap of MoS_2, causing a phase change from 2H to1T, which is associated with the voltage plateau at ca. 1.1 V. Theoretically, one mole of MoS_2 will uptake one mole of Li^+ upon fully lithiation ($x = 1$), delivering a specific capacity of 167 mAh/g. The lattice parameters expand only 5% after the formation of $LiMoS_2$. which is much smaller than other emerging electrode materials.[3] The metallic 1T MoS_2 formed could also enhance the conductivity of the electrode. As a result, the MoS_2 cathode shows good cycling stability and rate performance between 1-3 V.[78]

In the 1980's, the MoS_2 cathode was first commercialized by Moli Energy with lithium metal as the anode. The MoS_2 could be used directly without pre-lithiation. The structural evolution in the intercalation process was studied by Chrissafis et al.[79] It was found that, the amorphous or disorder MoS_2 delivered much higher specific capacity than the crystalline form. The much faster Li^+ diffusion coefficient was believed to be responsible for this improvement.[75,76] To further enhance the electrochemical performance, some other attempts have also been tried, which includes partial replacement of S with O,[80] incorporation with conducting agents,[81] and oxidation of Mo to higher valence.[82] However, the growth of lithium dendrites is the major safety concerns of these batteries, which may cause short circuit and even fire hazard during cycling. The intermediate cathodic voltage (ca. 2V) of is another major disadvantage of the MoS_2 cathode, which lowers the energy density of the cell, though in some cases, this may be compensated by its relatively higher specific capacity.

2.3.3 Anode (0-3 V)

The MoS_2 has not been considered as an anode material until recently, more and more researchers verified the recyclability of MoS_2 between 0-3 V.[83-87] A significant change in lithiation mechanism will occur when the MoS_2 is discharged below 1 V. With the

continue insertion of Li^+ (x>1), the structural transformation of MoS_2 becomes irreversible. When the concentration of Li^+ exceeds the saturation limit, a decomposition reaction happens at about 0.5 V, yielding Mo and Li_2S, as shown in equation 2.5.

$$Li_xMoS_2 + (4-x)Li^+ + (4-x)e^- = 2Li_2S + Mo \quad (2.5)$$

However, there is a debate in the oxidation process. Typically, two cathodic peaks are observed in the CV curve during charge, as shown in Figure 2.9. The first smaller one locates at about 1.6 -1.7 V, which can be attributed to the partial oxidation of Mo to MoS_2,[88] delithiation of residual Li_xMoS_2[57] or deassociation of Li^+ with Mo.[89] The oxidation potential seems to support the first two conclusions, but no MoS_2 can be detected from XRD due to their amorphous nature. In the bulk form, Li^+ do not alloy with Mo. However, for Mo nanoparticles, their activity may be greatly enhanced due to the large surface area and high surface energy. The second oxidation peak locates at about 2.2-2.3 V with much stronger intensity. Previous reports claimed that this peak could be attributed to the formation of MoS_2.[53,90] However, if that's the case, the polarization between charge and discharge will be as large as 1.8 V. That is not likely to happen for transition metal sulfides, which is usually less than 1 V.[91,92] In addition, for the following cycles, the reduction peak at about 1.1 V and 0.5 V almost disappears. Instead, a new peak emerges at about 1.8 V, indicating the decomposition of MoS_2 is actually irreversible.

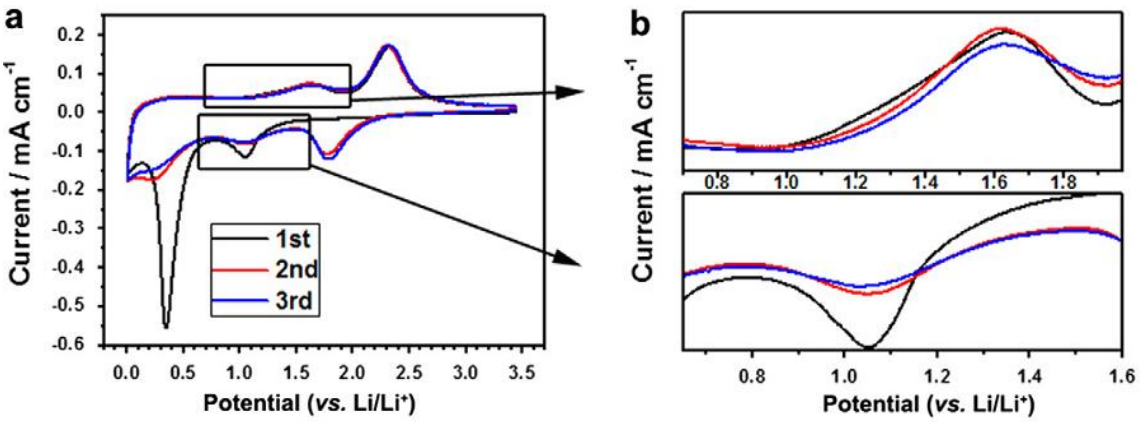

Figure 2.9 CV curves of mesoporous MoS_2 at a scan rate of 0.05 mV/s between 0.01–3.3 V.

The reaction mechanism of MoS_2 anode was carefully examined by Xiao et al via XRD

and HRTEM at different depth of charge and discharge.[89] They found that, the MoS_2 electrode actually becomes a mixture of S and Mo after the first cycle, and the S/Li_2S couple dominants the following redox process. Thus, it's clear that the oxidation peak at 2.2 V is attributed to the conversion of Li_2S to S, while the reduction peak at 1.8 V is indicative of the reverse reaction, similar to that of Li-S batteries[93,94] This conclusion was confirmed by other researchers soon after, either by experimental data or theoretical calculations.[57,95-97] Note that the existence of Mo may alter the chemistry of S or Li_2S, because the redox potentials of MoS_2 anode are slightly different from that of Li-S batteries. Anyway, because of the same reaction mechanism, the progress in Li-S batteries will shed light on the development of MoS_2-based anode, or vice versa.

Similar to the Li-S batteries, MoS_2 suffers from sluggish kinetics due to its limited electron and Li^+ conductivity, especially along the c-direction, and the shuttle effect caused by the soluble polysulfide intermediates results in a loss of active material and continuous capacity decay. In addition, though the volumetric expansion of MoS_2 is "only" 103% (calculated based on the density of MoS_2, Mo and Li_2S), which is much smaller than other emerging anode materials, the repeated expansion and contraction may still cause a collapse of the structure.

Reducing the number of layers is an effective way to enhance the electron and Li^+ transport of MoS_2, because it not only increases the contact surface area with the electrolyte, but shortens the diffusion distance along the c-direction. Ding et al prepared MoS_2 microspheres composed of few-layered nanosheets using polystyrene microsphere as the template.[98] The resultant materials showed promising electrochemical performance with improved rate and cycling capabilities. Sen et al prepared flower-like MoS_2 containing 2D nanowalls via a two-step process. They found that, compared to traditional PVDF binder, the use of cellulose could enhance the cycling stability of the electrode due to its better tolerance with the large volumetric change.[99] An important progress was made by Hwang et al, who synthesized highly disordered graphene-like MoS_2 nanoplates via a solvothermal reaction of S and $Mo(CO)_6$ in xylene.[51] The MoS_2 nanoplates is only 30 nm in length and few nanometers in thickness, with amorphous and crystalline regions evenly distributed through the whole region. As a result, extraordinary

high rate capacity up to 554 mAh/g was achieved even at 53.1 A/g after 20 cycles. Apart from the success in half cell, they also assembled a full cell using lithium cobalt oxide as the cathode, and demonstrated excellent rate capability at 1A.

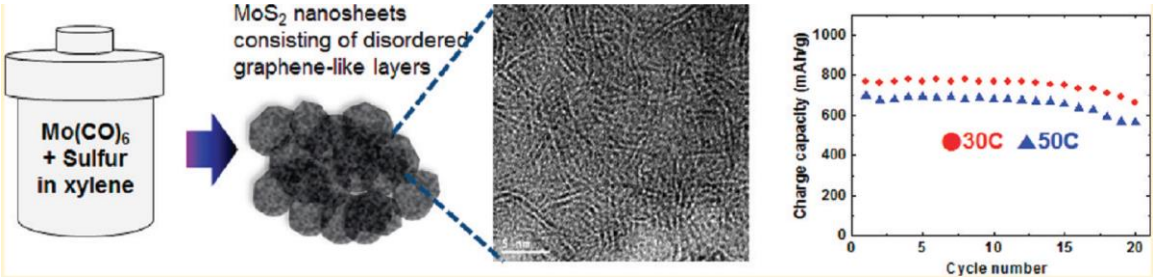

Figure 2.10 Schematic illustrations of the preparation, structure and property of the MoS_2 nanoplates.

Expanding the interlayer spacing of MoS_2 is another way to meliorate the electron and Li+ transport. What's more, the expanded wan der Walls gap could accommodate more Li^+ before the conversion reaction, and the larger gap will buffer the volumetric change during cycling, thus improving the specific capacity and cycling stability of the electrode. The chemical exfoliated MoS_2 monolayers are unstable and will restack spontaneously upon heating or long time storage. Through this exfoliation and restacking process, Du et al prepared restacked MoS_2 nanosheets with an interlayer distance of 0.635 nm, 0.15 nm larger than that of bulk MoS_2.[100] The restacked sample exhibited superior stability and high capacity compared to its bulk counterpart. Highly ordered mesoporous MoS_2 was prepared by Liu et al using SBA-15 as the self-sacrificing template.[101] The MoS_2 precursor was first filled into the pores of SBA-15 via vacuum assisted impregnation, followed by sulfurization and removal of template. The XRD and TEM results showed that the resultant MoS_2 is mesoporous with an expanded interlayer spacing of 0.66 nm, which provided sufficient space for fast Li^+ diffusion. This is confirmed by the lower charge transfer resistance and activation energy, showing a reversible capacity of 600 mAh/g at 10A/g.

Another popular approach to improve the performance of the MoS_2-based electrodes is to integrate MoS_2 with carbonaceous materials to fabricate nanocomposites with specially designed architectures. The role of carbon is multiple: 1) it provides good e^- and Li^+

transport; 2) it confines the discharge products from shuttling; 3) it serves as a buffer to nullify the shrinkage during cycling and 4) last but not least, it prevents the aggregation or restacking of MoS_2. Graphene [54,102-106] and carbon nanotubes (CNT) [90,107-111] are the most widely used carbonaceous materials due to their large surface area, high conductivity, and structural stability.

Three-dimensional (3D) graphene/MoS_2 was prepared by Yu et al via a simple hydrothermal method.[112] MoS_2 nanoflake arrays were grown vertically on the surface of graphene, forming a hierarchical architecture. 3D graphene foam was also regarded as an excellent backbone for the load of MoS_2, which acted as a highly conductive matrix for e^- and Li^+.[113] Honeycomb like MoS_2 was anchored into the graphene foam with the help of P123 surfactant. This unique architecture showed improved Li^+ storage capacity because of high surface area, high conductivity and close contact between the graphene matrix and MoS_2 nanosheets.

The functions of CNT are similar to that of graphene except that CNT can be easily fabricated into non-woven fabric film due to its large length to diameter ratio. Wang et al prepared the MoS_2-CNT composite film by liquid exfoliation and vacuum filtration.[114] The resultant composite film was transferred onto copper foil and used as LIB anode directly. The performance of the MoS_2-CNT composite was related to the thickness of the film, showing a reversible capacity of 990 mAh/g after 100 cycles with a thickness of 1 μm. Another binder-free CNT-MoS_2 composite was prepared by Lu et al via hydrothermal growth of MoS_2 on the outer surface of CNT, which was pre-deposited on the stainless steel substrate by CVD.[115] The composite showed impressive electrochemical performance, with a reversible capacity of 1300 mAh/g at 0.2 A/g. Not only the outer surface, ultranarrow MoS_2 nanoribbons with width of 1-4 nm and thickness of 0.6-2 nm were grown on the inner space of CNT via capillarity followed by sulfurization.[56] This novel mixed low-dimensional nanostructure is believed a promising candidate for high performance LIB anode material. Similar to CNT, CNF is another promising 1D substrate, which possess the advantages of high strength, high conductivity, easy to weave and low cost. Thin MoS_2 nanoflakes were hydrothermally grown on the surface of CNF-derived woven cloth.[59,116] The resultant hybrid cloth showed high

mechanical strength and flexibility, and was fabricated into a flexible full cell directly. This cell demonstrated good cycling stability under continuous bending.

Except for the graphene and CNT/CNF, a variety of organic materials were used as the carbon precursors and to fabricate MoS_2/C nanocomposites, which include poly(vinylpyrrolidone) (PVP),[117] glucose,[118] sucrose,[119] dopamine (DOPA),[120] sulfonated polystyrene,[121] resorcinol-formaldehyde,[122] etc. An impressive work was done by Zhu et al, who prepared 1D carbon nanowires embedded with MoS_2 nanodots via carbonization of PVP and $(NH4)_2MoS_4$, as shown in Figure 2.11.[123] The different storage mechanisms, insertion, conversion and interfacial storage were blurred due to ultrasmall size of MoS_2 (ca. 0.6 nm in thickness and 4 nm in length), leading to an almost diffusion less and nucleation free electrochemical process. Yu et al. prepared carbon nanofibers from glucose and decorated them with MoS_2 nanosheets.[124] A synergistic effect was observed between the two components, triggering a step oxidation of Mo to Mo^{6+} in the charge process. Jiang et al fabricated a MoS_2-carbon superstructure via hydrothermal synthesis of MoS_2 in the presence of oleic acid, amidation of oleic acid with DOPA, followed by self-polymerization of DOPA and carbonization. The composites exhibited superior cycling stability and rate capability due to the ideal interface contact.[125] Chen et al. published a series of works based on the hydrothermal growth of MoS_2 with glucose and L-cysteine.[126-128] They found that the presence of glucose-derived amorphous carbon inhibited the growth of MoS_2 and stabilized the disordered structure, thereby resulting in high reversible capacity and cycling stability. They also claimed that the growth of MoS_2 could be further optimized by cationic or Gemini surfactants because of their interaction with the MoS_2 precursors. MoS_2 with different structure and morphology were synthesized by varying the concentration of surfactant.[61,129-131]

As an alternative to carbonaceous materials, conducting polymers were also used for the fabrication of MoS_2-based composite due to their soft molecular structure and moderate conductivity. Hierarchical MoS_2/PANI nanowires were prepared via polymerization and sulfurization of a special designed precursor, $Mo_3O_{10}(C_6H_8N)_2$[132,133] The ultrathin MoS_2 nanosheets were evenly integrated with PANI throughout the whole nanowire. This

unique organic-inorganic architecture rendered the MoS_2/PANI nanowires improved Li^+ storage properties.

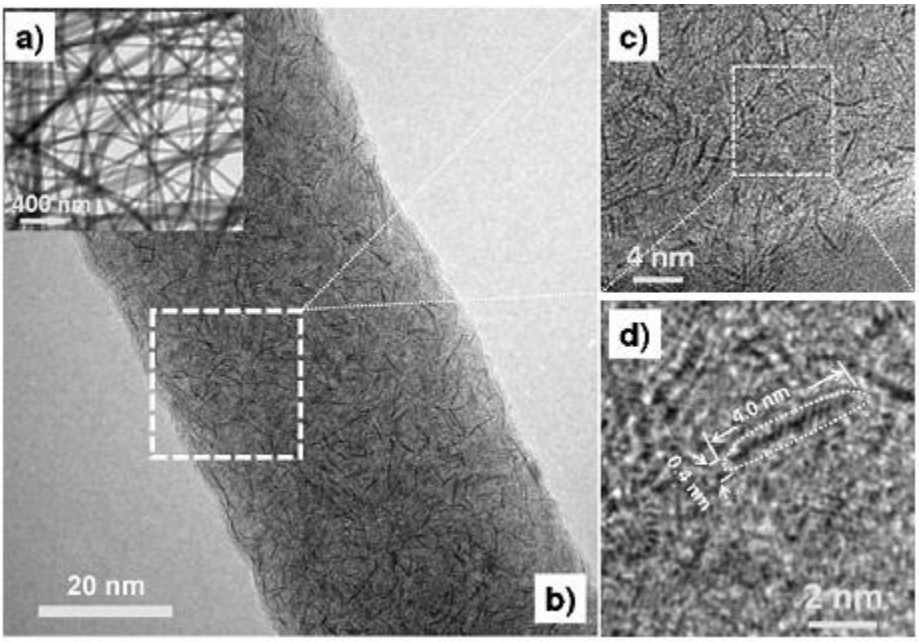

Figure 2.11 TEM images showing the ultrasmall MoS_2 monolayers embedded in CNF.

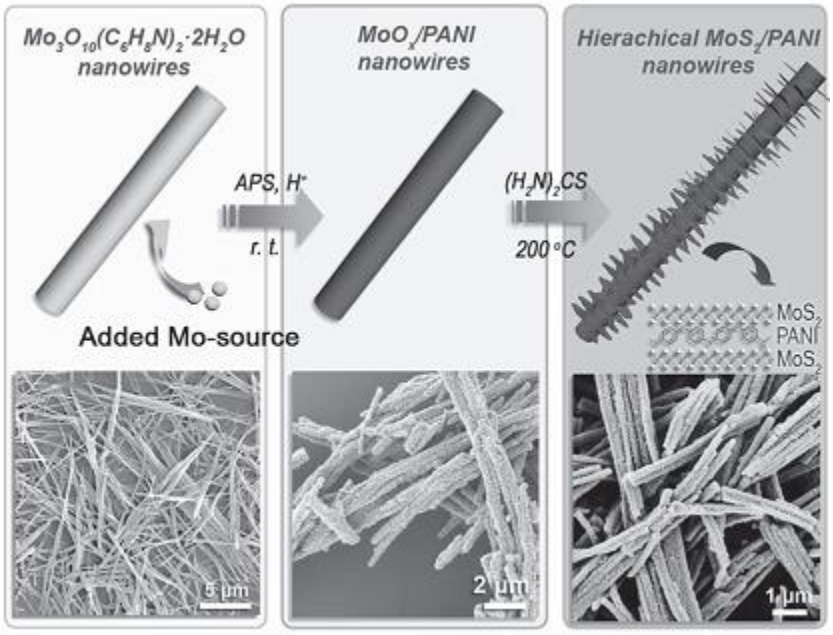

Figure 2.12 Scheme for the preparation of MoS_2/PANI nanowires.

Last but not least, other than the structure design of MoS_2 and the integration with

conducting agents, the performance of MoS_2-based anodes could be enhanced by adding certain additives, for example, poly(ethylene oxide) (PEO), a widely used polymer electrolyte.[89,134,135] The addition of PEO accelerated the Li^+ transportation between the electrode and electrolyte, inhibited the aggregation or restacking of MoS_2 during cycling and accommodated more Li^+ between the MoS_2 and PEO interfaces, thus resulting in much improved cycling stability and rate capability.

2.4 Questions to Answer Based on Literature

Based on the equations 1.1 and 1.2, the theoretical capacity of MoS_2 is only 670 mAh/g, which is well below the most reported numbers in literatures. We believe there are four additional while by no means mutually exclusive contributions to the net Li^+ storage.

i. As mentioned above, after the first cycle, majority of MoS_2 is converted to Mo and S, and the Li_2S/S couple dominant the following redox process. Clearly, the specific capacity of MoS_2 will be largely determined by the S content. Bulk MoS_2 is usually obtained from mineral and is stoichiometric. However, for the various nanostructured MoS_2 especially those prepared from the bottom up method, the real S content may be slightly deviated from the theoretical value. An excess of S source is used in almost all the literatures to ensure the complete sulfurization of the Mo species. As a result, all the defects sites and edges of the MoS_2 crystal will be terminated by S. That also explains why smaller and more disordered structure delivers better electrochemical performance.

ii. In the bulk form, Mo is not active towards Li^+. However, the story is always different when it downs to the nano-size, as the activity of Mo nanoparticles may be greatly enhanced due to their large surface area and high surface energy.[89] Therefore, the Mo nanoparticles derived from the decomposition of MoS_2 may also participate in the reversible cycling process, either by absorption or alloying of Li^+, thus accommodating a large amount of Li^+.

iii. Materials with nanostructures are always possessing larger specific surface areas than their bulk forms. As a result, certain amount of Li^+ will be stored at the near surface or interfaces of the sample, similar to that of supercapacitors[136]. This capacitive behavior may also take place for nanostructured MoS_2. Extra Li^+ may be stored at the surface of

MoS_2 anode or interfaces of Li_2S and Mo.

iv. The specific capacity of pure MoS_2 anode is always lower than 900 mAh/g regardless of structure, morphology or crystallinity. The top numbers especially those above 1000 mAh/g are always obtained in the presence of a carbon phase. We believe that the contribution of nanostructured carbon to the total capacity may be either underestimated or perhaps even not take into account at all. On one hand, the defect-rich carbon may deliver a much higher specific capacity than that of graphite, even approaching 1000 mAh/g;[137] On the other, in many cases, disordered MoS_2 domains are dispersed within the defect-rich carbon phase, triggering a synergistic interaction between them, which can't be captured by the simple mixture rule. The intimate contact of MoS_2 and carbon creates abundant interfaces. This atomic interface system will benefit a more prominent Li^+ storage capability.

2.5 Questions Remaining

Though thin MoS_2 nanosheets can be obtained through various methods, the large-scale aqueous production of high crystalline thin MoS_2 nanosheets is still restricted by the low stability of the suspension as well as low concentration. As for the SL-MoS_2 nanosheets, the synthetic method is even more challenging because of their strong restacking tendency. As mentioned above, the presence of atomic interfaces plays an important role in Li^+ storage. However, to the best of our knowledge, few attempts have been tried to optimize the electrochemical performance of MoS_2 through the engineering of interface. Moreover, as a 2D layered material with excellent lubricating property, MoS_2 paper may exhibits good flexibility, similar to that of graphene paper. This emerging area, however, is seldom reported and should be also paid special attention to.

Reference:

[1] R. G. Dickinson and L. Pauling. *J. Am. Chem. Soc.* **1923**, 45, 1466-1471.

[2] F. Jellinek, G. Brauer and H. Muller. *Nature*. **1960**, 185, 376-377.

[3] T. Stephenson, Z. Li, B. Olsen and D. Mitlin. *Energy Environ. Sci.* **2014**, 7, 209-231.

[4] L. Wang, Z. Xu, W. Wang and X. Bai. *J. Am. Chem. Soc.* **2014**, 136, 6693-6697.

[5] G. Eda, H. Yamaguchi, D. Voiry, T. Fujita, M. Chen and M. Chhowalla. *Nano Lett.* **2011**, 11, 5111-5116.

[6] J. Heising and M. G. Kanatzidis. *J. Am. Chem. Soc.* **1999**, 121, 11720-11732.

[7] E. Benavente, M. Santa Ana, F. Mendiz ábal and G. Gonz ález. *Coord. Chem. Rev.* **2002**, 224, 87-109.

[8] F. Wypych, K. Sollmann and R. Sch öllhorn. *Mater. Res. Bull.* **1992**, 27, 545-553.

[9] F. Wypych and R. Schollhorn. *J. Chem. Soc., Chem. Commun.* **1992**, 1386-1388.

[10] K. F. Mak, C. Lee, J. Hone, J. Shan and T. F. Heinz. *Phys. Rev. Lett.* **2010**, 105, 136805.

[11] R. Ganatra and Q. Zhang. *ACS nano*. **2014**, 8, 4074-4099.

[12] H. Wang, P. Skeldon and G. Thompson. *Surf. Coat. Technol.* **1997**, 91, 200-207.

[13] T. Le Mogne, C. Donnet, J. M. Martin, A. Tonck, N. Millard-Pinard, S. Fayeulle and N. Moncoffre. *J. Vac. Sci. Technol., A.* **1994**, 12, 1998-2004.

[14] D. Liu, X. Chen, D. Li, F. Wang, X. Luo and B. Yang. *J. Mol. Struct.* **2010**, 980, 66-71.

[15] V. Alexiev, R. Prins and T. Weber. *Phys. Chem. Chem. Phys.* **2000**, 2, 1815-1827.

[16] A. Splendiani, L. Sun, Y. Zhang, T. Li, J. Kim, C.-Y. Chim, G. Galli and F. Wang. *Nano Lett.* **2010**, 10, 1271-1275.

[17] S. S. Chou, B. Kaehr, J. Kim, B. M. Foley, M. De, P. E. Hopkins, J. Huang, C. J. Brinker and V. P. Dravid. *Angew. Chem., Int. Ed.* **2013**, 52, 4160-4164.

[18] J. Zheng, H. Zhang, S. Dong, Y. Liu, C. Tai Nai, H. Suk Shin, H. Young Jeong, B. Liu and K. Ping Loh. *Nat. Commun.* **2014**, 5.

[19] V. Nicolosi, M. Chhowalla, M. G. Kanatzidis, M. S. Strano and J. N. Coleman. *Science*. **2013**, 340.

[20] A. Castellanos-Gomez, M. Barkelid, A. M. Goossens, V. E. Calado, H. S. J. van der Zant and G. A. Steele. *Nano Lett.* **2012**, 12, 3187-3192.

[21] J. Jeon, S. K. Jang, S. M. Jeon, G. Yoo, Y. H. Jang, J.-H. Park and S. Lee. *Nanoscale*. **2015**, 7, 1688-1695.

[22] H. S. S. Ramakrishna Matte, A. Gomathi, A. K. Manna, D. J. Late, R. Datta, S. K. Pati and C. N. R. Rao. *Angew. Chem., Int. Ed.* **2010**, 49, 4059-4062.

[23] K. S. Novoselov, A. K. Geim, S. V. Morozov, D. Jiang, Y. Zhang, S. V. Dubonos, I. V. Grigorieva and A. A. Firsov. *Science*. **2004**, 306, 666-669.

[24] K. S. Novoselov, D. Jiang, F. Schedin, T. J. Booth, V. V. Khotkevich, S. V. Morozov and A. K. Geim. *Proc. Natl. Acad. Sci. U. S. A.* **2005**, 102, 10451-10453.

[25] RadisavljevicB, RadenovicA, BrivioJ, GiacomettiV and KisA. *Nat. Nanotechnol.* **2011**, 6, 147-150.

[26] K. E. Dungey, M. D. Curtis and J. E. Penner-Hahn. *Chem. Mater.* **1998**, 10, 2152-2161.

[27] M. A. Santa-Ana, V. Sanchez and G. Gonzalez. *Electrochim. Acta*. **1995**, 40, 1773-1775.

[28] Z. Zeng, Z. Yin, X. Huang, H. Li, Q. He, G. Lu, F. Boey and H. Zhang. *Angew. Chem., Int. Ed.* **2011**, 50, 11093-11097.

[29] J. Zheng, H. Zhang, S. Dong, Y. Liu, C. Tai Nai, H. Suk Shin, H. Young Jeong, B. Liu and K. Ping Loh. *Nat. Commun.* **2014**, 5, 2995.

[30] J. N. Coleman, M. Lotya, A. O'Neill, S. D. Bergin, P. J. King, U. Khan, K. Young, A. Gaucher, S. De and R. J. Smith. *Science*. **2011**, 331, 568-571.

[31] K. Lee, H. Y. Kim, M. Lotya, J. N. Coleman, G. T. Kim and G. S. Duesberg. *Adv. Mater.* **2011**, 23, 4178-4182.

[32] J. N. Coleman. *Adv. Funct. Mater.* **2009**, 19, 3680-3695.

[33] G. Cunningham, M. Lotya, C. S. Cucinotta, S. Sanvito, S. D. Bergin, R. Menzel, M. S. Shaffer and J. N. Coleman. *ACS nano*. **2012**, 6, 3468-3480.

[34] K.-G. Zhou, N.-N. Mao, H.-X. Wang, Y. Peng and H.-L. Zhang. *Angew. Chem., Int. Ed.* **2011**, 50, 10839-10842.

[35] Y. Yao, L. Tolentino, Z. Yang, X. Song, W. Zhang, Y. Chen and C.-p. Wong. *Adv. Funct. Mater.* **2013**, 23, 3577-3583.

[36] M. D. J. Quinn, N. H. Ho and S. M. Notley. *ACS Appl. Mater. Interfaces*. **2013**, 5, 12751-12756.

[37] W. Yin, L. Yan, J. Yu, G. Tian, L. Zhou, X. Zheng, X. Zhang, Y. Yong, J. Li, Z. Gu and Y. Zhao. *ACS nano*. **2014**, 8, 6922-6933.

[38] Y. Yao, Z. Lin, Z. Li, X. Song, K.-S. Moon and C.-p. Wong. *J. Mater. Chem.* **2012**, 22, 13494-13499.

[39] W. Wenseleers, I. I. Vlasov, E. Goovaerts, E. D. Obraztsova, A. S. Lobach and A. Bouwen. *Adv. Funct. Mater.* **2004**, 14, 1105-1112.

[40] R. J. Smith, P. J. King, M. Lotya, C. Wirtz, U. Khan, S. De, A. O'Neill, G. S. Duesberg, J. C. Grunlan and G. Moriarty. *Adv. Mater.* **2011**, 23, 3944-3948.

[41] X. C. Song, Y. Zhao, Y. F. Zheng and E. Yang. *Adv. Eng. Mater.* **2007**, 9, 96-98.

[42] T. P. Prasad, E. Diemann and A. Müller. *J. Inorg. Nucl. Chem.* **1973**, 35, 1895-1904.

[43] J. L. Brito, M. Ilija and P. Hernández. *Thermochim. Acta*. **1995**, 256, 325-338.

[44] K.-K. Liu, W. Zhang, Y.-H. Lee, Y.-C. Lin, M.-T. Chang, C.-Y. Su, C.-S. Chang, H. Li, Y. Shi, H. Zhang, C.-S. Lai and L.-J. Li. *Nano Lett.* **2012**, 12, 1538-1544.

[45] Y. Shi, W. Zhou, A.-Y. Lu, W. Fang, Y.-H. Lee, A. L. Hsu, S. M. Kim, K. K. Kim, H. Y. Yang, L.-J. Li, J.-C. Idrobo and J. Kong. *Nano Lett.* **2012**, 12, 2784-2791.

[46] C. Altavilla, M. Sarno and P. Ciambelli. *Chem. Mater.* **2011**, 23, 3879-3885.

[47] Y. han, Z. Liu, S. Najmaei, P. M. Ajayan and J. Lou. *Small*. **2012**, 8, 966-971.

[48] K. M. McCreary, A. T. Hanbicki, J. T. Robinson, E. Cobas, J. C. Culbertson, A. L. Friedman, G. G. Jernigan and B. T. Jonker. *Adv. Funct. Mater.* **2014**, 24, 6449-6454.

[49] Y.-H. Lee, X.-Q. Zhang, W. Zhang, M.-T. Chang, C.-T. Lin, K.-D. Chang, Y.-C. Yu, J. T.-W. Wang, C.-S. Chang, L.-J. Li and T.-W. Lin. *Adv. Mater.* **2012**, 24, 2320-2325.

[50] Y.-C. Lin, W. Zhang, J.-K. Huang, K.-K. Liu, Y.-H. Lee, C.-T. Liang, C.-W. Chu and L.-J. Li. *Nanoscale*. **2012**, 4, 6637-6641.

[51] H. Hwang, H. Kim and J. Cho. *Nano Lett.* **2011**, 11, 4826-4830.

[52] Z. Wang, H. Li, Z. Liu, Z. Shi, J. Lu, K. Suenaga, S.-K. Joung, T. Okazaki, Z. Gu, J. Zhou, Z. Gao, G. Li, S. Sanvito, E. Wang and S. Iijima. *J. Am. Chem. Soc.* **2010**, 132, 13840-13847.

[53] C. Feng, J. Ma, H. Li, R. Zeng, Z. Guo and H. Liu. *Mater. Res. Bull.* **2009**, 44, 1811-1815.

[54] K. Chang, D. Geng, X. Li, J. Yang, Y. Tang, M. Cai, R. Li and X. Sun. *Adv. Energy Mater.* **2013**, 3, 839-844.

[55] X. Duan, C. Wang, J. C. Shaw, R. Cheng, Y. Chen, H. Li, X. Wu, Y. Tang, Q. Zhang, A. Pan, J. Jiang, R. Yu, Y. Huang and X. Duan. *Nat. Nanotechnol.* **2014**, 9, 1024-1030.

[56] Y.-C. Lin, N. Lu, N. Perea-Lopez, J. Li, Z. Lin, X. Peng, C. H. Lee, C. Sun, L. Calderin, P. N. Browning, M. S. Bresnehan, M. J. Kim, T. S. Mayer, M. Terrones and J. A. Robinson. *ACS nano*. **2014**, 8, 3715-3723.

[57] X. Fang, X. Yu, S. Liao, Y. Shi, Y.-S. Hu, Z. Wang, G. D. Stucky and L. Chen. *Microporous Mesoporous Mater.* **2012**, 151, 418-423.

[58] G. Nagaraju, C. Tharamani, G. Chandrappa and J. Livage. *Nanoscale Res. Lett.* **2007**, 2, 461-468.

[59] H. Yu, C. Zhu, K. Zhang, Y. Chen, C. Li, P. Gao, P. Yang and Q. Ouyang. *J. Mater. Chem. A*. **2014**, 2, 4551-4557.

[60] C. N. R. Rao and A. Nag. *Eur. J. Inorg. Chem.* **2010**, 2010, 4244-4250.

[61] L. Ma, J. Ye, W. Chen, D. Chen and J. Yang Lee. *Nano Energy*. **2014**, 10, 144-152.

[62] S. Balendhran, J. Z. Ou, M. Bhaskaran, S. Sriram, S. Ippolito, Z. Vasic, E. Kats, S. Bhargava, S. Zhuiykov and K. Kalantar-Zadeh. *Nanoscale*. **2012**, 4, 461-466.

[63] S. Wu, C. Huang, G. Aivazian, J. S. Ross, D. H. Cobden and X. Xu. *ACS nano*. **2013**, 7, 2768-2772.

[64] Y. Peng, Z. Meng, C. Zhong, J. Lu, W. Yu, Y. Jia and Y. Qian. *Chem. Lett.* **2001**, 30, 772-773.

[65] J. Xie, H. Zhang, S. Li, R. Wang, X. Sun, M. Zhou, J. Zhou, X. W. D. Lou and Y. Xie. *Adv. Mater.* **2013**, 25, 5807-5813.

[66] H. Lin, X. Chen, H. Li, M. Yang and Y. Qi. *Mater. Lett.* **2010**, 64, 1748-1750.

[67] M. Al-Mamun, H. Zhang, P. Liu, Y. Wang, J. Cao and H. Zhao. *RSC Adv.* **2014**, 4, 21277-21283.

[68] M. Wang, G. Li, H. Xu, Y. Qian and J. Yang. *ACS Appl. Mater. Interfaces*. **2013**, 5, 1003-1008.

[69] H. Li, W. Li, L. Ma, W. Chen and J. Wang. *J. Alloys Compd.* **2009**, 471, 442-447.

[70] X. Wang, J. Ding, S. Yao, X. Wu, Q. Feng, Z. Wang and B. Geng. *J. Mater. Chem. A.* **2014**, 2, 15958-15963.

[71] I. Song, C. Park and H. C. Choi. *RSC Adv.* **2015**, 5, 7495-7514.

[72] X. Li and H. Zhu. *J. Materiomics*. **2015**, 1, 33-44.

[73] C. Tan and H. Zhang. *Chem. Soc. Rev.* **2015**, 44, 2713-2731.

[74] R. R. Haering, J. A. R. Stiles and K. Brandt, US Patent 4224390, 1980.

[75] Y. Miki, D. Nakazato, H. Ikuta, T. Uchida and M. Wakihara. *J. Power Sources*. **1995**, 54, 508-510.

[76] C. Julien, S. I. Saikh and G. A. Nazri. *Mater. Sci. Eng., B.* **1992**, 15, 73-77.

[77] N. Imanishi, K. Kanamura and Z. i. Takehara. *J. Electrochem. Soc.* **1992**, 139, 2082-2087.

[78] X. Chen, J. He, D. Srivastava and J. Li. *Appl. Phys. Lett.* **2012**, 100, -.

[79] K. Chrissafis, M. Zamani, K. Kambas, J. Stoemenos, N. A. Economou, I. Samaras and C. Julien. *Mater. Sci. Eng., B.* **1989**, 3, 145-151.

[80] V. Yufit, M. Nathan, D. Golodnitsky and E. Peled. *J. Power Sources*. **2003**, 122, 169-173.

[81] A. V. Murugan, M. Quintin, M.-H. Delville, G. Campet, C. S. Gopinath and K. Vijayamohanan. *J. Power Sources*. **2006**, 156, 615-619.

[82] E. Shembel, R. Apostolova, I. Kirsanova and V. Tysyachny. *J. Solid State Electrochem.* **2008**, 12, 1151-1157.

[83] Y. Liu, X. He, D. Hanlon, A. Harvey, U. Khan, Y. Li and J. N. Coleman. *ACS nano*. **2016**.

[84] C. Zhao, X. Wang, J. Kong, J. M. Ang, P. S. Lee, Z. Liu and X. Lu. *ACS Appl. Mater. Interfaces*. **2016**, 8, 2372-2379.

[85] Z. Xu, X. Shen, Q. Zhang, J. Li, L. Kong, L. Cao and J. Huang. *Part. Part. Syst. Charact.* **2016**, n/a-n/a.

[86] D. Ren, Y. Hu, H. Jiang, Z. Deng, S. Petr, H. Jiang and C. Li. *ACS Sustainable Chem. Eng.* **2016**, 4, 1148-1153.

[87] J. Zhou, J. Qin, N. Zhao, C. Shi, E.-Z. Liu, F. He, J. Li and C. He. *J. Mater. Chem. A.* **2016**.

[88] J. Kong, C. Zhao, Y. Wei, S. L. Phua, Y. Dong and X. Lu. *J. Mater. Chem. A*. **2014**, 2, 15191-15199.

[89] J. Xiao, X. Wang, X.-Q. Yang, S. Xun, G. Liu, P. K. Koech, J. Liu and J. P. Lemmon. *Adv. Funct. Mater*. **2011**, 21, 2840-2846.

[90] Q. Wang and J. Li. *J. Phys. Chem. C*. **2007**, 111, 1675-1682.

[91] Y. Kim and J. B. Goodenough. *J. Phys. Chem. C*. **2008**, 112, 15060-15064.

[92] A. Débart, L. Dupont, R. Patrice and J. M. Tarascon. *Solid State Sci*. **2006**, 8, 640-651.

[93] Y. Zhou, C. Zhou, Q. Li, C. Yan, B. Han, K. Xia, Q. Gao and J. Wu. *Adv. Mater*. **2015**, 27, 3840-3840.

[94] R. Fang, S. Zhao, P. Hou, M. Cheng, S. Wang, H.-M. Cheng, C. Liu and F. Li. *Adv. Mater*. **2016**, 28, 3374-3382.

[95] X. Fang, X. Guo, Y. Mao, C. Hua, L. Shen, Y. Hu, Z. Wang, F. Wu and L. Chen. *Chem. - Asian J*. **2012**, 7, 1013-1017.

[96] X. Fang, C. Hua, X. Guo, Y. Hu, Z. Wang, X. Gao, F. Wu, J. Wang and L. Chen. *Electrochim. Acta*. **2012**, 81, 155-160.

[97] U. K. Sen, P. Johari, S. Basu, C. Nayak and S. Mitra. *Nanoscale*. **2014**, 6, 10243-10254.

[98] S. Ding, D. Zhang, J. S. Chen and X. W. Lou. *Nanoscale*. **2012**, 4, 95-98.

[99] U. K. Sen and S. Mitra. *ACS Appl. Mater. Interfaces*. **2013**, 5, 1240-1247.

[100] G. Du, Z. Guo, S. Wang, R. Zeng, Z. Chen and H. Liu. *Chem. Commun.* . **2010**, 46, 1106-1108.

[101] H. Liu, D. Su, R. Zhou, B. Sun, G. Wang and S. Z. Qiao. *Adv. Energy Mater*. **2012**, 2, 970-975.

[102] X. Cao, Y. Shi, W. Shi, X. Rui, Q. Yan, J. Kong and H. Zhang. *Small*. **2013**, 9, 3433-3438.

[103] V. H. Pham, K.-H. Kim, D.-W. Jung, K. Singh, E.-S. Oh and J. S. Chung. *J. Power Sources*. **2013**, 244, 280-286.

[104] Y. Hu, X. Li, A. Lushington, M. Cai, D. Geng, M. N. Banis, R. Li and X. Sun. *ECS J. Solid State Sci. Technol.* **2013**, 2, M3034-M3039.

[105] X. Zhou, L.-J. Wan and Y.-G. Guo. *Chem. Commun.* . **2013**, 49, 1838-1840.

[106] D. Kong, H. He, Q. Song, B. Wang, W. Lv, Q.-H. Yang and L. Zhi. *Energy Environ. Sci.* **2014**, 7, 3320-3325.

[107] K. Bindumadhavan, S. K. Srivastava and S. Mahanty. *Chem. Commun.* . **2013**, 49, 1823-1825.

[108] I. Zafiropoulou, M. S. Katsiotis, N. Boukos, M. A. Karakassides, S. Stephen, V. Tzitzios, M. Fardis, R. V. Vladea, S. M. Alhassan and G. Papavassiliou. *J. Phys. Chem. C*. **2013**, 117, 10135-10142.

[109] S. Ding, J. S. Chen and X. W. Lou. *Chem. - Eur. J.* **2011**, 17, 13142-13145.

[110] S.-K. Park, S.-H. Yu, S. Woo, B. Quan, D.-C. Lee, M. K. Kim, Y.-E. Sung and Y. Piao. *Dalton Trans.* **2013**, 42, 2399-2405.

[111] S. Wang, X. Jiang, H. Zheng, H. Wu, S.-J. Kim and C. Feng. *Nanosci. Nanotechnol. Lett.* **2012**, 4, 378-383.

[112] H. Yu, C. Ma, B. Ge, Y. Chen, Z. Xu, C. Zhu, C. Li, Q. Ouyang, P. Gao, J. Li, C. Sun, L. Qi, Y. Wang and F. Li. *Chem. - Eur. J.* **2013**, 19, 5818-5823.

[113] J. Wang, J. Liu, D. Chao, J. Yan, J. Lin and Z. X. Shen. *Adv. Mater.* **2014**, 26, 7162-7169.

[114] J. Z. Wang, L. Lu, M. Lotya, J. N. Coleman, S. L. Chou, H. K. Liu, A. I. Minett and J. Chen. *Adv. Energy Mater.* **2013**, 3, 798-805.

[115] C. Lu, W.-w. Liu, H. Li and B. K. Tay. *Chem. Commun.* . **2014**, 50, 3338-3340.

[116] C. Wang, W. Wan, Y. Huang, J. Chen, H. H. Zhou and X. X. Zhang. *Nanoscale*. **2014**, 6, 5351-5358.

[117] J. Shao, Q. Qu, Z. Wan, T. Gao, Z. Zuo and H. Zheng. *ACS Appl. Mater. Interfaces*. **2015**, 7, 22927-22934.

[118] S. Hu, W. Chen, J. Zhou, F. Yin, E. Uchaker, Q. Zhang and G. Cao. *J. Mater. Chem. A*. **2014**.

[119] X. Zhou, L.-J. Wan and Y.-G. Guo. *Nanoscale*. **2012**, 4, 5868-5871.

[120] J.-M. Jeong, K. G. Lee, S.-J. Chang, J. W. Kim, Y.-K. Han, S. J. Lee and B. G. Choi. *Nanoscale*. **2015**, 7, 324-329.

[121] Z. Wan, J. Shao, J. Yun, H. Zheng, T. Gao, M. Shen, Q. Qu and H. Zheng. *Small*. **2014**, 10, 4975-4981.

[122] S. K. Das, R. Mallavajula, N. Jayaprakash and L. A. Archer. *J. Mater. Chem.* **2012**, 22, 12988-12992.

[123] C. Zhu, X. Mu, P. A. van Aken, Y. Yu and J. Maier. *Angew. Chem., Int. Ed.* **2014**, 53, 2152-2156.

[124] F. Zhou, S. Xin, H.-W. Liang, L.-T. Song and S.-H. Yu. *Angew. Chem., Int. Ed.* **2014**, 53, 11552-11556.

[125] H. Jiang, D. Y. Ren, H. F. Wang, Y. J. Hu, S. J. Guo, H. Y. Yuan, P. J. Hu, L. Zhang and C. Z. Li. *Adv. Mater.* **2015**, 27, 3687-3695.

[126] K. Chang and W. Chen. *ACS Nano*. **2011**, 5, 4720-4728.

[127] K. Chang, W. Chen, L. Ma, H. Li, H. Li, F. Huang, Z. Xu, Q. Zhang and J.-Y. Lee. *J. Mater. Chem.* **2011**, 21, 6251-6257.

[128] K. Chang and W. Chen. *J. Mater. Chem.* **2011**, 21, 17175-17184.

[129] Z. Wang, T. Chen, W. Chen, K. Chang, L. Ma, G. Huang, D. Chen and J. Y. Lee. *J. Mater. Chem. A.* **2013**, 1, 2202-2210.

[130] G. Huang, T. Chen, W. Chen, Z. Wang, K. Chang, L. Ma, F. Huang, D. Chen and J. Y. Lee. *Small*. **2013**, 9, 3693-3703.

[131] K. Chang and W. Chen. *Chem. Commun.* . **2011**, 47, 4252-4254.

[132] L. Yang, S. Wang, J. Mao, J. Deng, Q. Gao, Y. Tang and O. G. Schmidt. *Adv. Mater.* **2013**, 25, 1180-1184.

[133] C. Zhang, Z. Wang, Z. Guo and X. W. Lou. *ACS Appl. Mater. Interfaces*. **2012**, 4, 3765-3768.

[134] J. Xiao, D. Choi, L. Cosimbescu, P. Koech, J. Liu and J. P. Lemmon. *Chem. Mater.* **2010**, 22, 4522-4524.

[135] Y.-T. Liu, X.-D. Zhu, Z.-Q. Duan and X.-M. Xie. *Chem. Commun.* . **2013**, 49, 10305-10307.

[136] X. Guo, X. Fang, Y. Mao, Z. Wang, F. Wu and L. Chen. *J. Phys. Chem. C*. **2011**, 115, 3803-3808.

[137] R. Mukherjee, A. V. Thomas, D. Datta, E. Singh, J. Li, O. Eksik, V. B. Shenoy and N. Koratkar. *Nat. Commun.* **2014**, 5.

Chapter 3

Experimental Methodology

In this chapter, all the experimental details of my PhD work are presented. It starts with the rationale for selection of synthetic methods, including exfoliation, electrospinning, hydrothermal treatment and self-assembly. Their advantages and the underlying mechanisms are demonstrated. The following parts are the basic principles of some important characterization techniques used in my PhD work, the understanding of which is crucial for correct data collection and analysis. The detailed synthesis procedures are then presented, including the aqueous exfoliation of bulk MoS_2, the synthesis of MoS_2/C hybrid nanofibrous mats, SL-MoS_2/C nanocomposite and SL-MoS_2/NDG heterostructure.

3.1 Rationale for Selection of Methods

3.1.1 Aqueous exfoliation

Liquid-phase exfoliation is so far the most suitable route for large scale production of high quality MoS_2 nanosheets.[1] Although MoS_2 monolayers produced by scotch tape, CVD, etc. is ideal for electronics and optoeletronic devices, these methods are of extreme low efficiency or high cost, and therefore are restricted to the lab-scale. To meet the requirements of a range of applications such as thermoelectrics, supercapacitors and LIBs, mass production of MoS_2 nanosheets should be realized with the advantages of low cost and simplicity.

Compared to the exfoliation in organic solvents, aqueous exfoliation of MoS_2 possesses special economic and environmental superiority. The exfoliation of MoS_2 in water, however, is challenging owing to its hydrophobic nature. The highest concentration of MoS_2 dispersion is only 10^{-4} mg/ml. One method to address this issue is to use surfactants, which allows the exfoliated nanosheets to remain suspended.

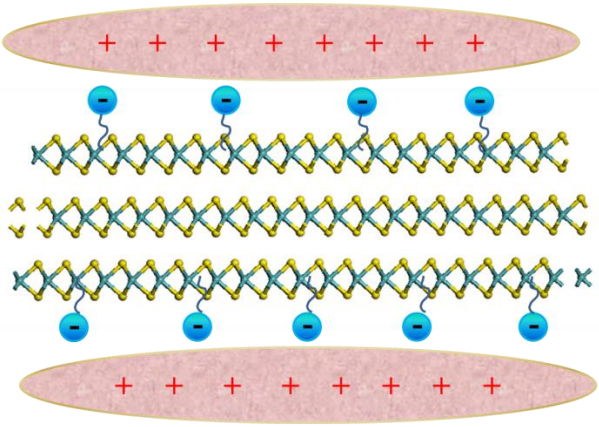

Figure 3.1 Schematic of the electric double layer on the surface of MoS_2.

The stabilization of colloids, taking MoS_2 as an example, by surfactant usually relies on two factors: surface charge and steric hindrance. When MoS_2 is exfoliated in the presence of surfactant, the surfactant molecules are absorbed on the exfoliated nanosheets due to intermolecular interactions. If the surfactant is ionic, the hydrolysis of surfactant molecules will lead to a charged surface of the nanosheets. At the same time, a layer of

counter-ions are attracted to the adjacent surface of surfactant, forming an electric double layer, as shown in Figure 3.1. The MoS_2 naonosheets are wrapped by the diffusion cloud of counter ions due to their Brownian motion, and appear to carry an effective surface charge. The electrostatic repulsion raised stabilizes the MoS_2 nanosheets and prevents their restacking. The magnitude and sign of this charge could be characterized by the zeta potential, ζ.

The repulsion potential between adjacent MoS_2 nanosheets can be calculated according to the following equation:[2]

$$V(D) = Be^{-\kappa D} \qquad (3.1)$$

Where D is the distance between two separated nanosheets; κ is the screening length and is related to the thickness of the electric double layer; B depends on κ, ζ and geometry of the nanosheets.

The attraction between neighbouring MoS_2 nanosheets is inversely proportional to the distance, which can be expressed as:[3]

$$V(D) = -A/D \qquad (3.2)$$

Where A depends on the geometry and density of the MoS_2 nanosheets. Therefore, the total potential is the sum of the attractive and repulsive components.

$$V_T(D) = -A/D + Be^{-\kappa D} \qquad (3.3)$$

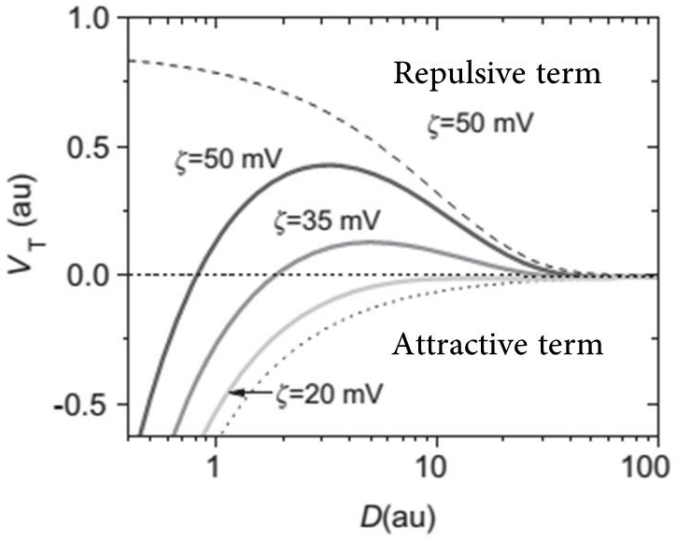

Figure 3.2 Graph showing the total interaction potentials with different zeta potentials. The dash lines show the attractive and repulsive components.

The graph of equation 3.3 is shown in Figure 3.2. The van der Waals attraction dominants at low D and decreases sharply with the increasing of D. As a result, a potential barrier appears at intermediate D before it falls. This potential barrier is the repulsion force that stabilized the MoS_2 nanosheets. Clearly, higher zeta potential induces higher potential barrier. Thus, for the dispersion of MoS_2, its stabilization is determined by the type (ζ) and concentration (κ) of the surfactant.

Steric hindrance is another factor that has to be considered, especially when the surfactant possesses high molecular weight. As we all know, for an isolated system, the increase of entropy is a spontaneous process until an equilibrium state is reached. This is the origin of the repulsion force. Assuming the MoS_2 dispersion have been stabilized by the absorption of surfactant, if the nanosheets approach to each other, the possible conformations of the attached polymer chains will be reduced due to their interaction in the overlapped space, resulting in a reduction in entropy and an increment in free energy. From afar, it looks like a repulsive force that stabilizes the MoS_2 dispersion.[4] The expression of this steric repulsion takes a similar form to the repulsion raised by surface charge:

$$V(D) = B' e^{-D/L} \qquad (3.4)$$

Where B ´and L depend on the coverage and thickness of the coating, respectively. Since the attractive component is the same, the overall interactive potential could be written as:

$$V(D) = -A/D + B' e^{-D/L} \qquad (3.5)$$

which has a similar shape to that of Figure 3.2.

3.1.2 Electrospinning

3.1.2.1 Principles and advantages

1D nanostructure has gained great interest for decades for energy conversion and storage devices due to the dependence of properties on directionality. In the LIBs field, various 1D nanostructures, such as nanorods, nanowires and nanofibers have been reported and show great promise in enhancing the electrochemical performances. The nano-scaled dimension increases the specific surface area and exposes high fraction of atoms, which provide more Li^+ reaction sites and shorter Li^+ diffusion path, hence enhancing the

charge transfer ability and making insertion/extraction process much easier. The large length to diameter ratio further reduces the internal resistance and facilitates the charge transfer.

Conventionally, 1D nanostructure can be synthesized via the bottom-up strategy, for example, CVD or template-assisted route. These methods, however, usually involve tedious process or harsh synthetic conditions. In recently years, an "old" technique, electrospinning, has regained people's interest and been explored as a promising method for the mass production of continuous1D nanofibers.[5,6]

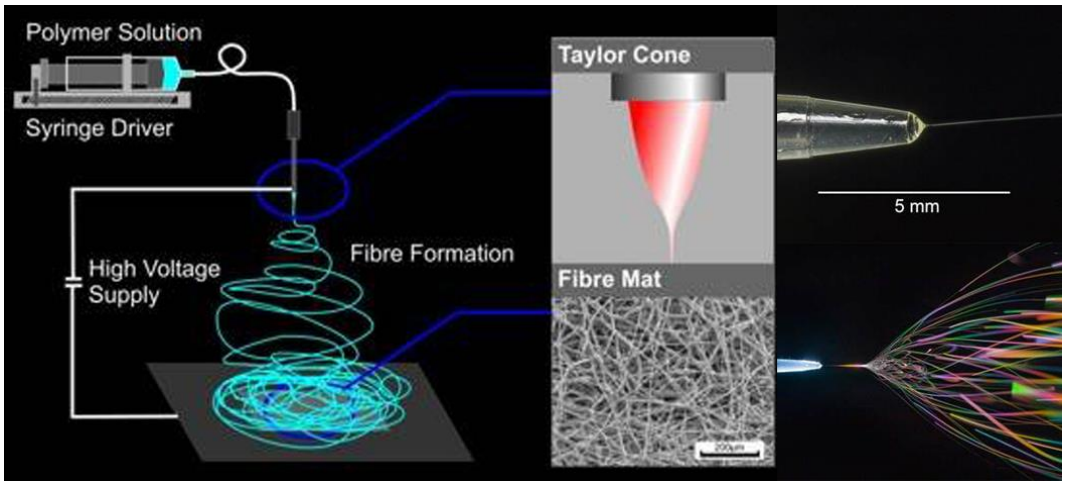

Figure 3.3 Scheme of a conventional electrospinning setup.

The principle of electrospinning is simple and straight-forward. Generally speaking, electrospinning shares characteristics of both electrospraying and conventional solution spinning, relying on strong electrical field to draw very fine fibers from charged droplet. A conventional setup for electrospinning is schematically shown in Figure 3.3. It consists of three major components: a high voltage power supply, a spinneret and a grounded collector (typically a metal plate). During electrospinning, a viscoelastic solution of polymers is delivered continuously by a pump system to the spinneret at a certain feeding rate, while the solution at the tip is charged by high voltage. On the surface of the droplet, the electric repulsion competes with the surface tension, causing an elongation of the droplet, from hemispherical to conical shape. With the increment in voltage, the deformation of the droplet reaches a critical point, where a Taylor cone is formed. The

surface charge repulsion overcomes the surface tension, causing a charged jet erupted from the tip of the Taylor cone. As the jet dries in flight (evaporation of solvent), the mode of the current flow changes from ohmic to convective due to the migration of charges to the fiber surface. The jet is then elongated by a whipping process caused by electrostatic repulsion, until it is finally deposited on the grounded collector.[7] The elongation and thinning of the fiber resulting from this bending instability leads to the formation of fibers around nanometers (nanofibers).[8] The electrospinning process does not require the use of coagulation chemistry or high temperatures to produce solid threads from solution, thus making this process particularly suitable for large and complex molecules. Free-standing mats can be obtained after they are peeled off from the collector.

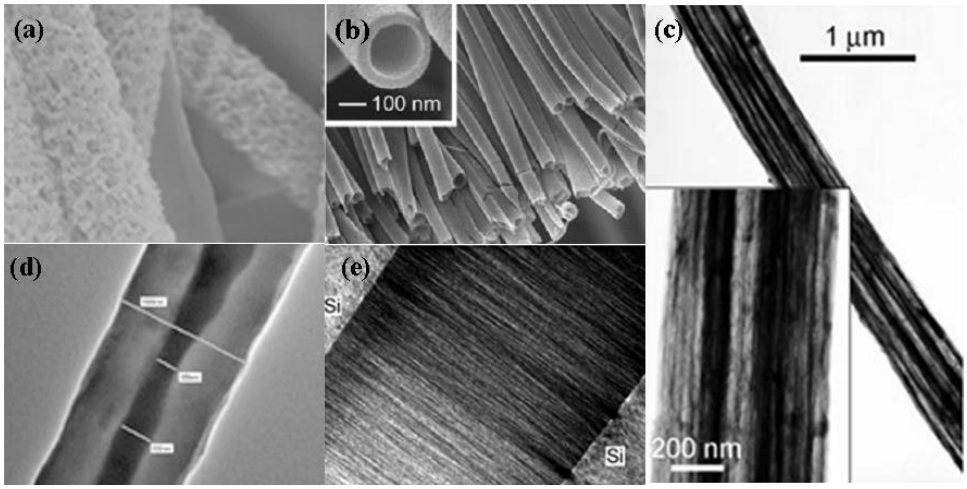

Figure 3.4 Preparation of nanofibers with controllable geometries and architectures by electrospinning: (a) porous, (b) hollow, (c) core-shell, (d) tubulous (e) aligned.

Not only polymers, the applicability of electrospinning has also been extended to hybrids with the advantages of simplicity, efficiency, low cost, high yield and high degree of reproducibility. By employing different types of precursors, polymers have been successfully electrospun with chromophores, magnetic nanoparticles, biomolecules, and metal oxides, etc. What's more, the versatility of electrospinning allows good control of orientation and composition of the nanofibers as well as manipulation their internal morphologies (Figure 3.4). The specific properties related to electrospun nanofibers such as large surface area, high aspect ratios and readily encapsulation of inorganics, make

them very useful for improving performance of energy storage and conversion devices, such as LIBs.

3.2.1.2 CNFs derived from electrospinning

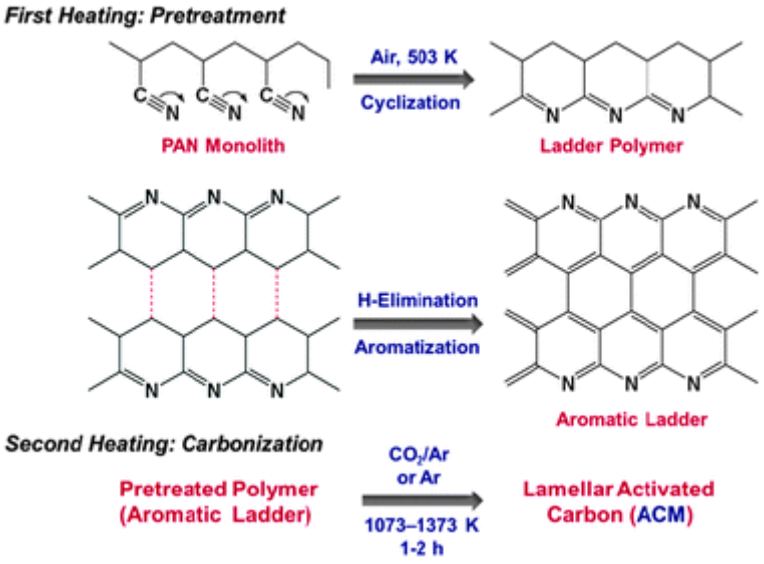

Figure 3.5 Two-steps carbonization of PAN.

In order to convert electrospun polymer nanofibers to CNFs, a heat treatment process called carbonization has to be applied, which may be categorized into several steps, depending on the precursors. Among the various polymers, Polyacrylonitrile (PAN) is most widely used due to its spinnability and high carbon yield. The carbonization of PAN involves two steps, as shown in Figure 3.4.[9] A so-called pretreatment process is essential to keep fibrous morphology. PAN is first cross-linked to a ladder structure by transforming C≡N to C=N bonds. Then an aromatization occurs through the elimination of H, leading to an infusible aromatic ladder structure. This increases the thermal stability of PAN and minimizes the carbon vaporization at elevated temperatures.[10] The stabilization of PAN usually takes place between 180-300 ^{o}C under atmospheric conditions. Carbonization is then followed, where the aromatic growth proceeds. With the increment of temperature, hydrogen atoms will be firstly removed, while the removal of nitrogen atoms occurs at slightly higher temperature. As a result, high conductive carbon with honeycomb like structure is formed.[11] It should be noted that, the diameter and micro-structure of the CNFs can be facilely tailored by adjusting electrospinning

parameters and carbonization conditions. The polymer nanofibers suffer significant weight loss during the pretreatment and carbonization, which further reduces the dimensions of resultant CNFs.

3.1.3 Hydrothermal synthesis

The hydrothermal synthesis is defined as a complicated physical-chemical reaction in aqueous media at temperature above 100 ^{o}C and pressure above 0.1 MPa. It is a widely used technique in the lab for the fabrication of various inorganic and hybrid materials, particularly because of its ability in precisely controlling the products' morphology and crystallinity.

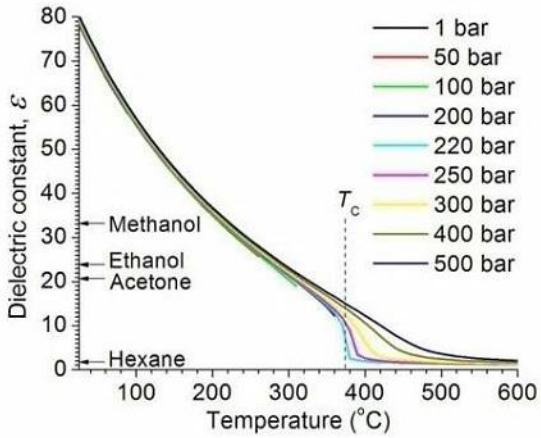

Figure 3.6 The dielectric constants of water at various temperatures and pressures. T_c is the supercritical temperature of water, which is 374 ^{o}C.

The hydrothermal synthesis of materials is actually a crystallization process from the aqueous solution. It exploits that the fundamental properties of water are temperature and pressure dependent. That is, with the increase of temperature and/or pressure, important characteristics of water, such as density, viscosity, dielectric constant, conductivity, etc. are changing. As a result, its ability as a solvent also changes. For example, water can dissolve lots of ionic and polar species at ambient conditions due to its large dielectric constant, as shown in Figure 3.6. However, its dielectric constant drops quickly with the increment of temperature, leading to sharp change in solubility and even precipitation of the solutes at higher temperatures. From another aspect, the low dielectric constant of water increases its solubility for non-polar and organic species, which are added as

surfactants to control morphology and crystallinity of products.

It should be note that, in many works, the term "supercritical" is frequently used to describe a hydrothermal system.[12] One may get confused about these two processes. Do all the hydrothermal reactions fall into the supercritical territory, or vice versa? As shown in Figure 3.6, with the continuous decrease in dielectric constant, a drastic drop occurs at about 374 ^{o}C and 22 MPa. Above this point, the dielectric constant of water approaches to 0 and the distinction between the gas and liquid states is blurred. This new existence form of water is known as the supercritical state. Therefore, the supercritical synthesis is actually an extension of the hydrothermal technique.

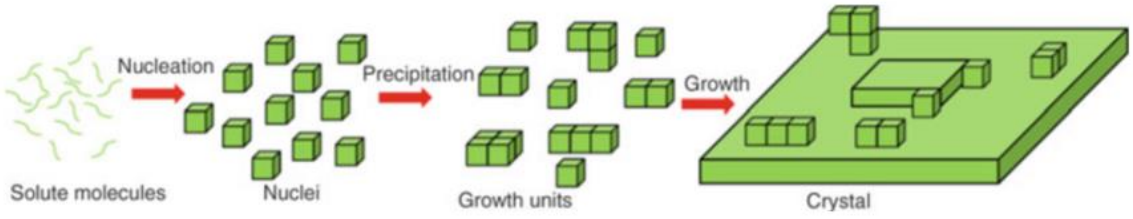

Figure 3.7 The growth mechanism of crystals under hydrothermal conditions.

Generally, two steps are involved in a hydrothermal reaction, crystal nucleation and growth. The growth mechanism of crystals is shown in Figure 3.7. As stated above, the solubility of ionic and polar species decreases at high temperature. When the concentration of solutes exceeds its limit, the solution becomes the supersaturated and nucleation occurs. The critical size of nuclei depends on the degree of supersaturation. Higher supersaturation will decrease the critical radius of stable nuclei. The energy required to overcome the nucleation barrier is provided by the elevated temperature. Subsequently, the nuclei begin to grow to minimize the energy of newly formed high surface area. The mechanism "Ostwald ripening" is typically used to describe this process, although other explanations also exits depending on the properties of the solutions. Small particles usually possess large chemical potentials due to their high surface areas. To reduce the free energy of the system, the newly formed small particles may be re-dissolved, which generates a local concentration gradient of the solution. The solute will then diffuse through solution to the near surface of nuclei, where the concentration is the lowest, and attach to the growth sites, leading to the growth of

crystals. The "Ostwald ripening" usually produces homogenous crystals with narrow size distribution.

3.1.4 Self-assembly

Self-assembly is a process in which randomly oriented components arrange spontaneously through local interactions to form ordered aggregates. The success of self-assembly can be determined by five characteristics, components, interactions, adjustability, environment and mass transport.[13] The building blocks of self-assembly span from molecules to nanometer and even micrometer scale structures. The interactions between them are usually weak and noncovalent, including capillary, electrostatic, π-π and van der Waals interactions, hydrogen bonds and coordination bonds (although belongs to covalent bonds but relatively weak), etc.

3.2 Characterization Techniques

3.2.1 X-ray diffraction

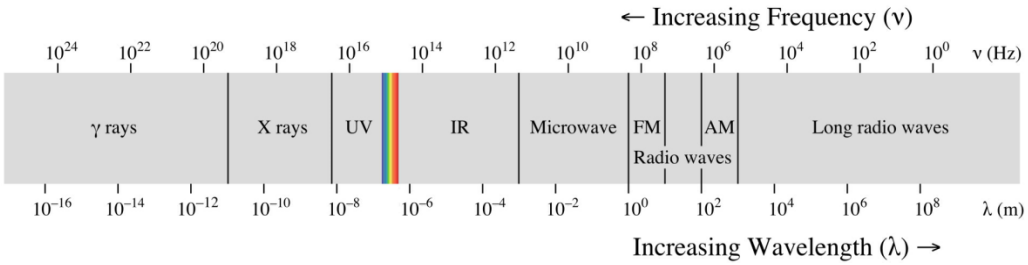

Figure 3.8 Electromagnetic spectrum.

X-ray is a kind of electromagnetic waves with a wavelength of 10^{-8}-10^{-11} nm. Its position in the electromagnetic spectrum is shown in Figure 3.8. Diffraction is a characteristic phenomenon of wave. When an X-ray beam hits atoms, it will be scattered by the atomic orbital electrons, causing a change in amplitude or phase. The scattered X-rays interfere with each other and the sums of them are cancelled out in almost all directions (destructive interference). However, if the atoms within the sample are arranged in a regular pattern (crystalline), in a very few directions, the X-rays will mutually reinforce each other (constructive interference). This energy density distribution caused by X-ray irradiation is referred to as the X-ray Diffraction **(**XRD) pattern.

In real, crystals are 3D and the orientation and interplanar spacing of the lattice planes are defined by Miller indices, *h*, *k*, and *l*. To determine the directions of the X-rays, another three parameters, α, β and γ have to be used, making the 3D diffraction model too complex to handle mathematically. For simplification, a 2D model, Bragg's law is introduced here to demonstrate the formation of a XRD pattern.

$$2d * \sin\theta = n * \lambda \qquad (3.6)$$

As shown in Figure 3.9, when an incident X-rays hit the lattice plane (*hkl*) with an angle of θ, they are elastically scattered by atomic orbital electrons and the angle between the diffracted X-rays and the lattice plane is still θ. Clearly, the lower ray travels farther by the distance BC+CD, which is actually equal to 2d*sin θ. Constructive interference only occurs when Bragg's law is fulfilled, that is, the two diffracted X-rays remain in phase and as a result the summed amplitude reaches maximum. Since the wavelength of X-rays is a constant, the d-spacing of the lattice plane determines the position of the diffraction peak, while the peak density is determined by the electron density of the lattice plane. Therefore, for crystalline substance, a series of diffraction peaks will be obtained after the X-ray irradiation, corresponding to different lattice planes. The XRD pattern is like the fingerprint of the crystal and can be used for phase identification and unit cell parameter determination.

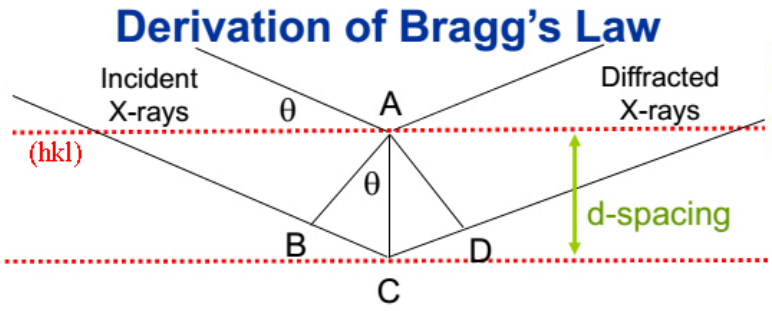

Figure 3.9 Bragg diffraction of X-rays.

3.2.2 X-Ray photoelectron spectroscopy

As shown in Figure 3.8, the X-rays have relatively higher energy due to their high frequencies, usually much higher than that of chemical binding.

$$E = h\nu \qquad (3.7)$$

As a result, core electrons (1s, 2s, 2p, 3s, 3p, 3d) can be ejected out of the sample surface by X-rays due to photoelectric effect.

The principle of X-Ray photoelectron spectroscopy (XPS) is shown in Figure 3.10. When an X-ray beam directs to the sample surface, the energy of the X-ray is absorbed by the core electrons of the atoms. The excited electrons thus possess enough energy to get rid of the binding of the nuclei and emit out of the sample surface. This free electron is referred to as photoelectrons. The energies of the photoelectrons is determined by

$$E_k = h\nu - E_b - \phi \qquad (3.8)$$

Where E_k is the kinetic energies of the ejected photoelectrons, which can be measured by the energy analyzer; $h\nu$ is the energy of the X-ray; E_b is binding energies of core electrons; ϕ is an instrument dependent constant. Since core electrons are spatially close to the nucleus, their corresponding binding energies are characteristic of the types and chemical states of nucleus (elements).

$$E_b = h\nu - E_k - \phi \qquad (3.9)$$

It should be noted that, the penetration depth of X-ray is up to micrometers. However, only the surface photoelectrons (< 10 nm) can escape from the sample surface. Therefore, XPS is a surface sensitive technique used to determine the chemical compositions of surfaces and bonding states of elements.

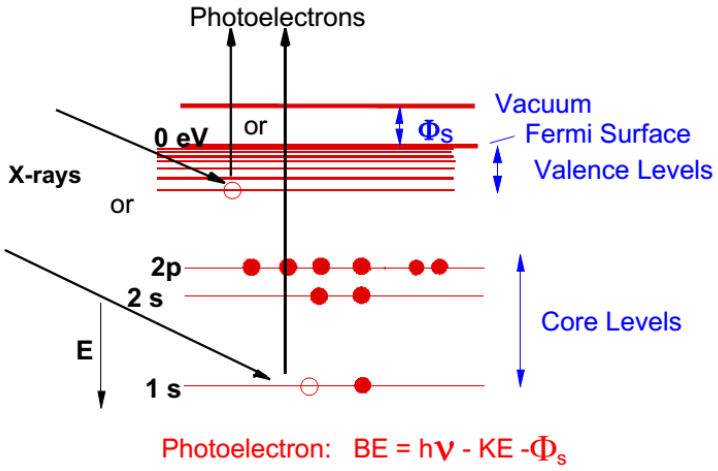

Figure 3.10 The basic principle of XPS, which is based on the photoelectric effect.

3.2.3 Fourier transform infrared spectroscopy

The Fourier transform infrared spectroscopy (FTIR) is concerned with the study of infrared absorption, which causes vibrational transition of a molecule. Therefore, it is also known as the vibrational spectroscopy. The term "Fourier Transform" shows the method used for signal analyzing.

Atoms within a molecule are always linked by chemical bonds, thus forming various functional groups. These functional groups are not motionless; instead they vibrate, stretching and bending for example, naturally around their equilibrium positions with certain frequencies. When energy is applied in the form of infrared radiation, it may be absorbed when 1) frequencies of the applied infrared are equal to the natural frequencies of functional groups and 2) the natural vibrations cause changes in dipole moments of the molecules, leading to transition of the molecular vibrational energy levels. Since each functional group has its own characteristic frequency, they will show different absorption peaks after the Fourier transformation. Therefore, the FTIR spectra can be used in structure elucidation to identify the presence of certain functional groups.

3.2.4 Ultraviolet-visible spectroscopy

The Ultraviolet-visible spectroscopy **(**UV-Vis) is also known as the electron absorption spectroscopy. That is, it studies the transition of electronic energy levels. Similar to vibration, the electrons of a molecule also exist in a number of defined energy levels. A change in electronic energy level requires the absorption of certain energy, which should match with the energy difference between the two levels. Since the electronic energy levels of a molecule are more widely separated than those of vibration, only radiations with higher energy can excite the transition. Ultraviolet and visible lights just fall into this range. Usually, organic molecules contain binding σ and π electrons and non-bonding n electrons. Therefore, four types of electronic transitions are involved in the UV-Vis, σ-σ^*, n-σ^*, n-π^* and π-π^*. (* indicates the corresponding anti-bonding orbit.)

3.2.5 Scanning electron microscope

The Scanning electron microscope (SEM) is an instrument in which the specimen surface is scanned by a focused beam of electrons across a rectangular shaped area (called "Raster"). The signals generated from electron-sample interaction forms image on the

screen. The reason why electrons are chosen is because 1) they can be easily generated from variety of materials; 2) they are charged particles therefore can be accelerated to high speed and moved around by magnetic fields. When electrons hit the surface of sample, they undergo elastic and inelastic collisions or are backscattered out of the sample, as shown in Figure 3.11. Among these signals, the secondary electrons, backscattered electrons and characteristic X-rays are the most frequently collected signals.

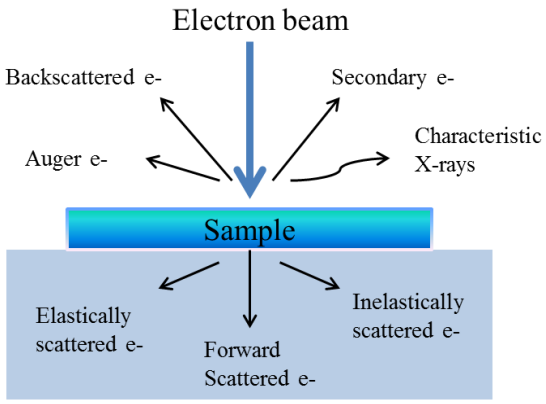

Figure 3.11 Various signals generated from the specimen-electron interaction.

Secondary electrons are produced through inelastic scattering that results in the ejection of loosely bound electrons out of the specimen. The secondary electrons are emitted from the top 1-50nm zone of the excitation area. That makes them very sensitive to topography. Backscattered electrons are produced through elastic scattering that results in the primary electron being re-emitted out of the specimen. The number of backscattered electrons increases with atomic number. As a result, contrast observed is proportional to atomic number, allowing the distinguishing of compositionally different regions. X-rays are also produced by inelastic scattering of beam electrons. X-rays are produced by two different electron beam-matter interactions. Continuous radiation is emitted when fast electrons are rapidly slowed down when passing through the electric field around atomic nuclei. It is non-specific and contributes to the background. Characteristic X-ray, however, is emitted from atoms when electrons make discrete transitions to lower atomic energy orbitals. When an incident electron beam hits atoms of the sample, the orbital electrons at the ground state may be excited and ejected, leaving holes in the electron shells. If these "holes" are in the inner shells, the atoms are not stable. Electrons from outer, high energy

shells will jump to the inner shells to stabilize the atoms. The energy lose is released in the form of X-rays. The K alpha and K beta X-rays are the most common signals observed, which come from the transition of electrons from L to K shell (innermost shell) and M to K shell respectively. Therefore, the X-rays emitted are characteristic of the type of elements and the two electron shells involved that allow the identification of elemental compositions of the sample.

3.2.6 Transmission electron microscopy

When the electrons are accelerated to very high speed, they behave like waves (wave-particle duality) and can pass through thin samples. The transmitted electrons get scattered due to the electron-matter interaction, as shown in Figure 3.11. Transmission Electron Microscopy (TEM) is a method of producing 'images' by illuminating the sample with electrons and detecting the elastically scattered electrons that are transmitted through it.

Essentially, TEM operates on the same principle as the light microscope except using electrons instead of light. The minimum resolvable distance (d) is proportional to the wavelength (λ) of energy source used.

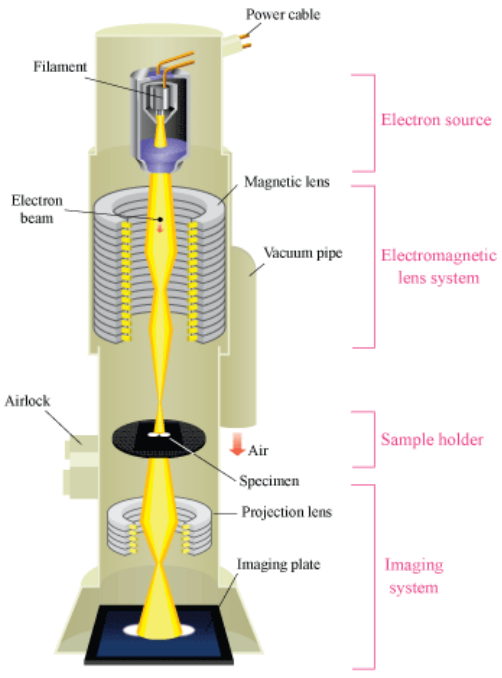

Figure 3.12 Schematic outline of TEM.

$$d = 0.61\lambda / NA \qquad (3.10)$$

The wavelength of an electron is depending on the accelerating voltage.

$$\lambda = h / \sqrt{2meV} \qquad (3.11)$$

As a result, high resolution up to <2 Å can be provided by TEM.

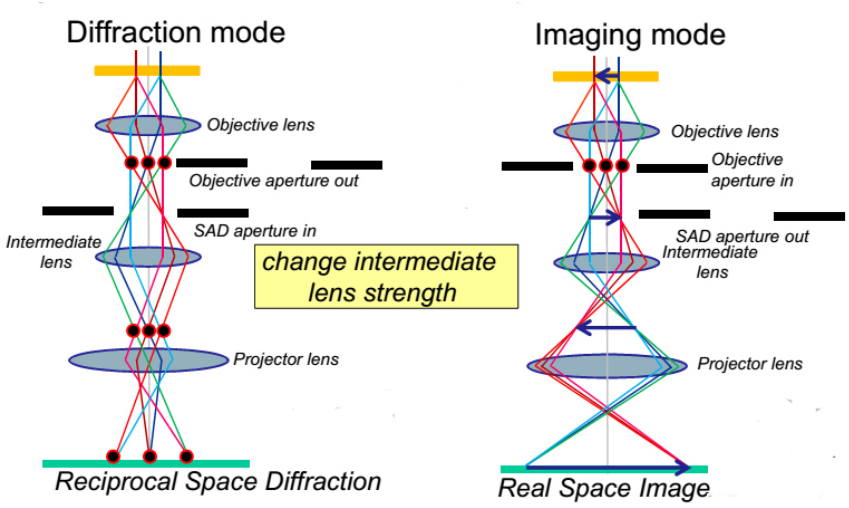

Figure 3.13 The beam paths in the imaging mode and diffraction mode of TEM.

The schematic outline of a TEM is shown in Figure 3.12. It includes four parts: electron source, electromagnetic lens system, sample holder, and imaging system. Electron source produces and accelerates the electrons, which are then tightly focused by electromagnetic lenses. Only those electrons with well-defined energy are allowed to pass through. After interacting with the specimen, the scattered electrons are refocused, enlarged and finally projected onto the screen. There are two different modes in TEM, imaging mode and diffraction mode, depending on the strength of the intermediate lens, as shown in Figure 3.13. In the imaging mode, high angle electrons are blocked by the objective aperture to increase contrast. All the electrons elastically scattered from one point of the sample are focused by the objective lens into one point on the first image plane. This “image” then passes down the column through the intermediate and projector lenses, showing a direct microstructure of the sample. In the diffraction mode, the selected area aperture is in to restrict the electrons passed. Parallel electrons elastically scattered from different points of the sample are focused into one point. This is the back focal plane of the objective lens and is where the diffraction pattern is formed. The objective lens is the most critical part of a TEM. Its resolution limit defines the resolution of the whole microscope.

3.3 Material Synthesis

3.3.1 Lignin-assistant aqueous exfoliation of MoS_2

A desired amount of AL (25, 125, 250, 375 or 500 mg) was added to 250 mL Millipore water in a glass bottle. When AL was completely dissolved, 2.5 g bulk MoS_2 was added into the AL solution. The mixture was then sonicated in a low-power sonic bath (MRC product: DC200H, 200W) for 5 to 80 h. The resulting dispersions were left to stand for approximately 24 h to allow large unstable MoS_2 aggregates to form and then centrifuged for 15 min at 1500 rpm to remove unexfoliated MoS_2. After centrifugation, the top 40 mL (out of 50-mL centrifuge tube) was carefully removed by pipet and retained for further use. The above AL-MoS_2 dispersion was vacuum-filtered onto a nitrocellulose membrane (Millipore, 0.025 μm pore size, 47 mm diameter) and washed with excess Millipore water. The obtained solids were re-dispersed in a small amount of water by bath sonication for 2 h. The undispersed fraction was removed by centrifugation at 1500 rpm for 15 min to give the saturated AL-MoS_2 dispersion without free AL.

To determine the concentration of the MoS_2 dispersion, a precisely measured 50 mL of AL-MoS_2 dispersion was filtered under high vacuum onto a pre-weighed nitrocellulose membrane (Millipore, 0.025 μm pore size, 47 mm diameter). After washing with excess Millipore water, the membrane was dried in a vacuum oven at 40 ℃ for 24 h and reweighed to give the deposited mass. Because it's impossible to thoroughly wash out the adsorbed AL, the content of MoS_2 mass on the filter membrane was determined by thermal gravimetric analysis (TGA).

The saturated AL-MoS_2 dispersion without free AL was immersed in liquid nitrogen, followed by freeze-drying. The obtained MoS_2 powder was annealed at 700 ℃ for 2h in an argon atmosphere.

3.3.2 Preparation of MoS_2/C hybrid nanofibers

The MoS_2 was synthesized using hydrothermal method. Typically, 250 mg Na_2MoO_4 and 200 mg thioacetamide (TAA) were dissolved in 60 ml deionized H_2O. The mixture was then transferred to a 100 ml Teflon-lined autoclave and kept at 200 ^oC for 16 hours. After

cooling down, the black precipitates were collected and washed with DI water and ethanol for 3 times. The MoS_2/PAN hybrid nanofibers were then fabricated via conventional single-spinneret electrospinning. Firstly, 150, 300 and 900 mg of MoS_2 was dispersed in 4.4g DMF using ultrasonication (Sonic, VCX 750), respectively. 300 mg PAN was then dissolved into each of the above suspensions through vigorous stirring at 60 ^oC for about 6 hours. The weight ratio of MoS_2 to PAN was 0.5/1, 1/1, 3/1, respectively. The electrospinning of the suspensions was carried out under a working voltage of 9.5~12.5 kV. The flow rate and needle tip-to-plate collector distance were fixed to 0.3 ml/h and 15 cm, respectively. The as-spun nanofibers were heated from room temperature to 280 ^oC at a heating rate of 1 ^oC/min and then stabilized at 280 ^oC for 1 hr in air. After that the nanofibers were further heated to 700 ^oC in argon (flow rate: 100 sccm) at a heating rate of 5 ^oC/min followed by carbonizing at 700 ^oC for 3 hours. For comparison, neat carbon nanofiber mats were also prepared from PAN by electrospinning followed by stabilization and carbonization.

3.3.3 Synthesis of the SL-MoS_2/C composite

The SL-MoS_2/C composite was synthesized using hydrothermal method. Typically, 300 mg Na_2MoO_4, 900 mg DOPA-HCl and 900 mg TAA were dissolved in 20 ml deionized water, respectively, and then transferred to a 100 ml Teflon-lined autoclave. The suspension was kept at 200 ^oC for 16 hours. After cooling down, the black precipitates were collected by centrifugation and washed with DI water and ethanol for 3 times. The obtained sample was annealed at 700 ℃ for 3 hours in argon to eliminate the surface functional groups.

The Fe_3O_4/C and WO_2/C composites were also synthesized following the same approach. 1 mmol $Na_2WO_4.2H_2O$ and $FeCl_3.6H_2O$ were dissolved in 60 ml deionized water and then mixed with 4 mmol DOPA-HCl, respectively. The suspensions were transferred to a 100 ml Teflon-lined autoclave and kept at 160 ^oC for 16 hours directly. The obtained samples were annealed at 400 ℃ for 3 hours in argon.

3.3.4 Fabrication of the NDG/MoS_2 heterostructure

Firstly, the lithium intercalated MoS_2 was synthesized by immersing 1.5g MoS_2 powder in 8 ml 1.6 M butyllithium solution for 3 days. The Li_xMoS_2 obtained was collected by centrifugation and washed with hexane for 3 times. After the exfoliation of Li_xMoS_2 in water (1 mg/ml) under ultrasonication, the mixture was centrifuged at 2000 rpm for 5 min to remove any unexfoliated material. The pH of the suspension was about 11.4. An excess amount of DOPA-HCl aqueous solution was then added into the suspension under stirring. The black flake-like floccules were formed within several minutes. They were isolated by centrifugation and washed with water for 3 times. The black solid was freeze dried and annealed at 600 ℃ for 2 h (the argon flow is about 10 sccm and the system pressure is about 0.1 mbar).

As a control experiment, the pH of the aqueous solution was adjusted to 11.4 by NaOH in the absence of MoS_2, and then DOPA-HCl was added (0.5 mg/ml). After 10 minutes, the solution was centrifuged at 11000 rpm for 10 minutes. No precipitation was found at the bottom of the tube.

Reference:

[1] V. Nicolosi, M. Chhowalla, M. G. Kanatzidis, M. S. Strano and J. N. Coleman. *Science*. **2013**, 340.

[2] R. J. Hunter, *Introduction to Modern Colloid Science*, Oxford University Press, **1993**.

[3] J. N. Israelachvili, *Intermolecular and Surface Forces*, Elsevier Science, **2010**.

[4] M. Rubinstein and R. H. Colby, *Polymer Physics*, OUP Oxford, **2003**.

[5] S. Cavaliere, S. Subianto, I. Savych, D. J. Jones and J. Rozière. *Energy Environ. Sci.* **2011**, 4, 4761-4785.

[6] V. Thavasi, G. Singh and S. Ramakrishna. *Energy Environ. Sci.* **2008**, 1, 205-221.

[7] D. Li and Y. Xia. *Adv. Mater.* **2004**, 16, 1151-1170.

[8] M. Inagaki, Y. Yang and F. Kang. *Adv. Mater.* **2012**, 24, 2547-2566.

[9] M. Nandi, K. Okada, A. Dutta, A. Bhaumik, J. Maruyama, D. Derks and H. Uyama. *Chem. Commun.* **2012**, 48, 10283-10285.

[10] L. I. B. David and A. F. Ismail. *J. Membr. Sci.* **2003**, 213, 285-291.

[11] D. Zhu, C. Xu, N. Nakura and M. Matsuo. *Carbon*. **2002**, 40, 363-373.

[12] K. Byrappa and T. Adschiri. *Prog. Cryst. Growth Charact. Mater.* **2007**, 53, 117-166.

[13] G. M. Whitesides and M. Boncheva. *Proc. Natl. Acad. Sci. U. S. A.* **2002**, 99, 4769-4774.

Chapter 4

Lignin-assisted Exfoliation of MoS_2 in Aqueous Media and Its Application in Lithium Ion Batteries*

In this chapter, for the first time we disclose that alkali lignin, a low-cost, environmentally benign and bio-renewable feedstock, is an excellent surfactant for direct exfoliation of bulk MoS_2 to nanosheets via sonication in water. The stabilization mechanisms and disperse conditions of lignin are explored. When applied as electrode materials for the LIBs, the exfoliated MoS_2 nanosheets exhibit much improved electrochemical performance compared to its bulk counterpart. Not only MoS_2, our results also indicate that alkali lignin is a versatile surfactant for aqueous exfoliation of many other types of layered materials, including graphite, WS_2 and boron BN. Therefore, we believe the findings of this work would facilitate the development of low-cost, environmental friendly and large-scale production of two-dimensional nanomaterials as well as utilization of lignin in high value-added products.

*This chapter published substantially as reference: Liu, W.#; **Zhao, C**.#; Zhou, R.; Zhou, D.; Liu, Z.; Lu, X. Nanoscale 2015, 7, 9919.

4.1 Introduction

As a member of 2D transition metal dichalcogenides, MoS_2 has a layered structure with a plane of Mo atoms covalently sandwiched between two planes of S atoms in a trigonal prismatic arrangement. It exhibits unique electronic, optical and electrochemical properties because of this structural feature, and has great potential for low-power electronics, optoeletronic devices, logic circuits, catalytic and energy storage applications.[1-6] However, just like other 2D materials, the properties of MoS_2 are also thickness dependent. For example, bulk MoS_2 is an n-type semiconductor with an indirect band gap of ~1.2 eV, while single-layer MoS_2 is a direct-band gap semiconductor with a gap of ~1.8 eV.[1,7] Similarly, it has been demonstrated that the electrochemical storage capacity of MoS_2 nanosheets is much higher than that of bulk crystals owing to the larger surface area and more active edges of the former.[8-10] In order to utilize the valuable properties of monolayer or few-layer MoS_2, different exfoliation techniques or synthesis methods have been developed for MoS_2, including micromechanical exfoliation,[11] chemical exfoliation through intercalation,[12,13] liquid-phase exfoliation,[14] thermal ablation method,[15] CVD on substrates[16] and direct solvothermal synthesis,[17] etc. Among these methods, liquid-phase exfoliation is so far the most suitable route for large scale production of MoS_2 nanosheets.[14,18-20] Although monolayer MoS_2 produced by scotch tape, CVD, etc. is ideal for electronics and optoeletronic devices, dispersed monolayer or few-layer MoS_2 produced by liquid-phase exfoliation will be sufficient to meet the requirements of a range of applications such as nanoscale hybrids for use in thermoelectrics, supercapacitors and LIBs.[21]

Liquid-phase exfoliation of MoS_2 in an aqueous media has economic and environmental advantages over the exfoliation in organic solvents.[22] The exfoliation of MoS_2 in water is, however, challenging owing to its hydrophobic nature. One method to address this issue is to use surfactants, which allows the exfoliated sheets to remain suspended. So far a few types of block copolymers,[2] charged macromolecular[21,23] and small organic salts[24] have been used to stabilize exfoliated MoS_2 in water. This, however, requires tedious synthesis procedures, and the surfactants also have limited capability for dispersing MoS_2, giving dispersions with MoS_2 concentrations well below 1.0 mg mL^{-1}.

Lignin, the second most abundant natural polymer after cellulose, accounts for up to 20-30 wt% of wood.[25] The annual production volume of lignin by pulp and paper industry is estimated to be 50 million tons.[26] Currently lignin goes mostly to relatively low-value energy recovery, so utilization of lignin in high-value products is receiving increasing attention. It is well known that the stabilization of surfactant-nanoparticle dispersions usually relies on electrostatic repulsion and/or steric hindrance.[27,28] Alkali lignin (AL), a type of low-cost commercial technical lignin, consists of negatively charged rigid macromolecules and is soluble in water.[29] Therefore, it has great potential to serve as surfactant for exfoliation of MoS_2 in aqueous media. In this work, AL was used as surfactant to prepare MoS_2 nanosheets in water by liquid-phase exfoliation method without any pre-treatment of MoS_2. Herein we report the effective exfoliation of bulk MoS_2 into nanosheets by this facile approach and the excellent stabilizing effects of AL. Under optimized dispersing condition, the obtained aqueous dispersions contain a concentration of MoS_2 as high as 1.75 ± 0.08 mg mL^{-1}. To validate the usefulness of the exfoliated MoS_2 nanosheets, their electrochemical performances are demonstrated as the anode of LIBs. Our results also show that AL can be used as a general surfactant for direct exfoliation of a wide range of layered materials, including graphite, MoS_2, WS_2 and BN in aqueous media.

4.2 Experimental Section

4.2.1 Materials

MoS_2 (99% purity) was purchased from Sigma-Aldrich Chemicals Inc. (USA). Alkali lignin was purchased from TCI America (USA, TCI product number: L0082, softwood lignin) and used without further purification. 1M $LiPF_6$ in a mixture of ethylene carbonate and dimethyl carbonate at a 1:1 volume ratio were purchased from Charslton Technologies Pte Ltd (Singapore).

4.2.2 Synthesis

Seen in section 3.3.1

4.2.3 Characterization

Optical absorption spectra were recorded on a Shimadzu UV-3600 UV–vis–NIR spectrophotometer with optical grade quartz cuvettes. For the MoS_2 dispersions with different lignin concentration, corresponding lignin aqueous solutions were scanned as baseline. All dispersions were diluted to one fifth or one twentieth of original concentrations because with original concentration the measured absorbance values for some samples exceed the measuring range of the equipment. Zeta potential was determined by dynamic light scattering measurement using a Zetasizer Nano ZS (Malvern Instruments Ltd., UK). All the samples were tested at room temperature and PH value of 7.5. TGA was performed on a TA Instruments TGA Q 500 under a nitrogen atmosphere at a heating rate of 10 ℃ min^{-1}. TEM was performed on JEOL-2010 with accelerating voltage of 200 kV. Samples for TEM were prepared by dropping diluted MoS_2 dispersion on carbon-coated Cu grids. SEM observation was investigated by JEOL FESEM 7600F field emission scanning electron microscope. The samples were coated with gold for 60 s. AFM observation was conducted on a Dimension 3100 AFM (Digital Instruments). The MoS_2 dispersion without free AL was used in the AFM tests because residual free AL would disturb the measured thickness. The samples were prepared by spin-coating the diluted MoS_2 dispersion onto freshly cleaved mica. Raman spectra were obtained using a Renishaw Invia Raman microscope with an excitation wavelength at 633 nm. XRD patterns were recorded in a Bruker D8 Advanced XRD using Cu Kα radiation. XPS measurements were performed on a Kratos Analytical AXIS His spectrometer with a monochromatized Al Kα X-ray source (1486.6 eV photons). The samples are tested with the MoS_2 powders obtained by freeze-drying the MoS_2 dispersion without free AL.

The electrochemical performances of the aqueous exfoliated MoS_2 were evaluated with a standard CR2032 coin cell. The working electrodes were composed of 60 wt% MoS_2, 30 wt% carbon black and 10 wt% polyvinylidene fluoride unless otherwise specified. A Celgard® 2600 membrane was used as the separator. Lithium metal foil was used as the counter/reference electrode, and 1 M $LiPF_6$ in a mixture of EC and DMC (1/1 in v/v) as the electrolyte. The CV was studied on a PGSTAT302N Autolab electrochemical workstation with a scan rate of 0.05 mV/s. For comparison purpose, the electrochemical performance of commercial MoS_2 powder (<2 μm) were tested under the same conditions.

4.3 Results and Discussion

4.3.1 Lignin-assisted exfoliation of MoS_2

4.3.1.1 Stabilizing effects of AL on MoS_2

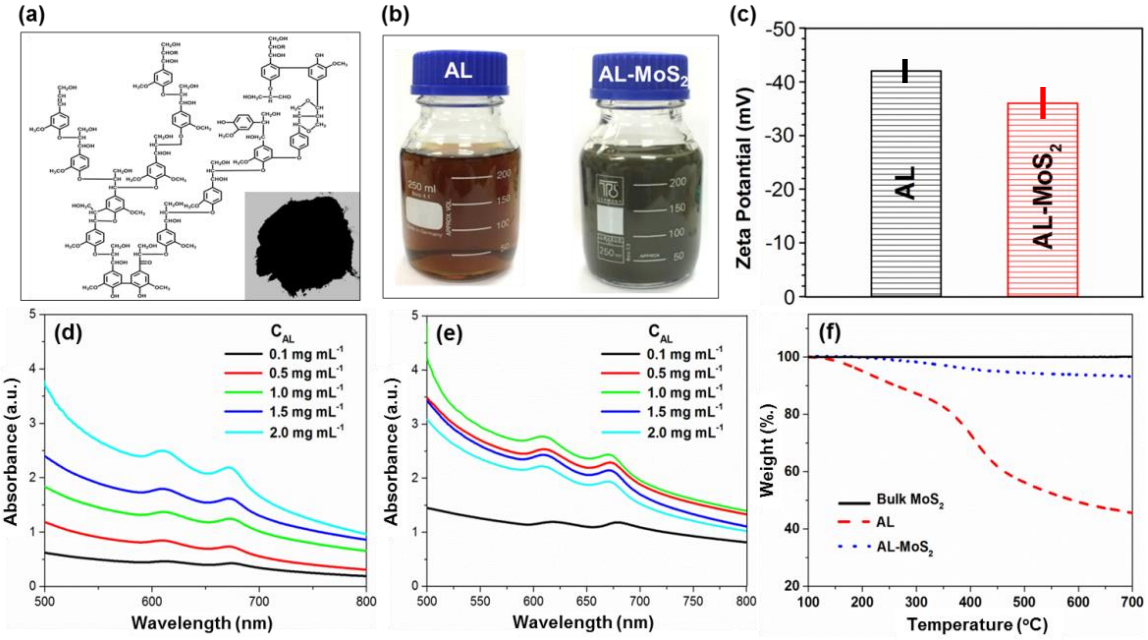

Figure 4.1 (a) Structural model of lignin from ref 24. The inset shows the photograph of AL powder. (b) Photographs of AL and corresponding AL-MoS_2 aqueous dispersions. (c) Zeta potential of AL and AL-MoS_2 dispersion. UV-Visible spectra of AL-MoS_2 aqueous dispersions with different AL feed concentrations. (d) Sonication treatment for 5 h (1/5 of original concentrations). (e) Sonication treatment for 80 h (1/20 of original concentrations). (f) TGA curves of bulk MoS_2, AL and AL-MoS_2 (without free AL) powders.

Lignin has a rigid, hyperbranched macromolecular structure composed of three different types of phenylpropane units and various functional groups such as hydroxyl, methoxy, ether, aldehyde, and ester groups (Figure 4.1a).[25] The inset in Figure 4.1a and 4.1b show the representative photographs of AL powder, AL and AL-MoS_2 aqueous dispersions (AL feed concentration of 0.5 mg mL^{-1}). The dark green AL-MoS_2 dispersion is prepared by sonication (5h) followed by centrifugation (1500 rpm for 15 min). In this process, the AL was absorbed on the exfoliated nanosheets due to van der Waals forces. The dispersion is very stable and only little sedimentation is observed over weeks. To explain

the excellent aqueous stability, zeta potential of the AL and AL-MoS_2 aqueous dispersions was measured. The results (Figure 4.1c) show that the dispersed AL and AL-MoS_2 are both negatively charged, with zeta potential of -42 and -37 mV, respectively. The values well exceed the accepted value for a stable colloid (-25 mV).[28] The high surface charge of AL makes the exfoliated MoS_2 stably suspended in the aqueous dispersion through electrostatic repulsion. In addition, similar to other polymer surfactants, steric hindrance may also play a role in stabilizing exfoliated MoS_2 since AL consists of rigid macromolecules.[2,27]

4.3.1.2 Disperse condition

The effect of dispersion condition on the concentration of exfoliated MoS_2 (C_M) was investigated by UV-Vis spectroscopy. Figure 4.1d and 4.1e show the UV-Vis spectra of diluted AL-MoS_2 aqueous dispersions with different AL feed concentrations and sonication time (feed concentration of bulk MoS_2 was fixed on 10 mg mL^{-1}). The spectra of the diluted AL-MoS_2 aqueous dispersions show two peaks at ca. 630 nm and 670 nm, which are related to the characteristic A1 and B1 direct excitonic transitions of MoS_2 with the energy split from valence band spin-orbital coupling.[2,16] According to the Lambert-Beer law ($A = \alpha C_M l$, where A is the absorbance, α the absorption coefficient, and l the path length), the C_M is proportional to optical absorbance A. It can be clearly seen that the C_M values monotonously increase with the AL feed concentration when the sonication time is 5 h (Figure 4.1d). This result is in accordance with the reported study using copolymer and sodium cholate as surfactants.[2,21] However, when the sonication time extends 80 h (Figure 4.1e), the C_M value no longer show monotonous increase with AL feed concentrations. The C_M values at different AL concentrations become fairly close to each other except the low C_M value obtained at the AL concentration of 0.1 mg mL^{-1}, and the maximum C_M value appears at the AL concentration of 1.0 mg mL^{-1}. The maximum C_M was measured to be 1.75 ± 0.08 mg mL^{-1} according to the method described in the experimental section and TGA results of bulk MoS_2, AL, and AL-MoS_2 powders (Figure 4.1f). This concentration is significantly higher than the reported C_M values obtained by liquid-phase exfoliation in aqueous media without prior treatment of MoS_2, as summarized in Table 4.1.

Table 4.1 Referenced table of exfoliation of MoS_2 in aqueous media.

Surfactant	Exfoliation method	Concentration	Ref
Sodium cholate	Probe sonication for 16 h; Concentration of surfactant: 1.5 mg mL^{-1}; Concentration of bulk MoS_2: 5.0 mg mL^{-1}; Purification: centrifugation at 1500 rpm for 90 min.	~ 0.5 mg mL^{-1}	21
Chitosan	Gridding bulk MoS_2 followed by oleum treatment; Bath sonication for 40 min followed by probe sonication for 2h; Concentration of surfactant: ~ 0.17 mg mL^{-1}; Purification: centrifugation at 2000 rpm.	~ 1.0 mg mL^{-1}	23
Block polymer PEO−PPO−PEO	Sonication (100 W) for 17 h; Purification: centrifugation at 1500 rpm for 5 min.	140 ppm	2
Sodium dodecyl sulfate	Ball milling for 12 h followed by sonication (80W) for 2 h; Concentration of surfactant: 0.5 mg mL^{-1}; Purification: centrifugation at 5000 rpm for 20 min.	0.8 mg mL^{-1}	24
No surfactant	Sonication in ethanol/water mixture for 8 h Purification: centrifugation at 3000 rpm for 20 min	0.018 mg mL^{-1}	22

4.2.1.3 Evidence of exfoliation

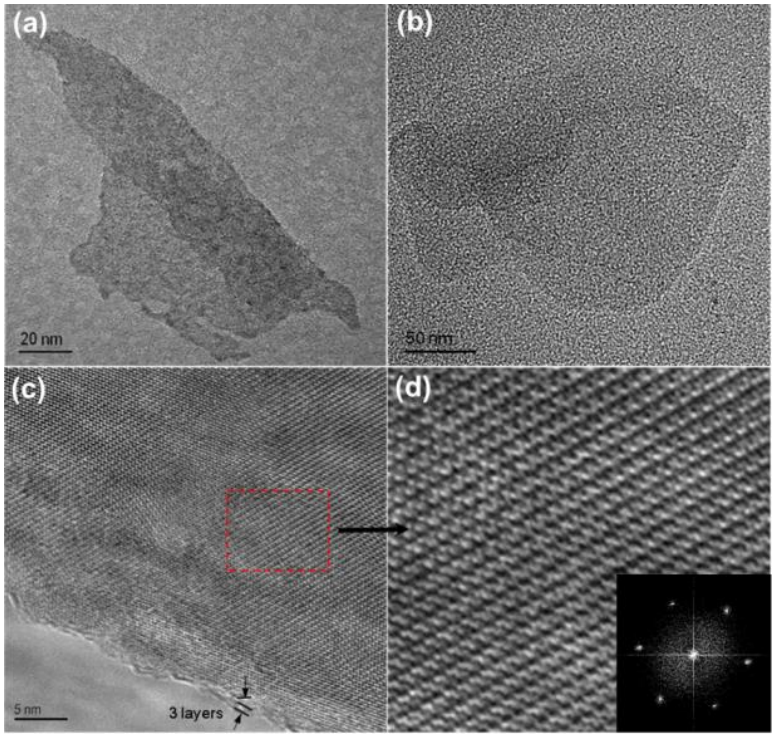

Figure 4.2 (a, b) Typical TEM images of exfoliated MoS_2 nanosheets. (c, d) High-resolution TEM image of a few-layered MoS_2 nanosheet. The inset in (d) is the corresponding SAED pattern.

The TEM studies were conducted to investigate the dispersion state of exfoliated MoS_2. The sample with AL feed concentration of 1.0 mg mL^{-1} and 80 h sonication treatment was chosen for the structure characterization. Figure 4.2a and 2b show TEM images of typical MoS_2 nanosheets with lateral size >100 nm collected from the MoS_2 aqueous dispersion. The MoS_2 nanosheets are slightly transparent to the electron beam and show low contrast with the carbon coating, indicating their ultrathin feature. The high-resolution TEM image in Figure 4.2c shows the edge of a MoS_2 nanosheet, which contains ca. 3 layers. The lattice structure of the MoS_2 nanosheet was not damaged during the exfoliation process (Figure 4.2d). The electron diffraction pattern (inset in Figure 4.2d) reveals that the MoS_2 nanosheet is of high crystalline.

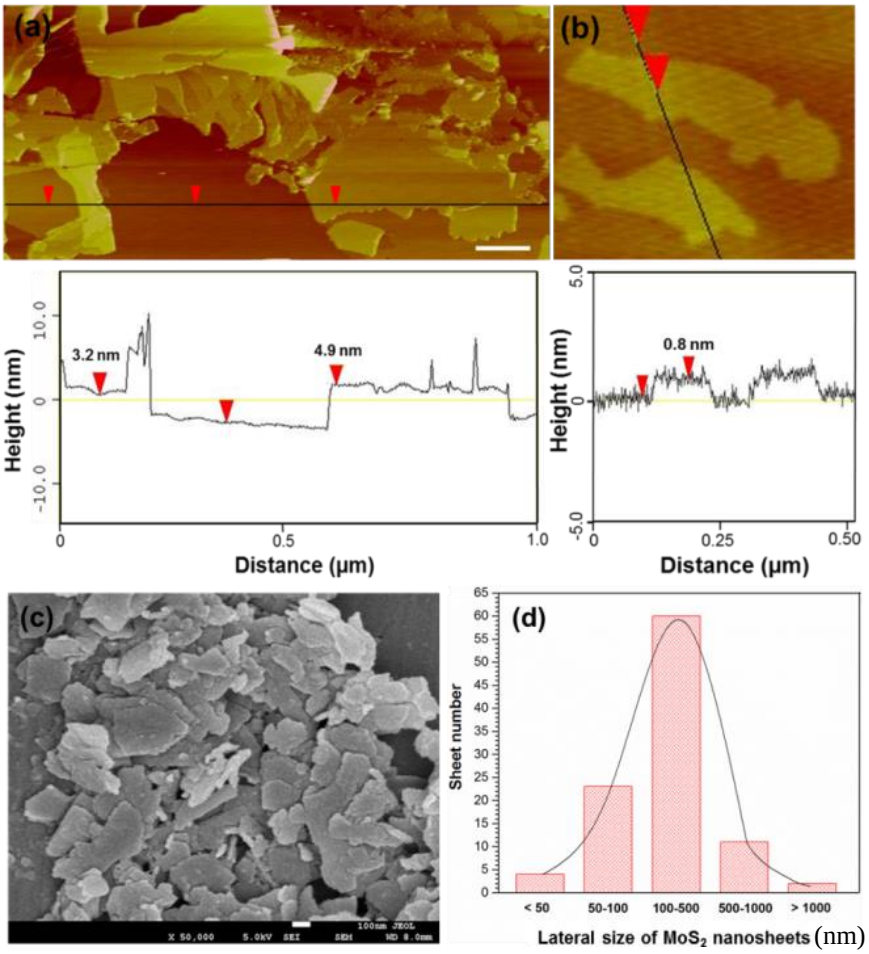

Figure 4.3 AFM images (including corresponding height profiles below) of few-layered (a) and monolayer MoS_2 (b) nanosheets. (c) SEM images of exfoliated MoS_2 powder. (d) The histograms of lateral size distribution of exfoliated MoS_2 nanosheets.

AFM was used to determine the thickness of the exfoliated nanosheets. The results reveal that majority of the exfoliated MoS_2 are multilayer. Figure 4.3a shows two typical MoS_2 nanosheets with thickness of 3.2 and 4.9 nm, respectively, which are estimated to consist of 3-5 atomic layers. Only few monolayer nanosheets are observed. As shown in in Figure 4.3b, the thickness of the nanosheet shown is ~ 0.8 nm, which agrees with the typical height of a single-layer MoS_2 (0.6-1.0 nm).[30] The lateral size of the MoS_2 nanosheets can be clearly observed by SEM. Figure 4.3c shows the typical SEM image of the exfoliated MoS_2 powder obtained by freeze-drying MoS_2 aqueous dispersion without free AL. By analyzing a large number of TEM and SEM images, we generated statistical data on the lateral size of the MoS_2 in the aqueous dispersions (Figure 4.3d). As can be seen, about 60 % of MoS_2 nanosheets have lateral size between 100-500 nm.

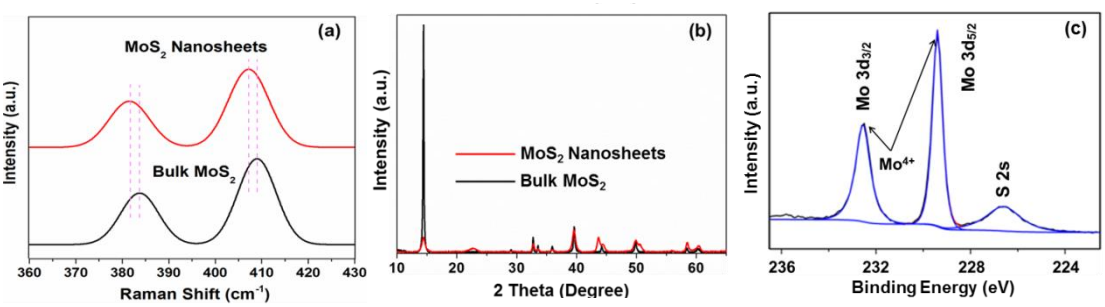

Figure 4.4 (a) Raman spectra and (b) XRD patterns of bulk MoS_2 and exfoliated MoS_2 nanosheets. (c) Mo 3d XPS spectrum of the exfoliated MoS_2 nanosheets after annealing.

The Raman spectra of both bulk MoS_2 powder and exfoliated MoS_2 nanosheets are shown in Figure 4.4a. Both spectra show the well-known high energy mode A_{1g} (stretching of the sulfur atoms) and lower energy E_{2g} (in-plane bending) peaks.[2] The E_{2g} and A_{1g} peaks show downshifts from 383 and 409 cm^{-1} for the bulk MoS_2 to 381 and 407 cm^{-1} for the exfoliated MoS_2, which is in agreement with the reported results.[17,31] The XRD patterns of the bulk and exfoliated MoS_2 are shown in Figure 4.4b. All the diffraction peaks are consistent with the hexagonal 2H-MoS_2 (JCPDS: 65-1951), except a much reduced peak density of (002) reflection for the exfoliated MoS_2, indicating the successful exfoliation

of MoS_2. Finally, XPS spectrum of the exfoliated MoS_2 nanosheets (Figure 4.4c) shows two Mo 3d peaks which can be assigned to Mo^{4+} $3d_{5/2}$ (229.4 eV) and Mo^{4+} $3d_{3/2}$ (232.5 eV). Almost no trace of Mo^{6+} $3d_{5/2}$ peak (~236 eV) was observed, indicating oxidation didn't occur during the treatment.

4.3.2 Exfoliated MoS_2 nanosheets as LIB electrode materials

Graphene-like MoS_2 has been explored as lithium-ion host materials because its high reversible capacity and rate capability, whereas these monolayer and multilayer MoS_2 nanosheets were mainly synthesized by bottom-up approaches, such as hydrothermal, pyrolysis and CVD.[32-34] The facile aqueous exfoliation method described above has the potential for large scale preparation of MoS_2 nanosheets from low-cost MoS_2 mineral. Different from the aforementioned methods, this top-down method preserves the pristine structure of MoS_2. However, the electrochemical behaviors of pristine MoS_2 nanosheets have not been studied so far, to the best of our knowledge. Thus in this work, the exfoliated MoS_2 nanosheets were studied as lithium-ion host materials in LIBs.

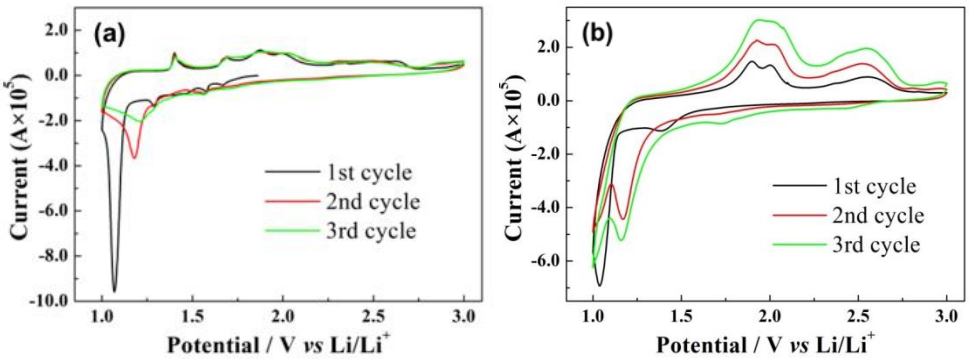

Figure 4.5 Cyclic voltammograms of (a) exfoliated MoS_2 nanosheets and (b) bulk MoS_2 between 1 and 3 V at a scan rate of 0.05 mV/s.

The CV curves of the exfoliated MoS_2 nanosheet are shown in Figure 4.5a. In the first cycle, the sharp cathodic peak at 1.07 V is attributed to the insertion of Li^+ into the MoS_2 layer, accompanied by a phase change from 2H to 1T with Li^+ occupying the interlayer S−S tetrahedron site.[35] While the anodic doublet at around 2 V is assigned to the extraction of Li^+ from the lattice of 1T-MoS_2.[36] Therefore, the Li^+ insertion is highly reversible in this range. It is interesting that two small cathodic peaks at 1.58 and 1.29 V

are also observed, indicating a stepwise transition may occur due to the presence of ultra-thin nanosheets.[37,38] Their corresponding anodic peaks are found at 1.69 V and 1.40 V, with a ΔV of 0.18 V. These peaks are absent for the pristine MoS_2 sample (Figure 4.5b).

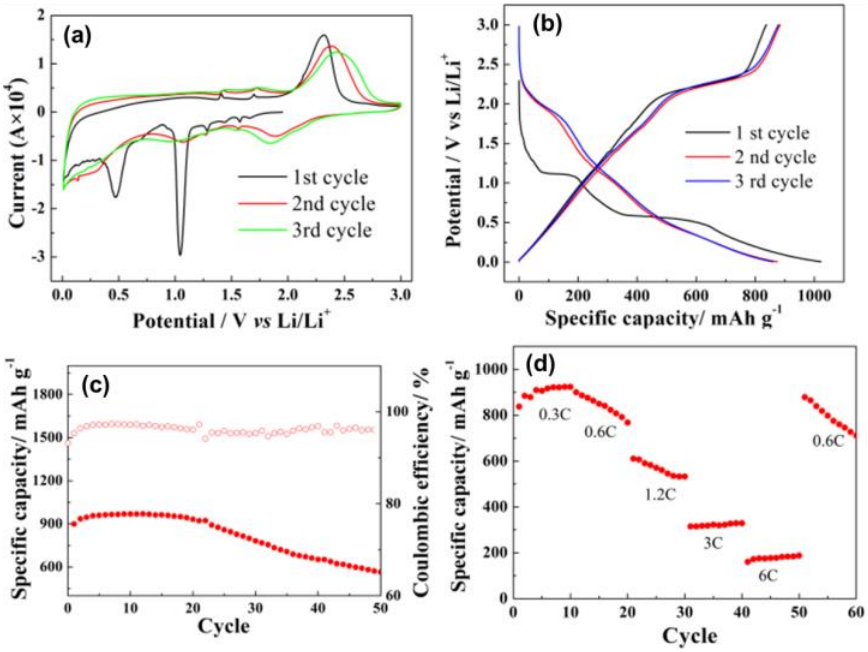

Figure 4.6 (a) Cyclic voltammograms, (b) discharge−charge profiles at 0.3C, (c) cycling performance at 0.6C and (d) rate capabilities of the exfoliated MoS_2 nanosheets between 0.01-3V.

A significant change in lithiation mechanism will occur when the MoS_2 cell is further discharged,[39,40] as shown in Figure 4.6a. Below 1 V, the broad shoulder peak at around 0.69V corresponds to the insertion of additional Li^+ into the ultrathin MoS_2 nanosheets.[40] The distinct peak at 0.47 V is derived from the conversion reaction from 1T-MoS_2 to Mo/Li_2S. In the anodic scan, the intensive peak at 2.32 V is associated with the oxidation of Li_2S to S. It is worth noting that, the 1.58/1.70 V and 1.29/1.41 V redox couples are again observed and their intensities decrease with cycling, indicating the conversion reaction between MoS_2 and Li_2S/Mo is partially reversible.[41-43] In the second discharge, the cathodic peak at 1.90 V is attributed to the lithiation of S. The weak peaks at 1.07 V and 0.35 V can be assigned to the lithiation of the re-formed MoS_2 followed by decomposition of the lithiated MoS_2. The electrochemical performances of the exfoliated MoS_2 nanosheet as an anode are shown in Figure 4.6b-d. The initial charge and discharge capacities are 838 and 1022 mAh/g, respectively, with a CE of 82%. This higher CE is

ascribed to the fast ion/electron transport of the ultrathin MoS_2 nanosheets.[44-46] The reversible capacity increases gradually in the beginning until the 12th cycle (970 mAh/g) and maintains above 600 mAh/g at the 50th cycle. The capacity decline can be ascribed to the dissolution of polysulfide intermediates into the electrolyte during cycling. The exfoliated MoS_2 nanosheets deliver reversible capacities of 920, 800, 550, 330 and 190 mAh/g at 0.3C, 0.6C, 1.2C, 3C and 6C respectively. The reversible capacity restores to ca. 750 mAh/g when the current density is reset to 0.6C.

4.3.3 AL-assisted exfoliation of other types of layered materials in water

Other than MoS_2, AL also shows strong stabilizing effects in exfoliating other layered crystals in water. Herein we also demonstrate that AL can effectively assist the exfoliation of graphene, WS_2 and BN in water and stabilize the exfoliated nanosheets (Figure 4.7). The low cost, non-toxicity and superior surfactant performance of AL make it an ideal candidate for the mass production of 2D nano-materials. More details about AL-assisted exfoliation of graphene, WS_2, BN and other layered materials as well as their applications will be reported later.

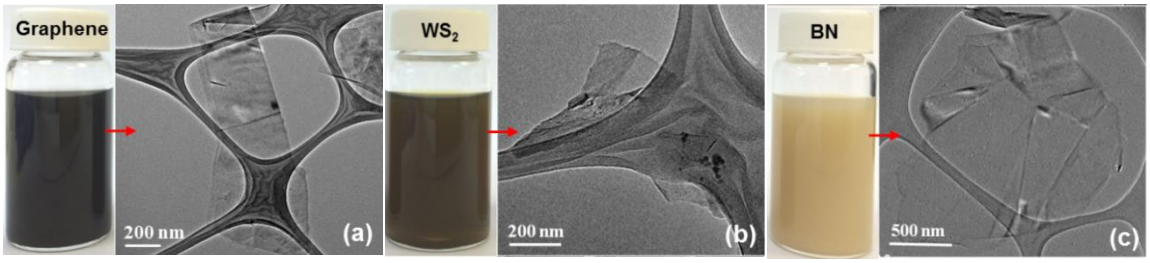

Figure 4.7 Photographs of aqueous dispersions and representative TEM images of the exfoliated nanosheets. (a) AL-graphene, (b) AL-WS_2 and (c) AL-BN aqueous dispersions were prepared by ultrasonic treatment for 5 h and centrifugation at 2000 rpm for 1 h. The concentration of AL was 0.5 mg mL^{-1}. The feed contents of bulk WS_2 and BN were 5 mg mL^{-1}.

4.3 Conclusions

AL has been successfully used as surfactant to produce MoS_2 nanosheets in aqueous media by liquid-phase exfoliation method. It exhibits excellent stabilizing function for the exfoliated MoS_2 nanosheets. With optimized dispersion parameters, the MoS_2 concentration of the resulting dispersion can reach 1.75 ± 0.08 mg mL^{-1}. The stabilization

mechanism lies in the electrostatic repulsion between negative charged AL as well as the steric hinerance of AL macromolecule. Microscopy study shows that the majority of the exfoliated MoS_2 nanosheets have only few layers with lateral size of 100-500 nm. When the exfoliated MoS_2 nanosheets are used as an anode, the LIB cells show relatively good capacity retention. Finally, it is demonstrated that AL has great potential to be a versatile surfactant for exfoliation of other types of layered materials, including graphite, WS_2 and BN. It shows that lignin is an extremely versatile surfactant and may have great potentials for high value-added products in many fields.

References:

[1] RadisavljevicB, RadenovicA, BrivioJ, GiacomettiV and KisA. *Nat. Nanotechnol.* **2011**, 6, 147-150.

[2] M. D. J. Quinn, N. H. Ho and S. M. Notley. *ACS Appl. Mater. Interfaces*. **2013**, 5, 12751-12756.

[3] J. Zhang, S. Najmaei, H. Lin and J. Lou. *Nanoscale*. **2014**, 6, 5279-5283.

[4] M. Bernardi, M. Palummo and J. C. Grossman. *Nano letters*. **2013**, 13, 3664-3670.

[5] B. Radisavljevic, M. B. Whitwick and A. Kis. *ACS nano*. **2011**, 5, 9934-9938.

[6] L. Zhang, H. B. Wu, Y. Yan, X. Wang and X. W. Lou. *Energy Environ. Sci.* **2014**, 7, 3302-3306.

[7] K. F. Mak, C. Lee, J. Hone, J. Shan and T. F. Heinz. *Phys. Rev. Lett.* **2010**, 105, 136805.

[8] L. Cao, S. Yang, W. Gao, Z. Liu, Y. Gong, L. Ma, G. Shi, S. Lei, Y. Zhang and S. Zhang. *Small*. **2013**, 9, 2905-2910.

[9] A. Winchester, S. Ghosh, S. Feng, A. L. Elias, T. Mallouk, M. Terrones and S. Talapatra. *ACS Appl. Mater. Interfaces*. **2014**, 6, 2125-2130.

[10] K. Chang and W. Chen. *ACS Nano*. **2011**, 5, 4720-4728.

[11] A. Splendiani, L. Sun, Y. Zhang, T. Li, J. Kim, C.-Y. Chim, G. Galli and F. Wang. *Nano Lett.* **2010**, 10, 1271-1275.

[12] S. S. Chou, B. Kaehr, J. Kim, B. M. Foley, M. De, P. E. Hopkins, J. Huang, C. J. Brinker and V. P. Dravid. *Angew. Chem., Int. Ed.* **2013**, 52, 4160-4164.

[13] J. Zheng, H. Zhang, S. Dong, Y. Liu, C. Tai Nai, H. Suk Shin, H. Young Jeong, B. Liu and K. Ping Loh. *Nat. Commun.* **2014**, 5, 2995.

[14] V. Nicolosi, M. Chhowalla, M. G. Kanatzidis, M. S. Strano and J. N. Coleman. *Science*. **2013**, 340.

[15] A. Castellanos-Gomez, M. Barkelid, A. M. Goossens, V. E. Calado, H. S. J. van der Zant and G. A. Steele. *Nano Lett.* **2012**, 12, 3187-3192.

[16] J. Jeon, S. K. Jang, S. M. Jeon, G. Yoo, Y. H. Jang, J.-H. Park and S. Lee. *Nanoscale*. **2015**, 7, 1688-1695.

[17] H. S. S. Ramakrishna Matte, A. Gomathi, A. K. Manna, D. J. Late, R. Datta, S. K. Pati and C. N. R. Rao. *Angew. Chem., Int. Ed.* **2010**, 49, 4059-4062.

[18] A. O'Neill, U. Khan and J. N. Coleman. *Chem. Mater.* **2012**, 24, 2414-2421.

[19] J. Z. Wang, L. Lu, M. Lotya, J. N. Coleman, S. L. Chou, H. K. Liu, A. I. Minett and J. Chen. *Adv. Energy Mater.* **2013**, 3, 798-805.

[20] Y. Yao, L. Tolentino, Z. Yang, X. Song, W. Zhang, Y. Chen and C.-p. Wong. *Adv. Funct. Mater.* **2013**, 23, 3577-3583.

[21] R. J. Smith, P. J. King, M. Lotya, C. Wirtz, U. Khan, S. De, A. O'Neill, G. S. Duesberg, J. C. Grunlan and G. Moriarty. *Adv. Mater.* **2011**, 23, 3944-3948.

[22] K.-G. Zhou, N.-N. Mao, H.-X. Wang, Y. Peng and H.-L. Zhang. *Angew. Chem., Int. Ed.* **2011**, 50, 10839-10842.

[23] W. Yin, L. Yan, J. Yu, G. Tian, L. Zhou, X. Zheng, X. Zhang, Y. Yong, J. Li, Z. Gu and Y. Zhao. *ACS nano*. **2014**, 8, 6922-6933.

[24] Y. Yao, Z. Lin, Z. Li, X. Song, K.-S. Moon and C.-p. Wong. *J. Mater. Chem.* **2012**, 22, 13494-13499.

[25] F. G. Calvo-Flores and J. A. Dobado. *ChemSusChem*. **2010**, 3, 1227-1235.

[26] T. Saito, J. H. Perkins, F. Vautard, H. M. Meyer, J. M. Messman, B. Tolnai and A. K. Naskar. *ChemSusChem*. **2014**, 7, 221-228.

[27] P. May, U. Khan, J. M. Hughes and J. N. Coleman. *J. Phys. Chem. C*. **2012**, 116, 11393-11400.

[28] M. Lotya, Y. Hernandez, P. J. King, R. J. Smith, V. Nicolosi, L. S. Karlsson, F. M. Blighe, S. De, Z. Wang, I. T. McGovern, G. S. Duesberg and J. N. Coleman. *J. Am. Chem. Soc.* **2009**, 131, 3611-3620.

[29] G. Wang and H. Chen. *Sep. Purif. Technol.* **2013**, 105, 98-105.

[30] Z. Zeng, Z. Yin, X. Huang, H. Li, Q. He, G. Lu, F. Boey and H. Zhang. *Angew. Chem., Int. Ed.* **2011**, 50, 11093-11097.

[31] N. Liu, P. Kim, J. H. Kim, J. H. Ye, S. Kim and C. J. Lee. *ACS nano*. **2014**, 8, 6902-6910.

[32] C. Zhu, X. Mu, P. A. van Aken, Y. Yu and J. Maier. *Angew. Chem., Int. Ed.* **2014**, 53, 2152-2156.

[33] X. Cao, Y. Shi, W. Shi, X. Rui, Q. Yan, J. Kong and H. Zhang. *Small*. **2013**, 9, 3433-3438.

[34] H. Hwang, H. Kim and J. Cho. *Nano Lett.* **2011**, 11, 4826-4830.

[35] L. Wang, Z. Xu, W. Wang and X. Bai. *J. Am. Chem. Soc.* **2014**, 136, 6693-6697.

[36] X. Fang, C. Hua, X. Guo, Y. Hu, Z. Wang, X. Gao, F. Wu, J. Wang and L. Chen. *Electrochim. Acta*. **2012**, 81, 155-160.

[37] F. Zhou, S. Xin, H.-W. Liang, L.-T. Song and S.-H. Yu. *Angew. Chem., Int. Ed.* **2014**, 53, 11552-11556.

[38] U. K. Sen, P. Johari, S. Basu, C. Nayak and S. Mitra. *Nanoscale*. **2014**, 6, 10243-10254.

[39] X. Fang, X. Guo, Y. Mao, C. Hua, L. Shen, Y. Hu, Z. Wang, F. Wu and L. Chen. *Chem. - Asian J.* **2012**, 7, 1013-1017.

[40] J. Xiao, X. Wang, X.-Q. Yang, S. Xun, G. Liu, P. K. Koech, J. Liu and J. P. Lemmon. *Adv. Funct. Mater.* **2011**, 21, 2840-2846.

[41] J. Wang, J. Liu, D. Chao, J. Yan, J. Lin and Z. X. Shen. *Adv. Mater.* **2014**, 26, 7162-7169.

[42] J. Kong, C. Zhao, Y. Wei, S. L. Phua, Y. Dong and X. Lu. *J. Mater. Chem. A*. **2014**, 2, 15191-15199.

[43] X. Fang, X. Yu, S. Liao, Y. Shi, Y.-S. Hu, Z. Wang, G. D. Stucky and L. Chen. *Microporous Mesoporous Mater.* **2012**, 151, 418-423.

[44] C. Zhao, J. Kong, X. Yao, X. Tang, Y. Dong, S. L. Phua and X. Lu. *ACS Appl. Mater. Interfaces*. **2014**, 6, 6392-6398.

[45] C. Zhao, J. Kong, L. Yang, X. Yao, S. L. Phua and X. Lu. *Chem. Commun.* . **2014**, 50, 9672-9675.

[46] K. Chang and W. Chen. *Chem. Commun.* . **2011**, 47, 4252-4254.

Chapter 5

Thin MoS_2 Nanosheets Encapsulated in Carbon Nanofibers as High-Performance Anodes for Lithium-Ion Batteries*

In the work described in this chapter, highly flexible and free-standing MoS_2-based mat, consisting of disordered graphene-like MoS_2 nanosheets encapsulated in amorphous carbon nanofibers, were fabricated through hydrothermal route followed by electrospinning and annealing for the first time. The high flexibility of the hybrid mat, which is ascribed to the multi-layered MoS_2 nanosheets as well as the resulting thin carbon sections, offers great opportunity for its practical use in various areas. When used as anode in LIBs, the MoS_2/C hybrid nanofibers exhibit excellent cycling and rate stability due to the robust hybrid fibrous structure and effective encapsulation of MoS_2. This work provides a general strategy to prepare high performance MoS_2 electrode, and also a clue to immobilize the soluble polysulfides intermediate in the lithium-sulfur battery.

*This chapter published substantially as reference: **Zhao, C**.; Kong, J.; Yao, X.; Tang, X.; Dong, Y.; Phua, S. L.; Lu, X. ACS Appl. Mater. Interfaces 2014, 6, 6392.

5.1 Introduction

The work presented in Chapter 4 has demonstrated that the exfoliation of MoS_2 indeed is an effective way to improve its Li+ storage capability, both as cathode and anode. However, the electrochemical performance of the exfoliated MoS_2 nanosheets is still not satisfied, especially the cycling stability. This rapid capacity fading can be attribute to the structure destruction induced by volume change in cycling and the dissolution of discharge products, polysulfides, which leads to a loss of active materials. A possible way to solve this problem is to fabricate hybrid nanostructures.[1-4] Chen *et al*. synthesized graphene-like MoS_2/amorphous carbon composites by a hydrothermal route and found that the cycling stability of the composites was greatly enhanced due to the enhanced conductivity and mechanical buffering effect of carbon.[5,6] Lemmon *et al*. prepared MoS_2/PEO composites and the incorporation of PEO stabilized the disordered structure of MoS_2 throughout the cycling regime.[7,8] Another route is to enlarge the interlayer distance of MoS_2, which will not only buffer the mechanical stress during cycling, but also introduce voids and defects into MoS_2 to improve its Li^+ ions storage capacity.[9,10] For instance, Guo *et al*. reported that restacked MoS_2 with enlarged interlayer distance could exhibit superior stability and higher reversible capacity than the raw material.[11] Cho *et al.* reported that disordered MoS_2 nanoplates with an interlayer distance of 0.69 nm could exhibit excellent rate capability even at ultrahigh rate.[12] These research findings indicate that the high performance of MoS_2-based anodes is rooted in the relief of the stress to maintain the structural stability.

Electrospinning, a powerful technique for mass production of nanofibers, is an attractive approach for large-scale fabrication of MoS_2/C hybrid nanofibers. The features of electrospun nanofibers, such as high aspect ratio and large surface area, may render the obtained hybrids good electrochemical properties,[13-17] while the carbon may effectively accommodate the volume change of MoS_2 in cycling. The obtained binder-free self-standing nanofibrous mats can be directly used as an anode after simply punching the mats into suitable size and shape. Furthermore, since thin MoS_2 nanosheets are flexible, similar to that of multilayer graphene, when they are dispersed in carbon nanofibers, excellent flexibility of the structure may be achieved, enabling realization of diverse

flexible LIBs.[18] In this work, we prepared the free-standing MoS_2/carbon nanofibrous mats via electrospinning and carbonization for the first time. The electrochemical properties of the MoS_2/C hybrid mats are reported and correlated to their morphology and structure. The mechanism for the good performance of the MoS_2/C anode is also clarified.

5.2 Experimental Section

5.2.1 Materials

DMF, polyacrylonitrile (PAN, M_w = 150000), thioacetamide (TAA), and sodium molybdate dehydrate (Na_2MoO_4) were purchased from Sigma-Aldrich (USA) and used as received.

5.2.2 Synthesis

Seen in section 3.3.2

5.2.3 Characterization

The morphologies and structure of the hybrid nanofibers were studied by FESEM, TEM and XRD as described section 4.2.3. The compositions of the hybrid nanofibers were determined by TGA (TA Q500). All the samples were heated at a rate of 10 ^oC/ min from room temperature to 600 ^oC in air.

The free-standing MoS_2/C nanofibrous mats and neat carbon mats were used as anode directly. The typical loading of the anodes in the electrode was 1 to 5 mg. The electrochemical tests were performed on a NEWARE BTS-5V10mA battery tester at room temperature. The cells were cycled between 0.005~3.0 V vs Li^+/Li at 50 mA g^{-1} unless otherwise specified. The CV was studied on a PGSTAT302N Autolab electrochemical workstation with a voltage window of 0.005~3.0 V and a scan rate of 0.1 mV/s. The EIS was measured in the frequency range of 10^{-2} to 10^6 Hz with an AC voltage amplitude of 5 mV. For comparison purpose, electrodes were also prepared through casting a slurry of 80 wt% MoS_2 nanosheets or commercial MoS_2 powder, 10 wt% super P carbon black and 10 wt% PVDF in NMP onto a copper foil and investigated.

5.3 Results and Discussion

5.3.1 Structure and morphology of the mats

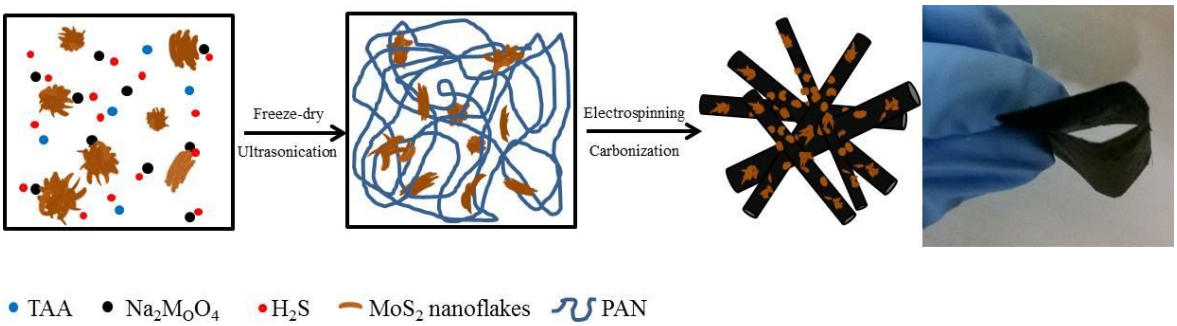

Figure 5.1 Schematics showing the fabrication process for the highly flexible free-standing MoS_2/C nanofibrous mats. The sample in the picture contains 47% MoS_2.

The fabrication process for the MoS_2/C nanofibrous mats is illustrated in Figure 5.1. Thin MoS_2 nanosheets were firstly hydrothermally synthesized from TAA and Na_2MoO_4. TAA, which acts as a sulfurization reagent, decomposes and generates H_2S easily at temperature above 150 ^oC:

$$CH_3CSNH_2 + H_2O \rightarrow CH_3COONH_4 + H_2S \quad (5.1)$$

while Mo (VI) is subsequently reduced in solution by H_2S:

$$Na_2MoO_4 + H_2S \rightarrow MoS_2 + Na_2SO_4 + H_2O + NaOH \quad (5.2)$$

The as-prepared MoS_2 was then encapsulated in PAN nanofibers via electrospinning. After carbonization, highly flexible free-standing MoS_2/C nanofibrous mats were obtained. Electrospinning-derived neat carbon nanofibers are in general fairly brittle,[19] whereas the MoS_2/C hybrid mats are very flexible, as demonstrated in the picture in Figure 5.1. This may be ascribed to the presence of high contents of thin MoS_2 nanosheets in the carbon matrix, resulting in thin carbon sections separated by flexible MoS_2 nanosheets in some regions that may facilitate bending. Indeed the flexibility of the mat increases with the MoS_2 content. The great difference in flexibility between MoS_2/C-95 hybrid mat, which has the highest MoS_2 content among all the hybrid mats, and neat carbon nanofiber mat was demonstrated through repeated bending tests (Figure 5.2).

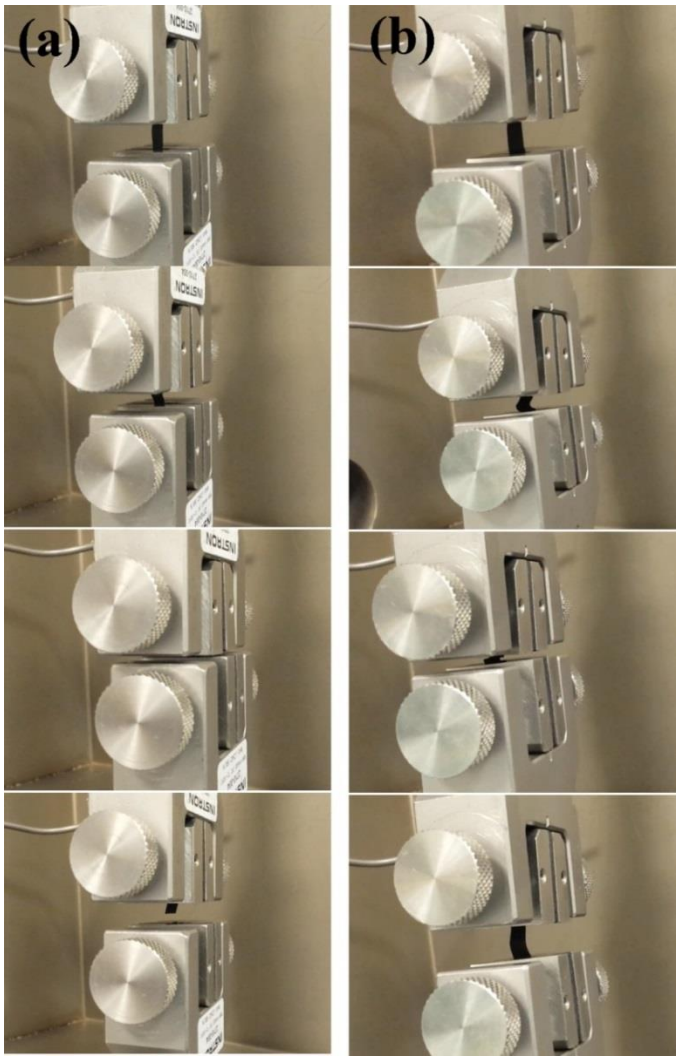

Figure 5.2 Repeated bending tests of (a) the neat carbon mat and (b) MoS_2/C-95 hybrid mat.

To verify the morphologies of the nanosheets and nanofibers, TEM and SEM studies were conducted. Figure 5.3 shows the TEM image of the as-synthesized MoS_2 nanosheets. The nanosheets are loosely packed, forming flower-like geometry with diameter of about 250 nm (Figure 5.3a). A magnified TEM image in Figure 5.3b shows that the petal of the "flower" is comprised of randomly oriented MoS_2 nanosheets with thickness of around 5 nm. This indicates that the number of MoS_2 layers in each nanosheet is less than 10 in most cases. The electron diffraction (SAED) pattern of the MoS_2 nanosheets (Inset of Figure 5.3b) consists of three diffraction rings that can be indexed to (002), (100) and (110) plane of MoS_2. This is further confirmed by XRD results (Figure 5.3c), where three distinct peaks at 2θ = 13.8^o, 33.1^o and 58.5^o corresponding to (002), (100) and (110)

plane of MoS_2, respectively, are observed.[9,20,21] It is worth noting that the (002) diffraction peak of the nanosheets ($2\theta = 13.8^o$; d = 0.64 nm) is at a lower angle than that of the commercial MoS_2 powder ($2\theta = 14.4^o$; d = 0.615 nm), indicating that the interlayer distance of the nanosheets is expanded. It has been reported that with one mole of lithium intercalation, *c* parameter of MoS_2 undergoes an increment of 0.25 Å.[22] The expanded interlayer *d* spacing would relieve the strain caused by electrochemical lithiation/delithiation during cycling and provide more space for Li ion intercalation with reduced diffusion barriers.[11] In addition, the broad (002) peak suggests that the average crystallite size of the nanosheets is around 5 nm. This corresponds to 7-8 MoS_2 layers and is consistent with the TEM result shown above.

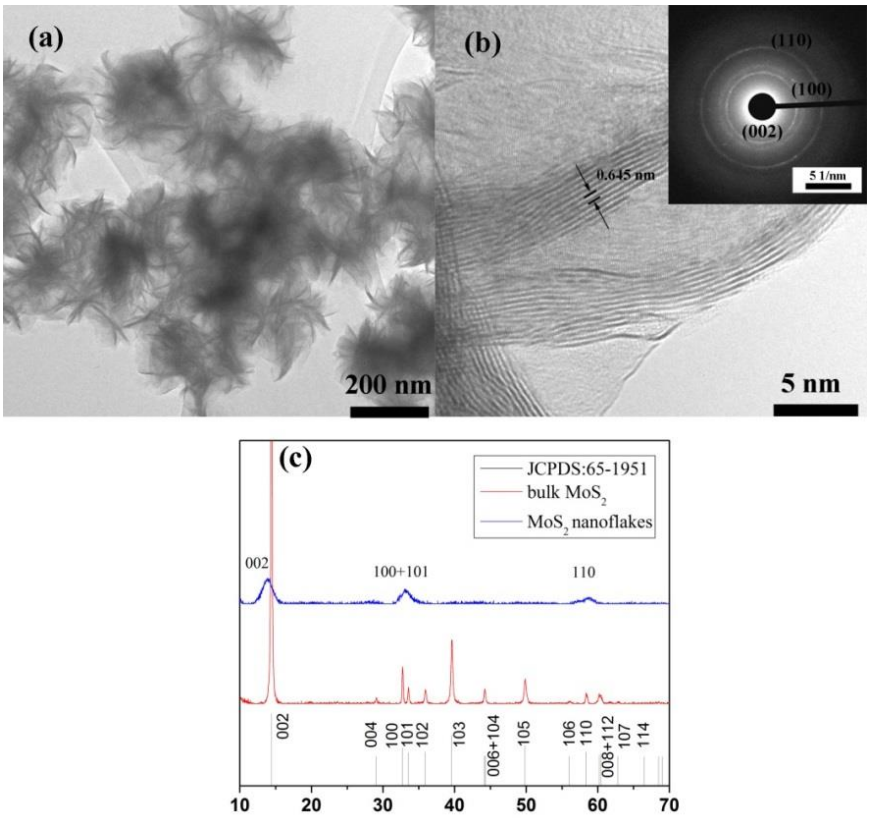

Figure 5.3 (a, b) TEM images and (c) XRD patterns of the hydrothermally synthesized MoS_2 nanosheets; the inset in (b) shows the corresponding SAED pattern.

Electrospinning was used to fabricate MoS_2/PAN hybrid nanofibers. Upon carbonization, PAN is converted to amorphous carbon while MoS_2 nanosheets would remain. This is confirmed by XRD results (Figure 5.4a). Compared with the as-synthesized MoS_2

nanosheets, there is no change in the diffraction peak positions after the electrospinning and carbonization, indicating that the incorporation of PAN and the heat treatment do not affect the microstructure of the MoS_2 nanosheets. The compositions of the MoS_2/C nanofibers were estimated by TGA (Figure 5.4b). There is a large weight loss in the range of 300-500 ℃, which is caused by the combustion of the amorphous carbon and a conversion of MoS_2 to MoO_3 in air. Based on the TGA results, the mass fractions of MoS_2 in the hybrid samples are 47 wt%, 73 wt% and 95 wt%, respectively, for the samples with feed MoS_2/PAN weight ratios of 0.5/1, 1/1 and 3/1. In the following discussion, the three samples are denoted as MoS_2/C-47, MoS_2/C-73 and MoS_2/C-95, respectively, where the numbers indicate the mass fractions of MoS_2 in the hybrids.

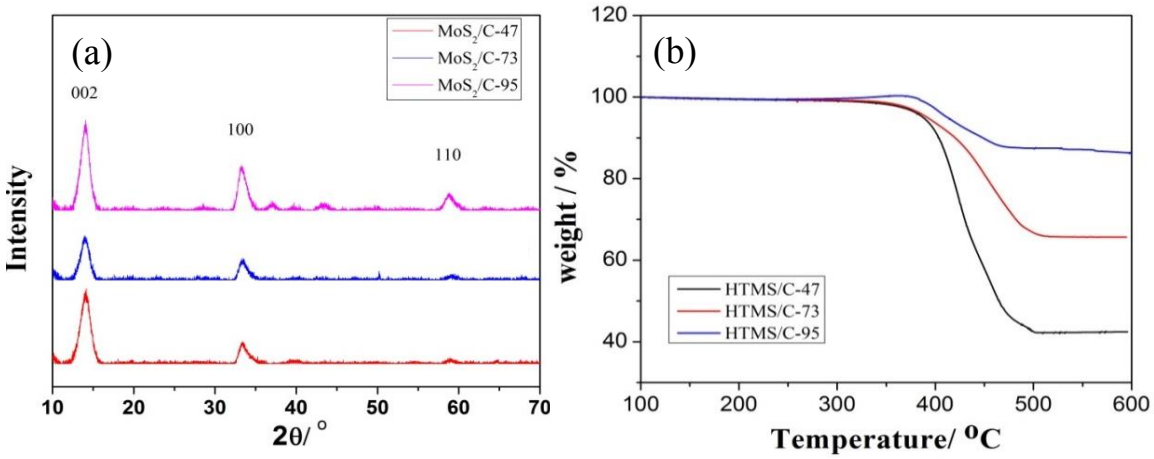

Figure 5.4 (a) XRD patterns and (b) TGA curves of MoS_2/C-47, MoS_2/C-73 and MoS_2/C-95.

SEM images of the as-spun (left) and carbonized (middle) hybrid nanofibers are shown in Figure 5.5. The as-spun nanofibers exhibit "bead-on-string" morphology due to the incorporation of MoS_2 nanosheets. The average diameters of the as-spun nanofibers increase from 250 nm to nearly 1 μm with the increase of MoS_2 content. For the nanofibers with relatively low MoS_2 contents, the diameters are uniform with only some sparsely distributed beads (Figure 5.5a_1 anb b_1). Differently, for the ones with the highest content of MoS_2, the beads are densely distributed and much larger (Figure 5.5c_1), indicating much severer aggregation of MoS_2 nanosheets. In addition, some nanosheets can be found on the surface of the nanofibers. After carbonization, the "bead-on-string" morphology becomes more distinct due to the shrinkage of the nanofibers caused by conversion of PAN to carbon (Figure 5.5a_2-3c_2). The distribution of the nanosheets in the

carbonized nanofibers was further examined using TEM. As shown in Figure 5.5a_3, for MoS_2/C-47, all the MoS_2 nanosheets are embedded in the carbonized nanofibers and the loosely packed morphology of the nanosheets are retained. However, at higher MoS_2 contents, especially in MoS_2/C-95, severe aggregation of MoS_2 nanosheets occurs and some nanosheets are only partially embedded in the nanofibers (Figure 5.5b_3 and 3c_3), which may lack conductive and buffering support from the carbon matrix.

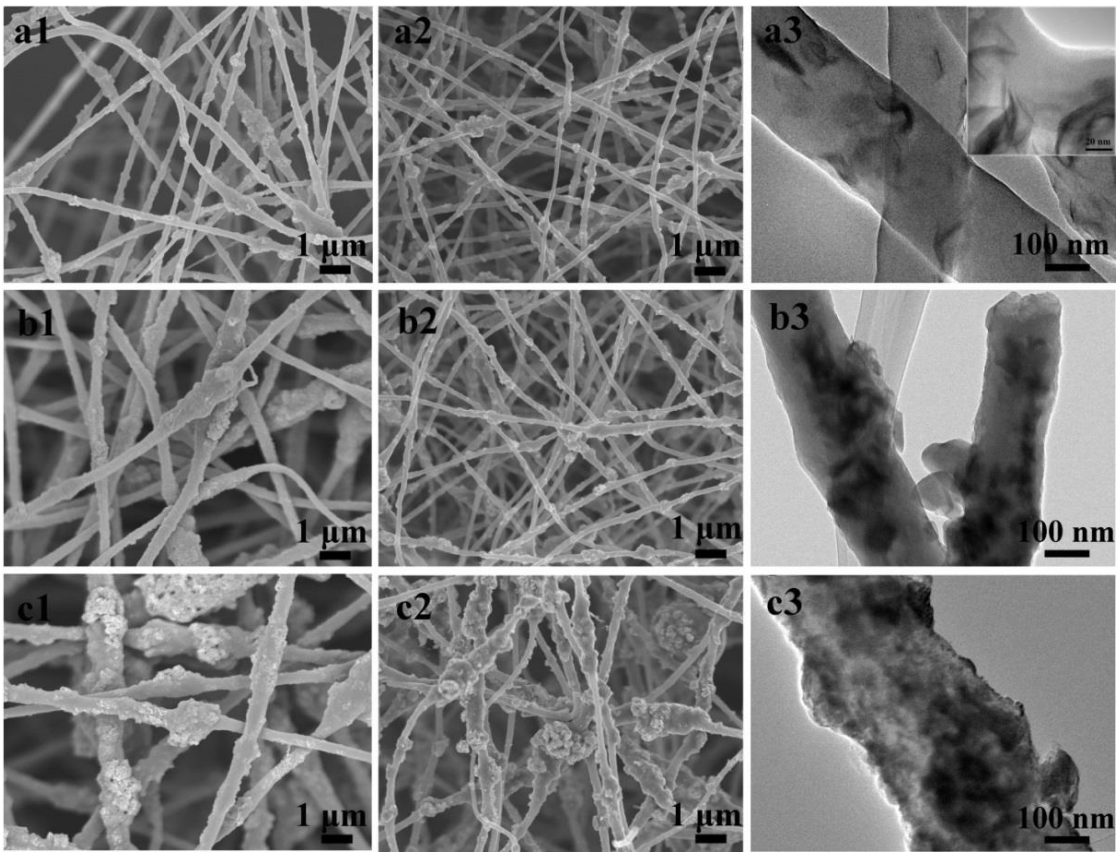

Figure 5.5 SEM (left, as-spun; middle, carbonized) and TEM (right) images of the hybrid nanofibers. The final MoS_2 contents for (a), (b) and (c) are 47, 73 and 95 wt%, respectively.

5.3.2 Electrochemical properties

To investigate the performance of the MoS_2/C nanofibrous mat as a LIB anode, firstly, the lithiation/delithiation behaviors were examined via CV, taking MoS_2/C-47 as an example (Figure 5.6a). The reduction peak at 1.6 V in the first cathodic curve is assigned to the reduction of PAN-derived oxygen/nitrogen-containing amorphous carbon.[23] The slope at about 1.1 V is indicative of the formation of Li_xMoS_2, which then decomposes

into Mo nanoparticles embedded in Li_2S, giving a cathodic peak at about 0.5 V. This two-step discharge process can be expressed by the following two reaction equations:[8]

$$MoS_2 + xLi^+ + xe^- = Li_xMoS_2 \quad (5.3)$$

$$Li_xMoS_2 + 4Li^+ + 4e^- = 2Li_2S + Mo / Li_x \quad (5.4)$$

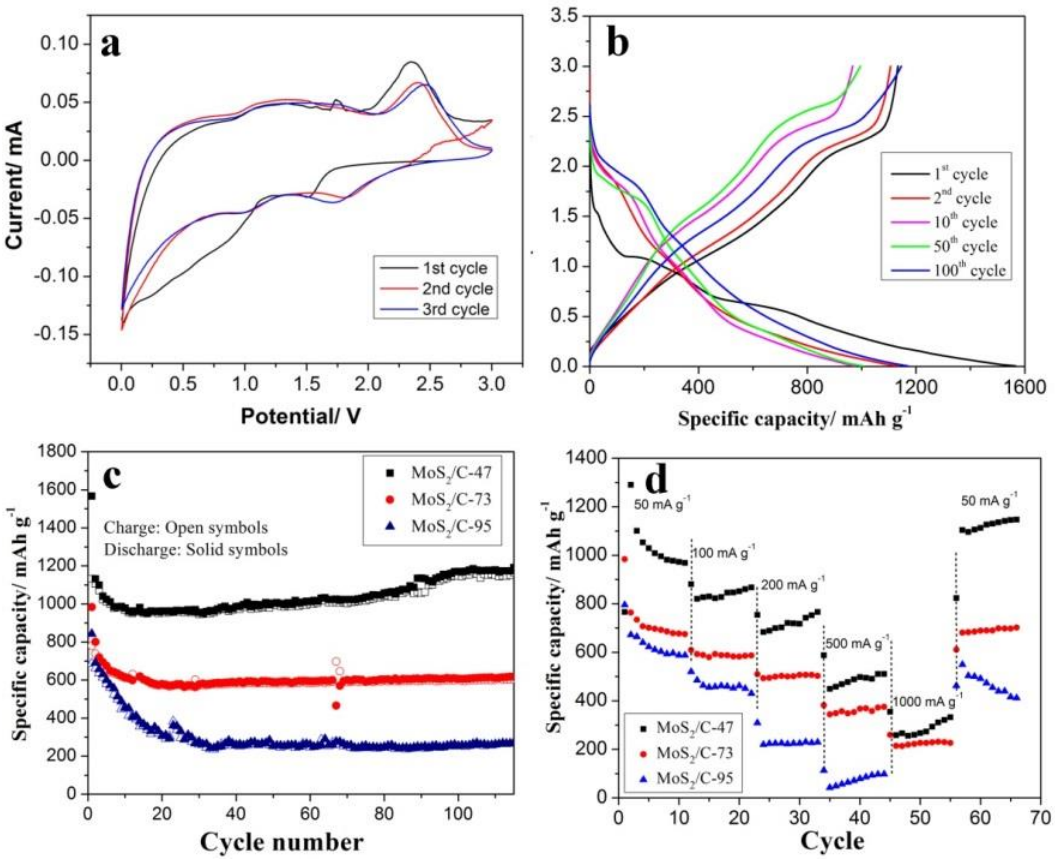

Figure 5.6 (a) Cyclic voltammograms of MoS_2/C-47 between 0.01 V and 3.0 V at a scan rate of 0.1 mV/s, (b) Discharge–charge profiles of MoS_2/C-47 for the 1st, 2nd, 10th, 50th and 100th cycles, (c) cycling performances of MoS_2/C-47, MoS_2/C-73 and MoS_2/C-95 at current density of 50 mA/g and (d) rate capabilities of the three samples.

The slope starts at ca. 1.0 V indicates the intercalation of Li^+ into the interlayer spacing of MoS_2. The inconspicuous conversion of Li_xMoS_2 to Mo and Li_2S is caused by the low crystallinity and disordered structure of MoS_2. The intercalation of Li^+ into the PAN-derived amorphous carbon may also cause the overlapping in the range (Figure 5.7a). [1,5] The slope below 0.3 V is assigned to the formation of a solid electrolyte interphase (SEI) film. During the anodic scanning, Li^+ stored within the amorphous carbon and defects of

MoS_2 are firstly released, leading to a broad oxidation peak centered at 1.2 V. Two pronounced peaks at 1.7 V and 2.3 V are associated with the delithiation of Mo and the oxidation of Li_2S to sulfur, respectively. Therefore, MoS_2 converts to a mixture of sulfur and Mo metal after the first cycle.[8] Accordingly in the following cycles, the reduction peak at 2.0 V can be attributed to the formation of Li_2S, and the association of Li^+ ions with Mo is found at 1.0 V.

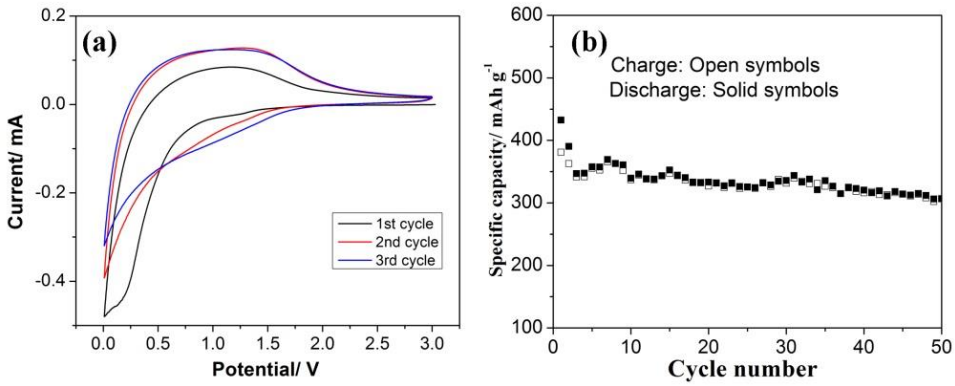

Figure 5.7 (a) Cyclic voltammograms between 0.01 V and 3.0 V at a scan rate of 0.1 mV/s and (b) cycling performances at current density of 50 mA/g of the neat electrospinning-derived carbon mat.

Figure 5.6c shows the cycling performance of the MoS_2/C nanofibers with varied MoS_2 contents. For comparison purpose, the capacity is normalized to the mass of MoS_2 by taking the capacity of amorphous carbon as that of graphite, 372 mAh/g (Figure 5.7b). It is shown that the cycling performance of MoS_2/C nanofibers is much better than that of the anodes based on the MoS_2 powder and MoS_2 nanosheets (Figure 5.6c). This is ascribed to the expanded interlayer *d* spacing of the MoS_2 nanosheets than that of the MoS_2 powder (Figure 5.8), as well as the fibrous architecture introduced by electrospinning (Figure 5.6c). On one hand, the larger interlayer distance of nanosheets relaxes the stress, lowers the energy barrier, and provides more defects for Li^+ ion intercalation. The small thickness of MoS_2 nanosheets shortens the electron and Li^+ ion pathway.[24] On the other hand, the carbon matrix stabilizes the disordered structure of MoS_2, tolerates local volume expansion/contraction during repetitive lithium storage/release and avoids the loss of polysulfides intermediate.[25-28] Furthermore, the conductivity of the whole anode is also greatly enhanced. The electrospun nanofibers,

typically meters in length, need only a few inter-fiber contacts to achieve sufficient electron transport, which is very important for the hybrid owing to the semi-conducting nature of MoS_2.

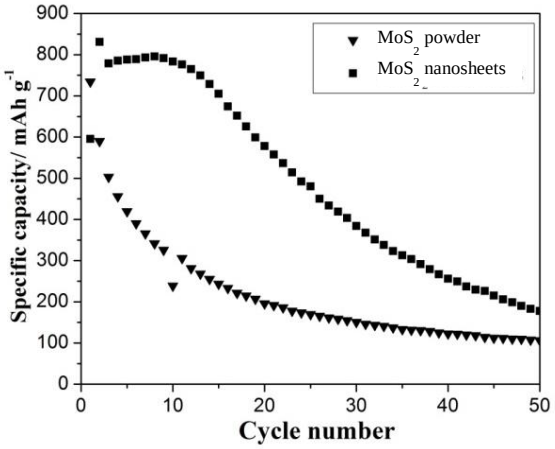

Figure 5.8 Cycling performances of MoS_2 nanosheets and MoS_2 powder prepared by casting. Both electrodes suffered rapid capacity fading due to structure destruction on cycling. However, the MoS_2 nanosheets showed a higher capacity at all cycles due to the larger interlayer spacing.

The initial charge capacity of MoS_2/C-47 is 1133 mAh/g with a coulombic efficiency of 73% (Figure 5.6b). The irreversible capacity loss is mainly caused by the formation of SEI film in the initial cycle. In the following cycles, the coulombic efficiency maintains at almost 100% with excellent cycling performance achieved. From 20 cycles onwards, the specific capacity of MoS_2/C-47 increases continuously and reaches 1150 mAh/g at the 100^{th} cycle, which may be attributed to the activation of Li^+ ion pathway between the electrolyte and electrode during cycling.[12] The stable cycling performance shows superiority over the other MoS_2-based anodes,[10,11,29] indicating that the carbon matrix not only enhances the electrical conductivity of the electrode, but also confines the active material within the matrix, alleviating the shuttle effect of soluble polysulfides.[30,31] Although MoS_2/C-73 has much higher MoS_2 content than MoS_2/C-47, the initial charge capacity and reversible capacity of MoS_2/C-73 are significantly lower than that of MoS_2/C-47. With the extremely high MoS_2 content, MoS_2/C-95 suffers more severe capacity loss upon cycling, from an initial capacity of 687 mAh/g to 260 mAh/g at the 30 cycle. The fast capacity decay of MoS_2/C-73 and MoS_2/C-95 can be attributed to

detachment of the MoS_2 nanosheets from the carbon nanofibers. More evidence for this will be shown later.

The rate capabilities of the MoS_2/C nanofibers are shown in Figure 5.6d. Beneficial from the good dispersion of MoS_2 in the carbon matrix, MoS_2/C-47 exhibits best rate performance among the three samples. Even at a high rate of 1000 mA/g, discharge capacity of 250-350 mAh/g can still be achieved. The reversible capacity restores to 1100 mAh/g when the current rate is changed back to 50 mA/g, and the capacity keeps ascending during subsequent cycling, approaching its initial capacity. On the contrary, the other two samples exhibit poor rate performance. MoS_2/C-95, for instance, only delivers a capacity of about 100 mAh/g at a current density of 500 mA/g, and suffers a significant capacity loss when the current rate is reset to 50 mA/g.

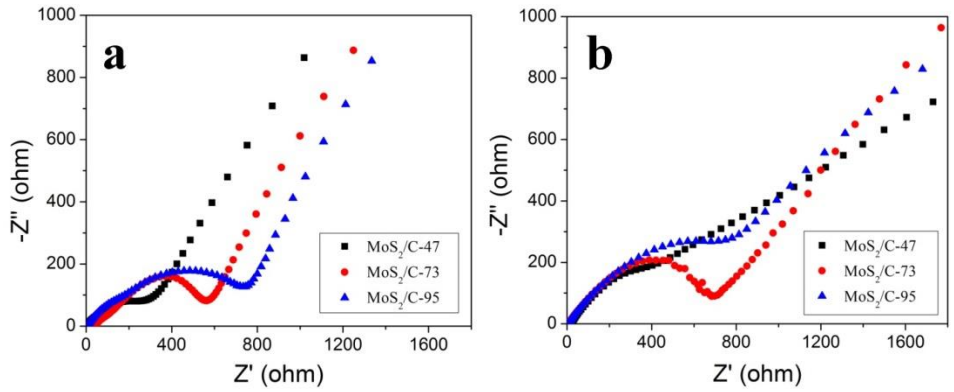

Figure 5.9 Nyquist plot of MoS_2/C-47, MoS_2/C-73 and MoS_2/C-95 measured at OCPs (a) before and (b) after cycles.

To verify the mechanism for the significant effect of MoS_2 content on electrochemical performance of the hybrid nanofibrous mats, AC impedance studies were carried out to analyze the charge-transfer resistance across MoS_2/C-47, MoS_2/C-73 and MoS_2/C-95 electrodes at open cycle potentials before and after cycling. The Nyquist plots obtained are shown in Figure 5.9. All the plots consist of two semicircles at high and medium frequencies and a straight line inclined at a constant angle at low frequencies, corresponding to the resistance of SEI film, charge transfer resistance at the electrolyte/electrode interface and the solid-state diffusion resistance of Li^+ in the electrode, respectively.[24] With the increase of MoS_2 content, the charge-transfer

resistance increases significantly, verifying that the aggregation of nanosheets at high MoS_2 contents indeed hinder electron and ion transport. After the cycling test, the interfacial charge-transfer resistance of the electrodes is higher than that before the cycling for all samples owing to the insulating SEI layer formed and the destruction of the MoS_2 structure during cycling. Nevertheless, MoS_2/C-47 still exhibits the lowest charge-transfer resistance, suggesting the smoothest diffusion for lithium ions and electrons, and hence justifying its highest cycle capacity.

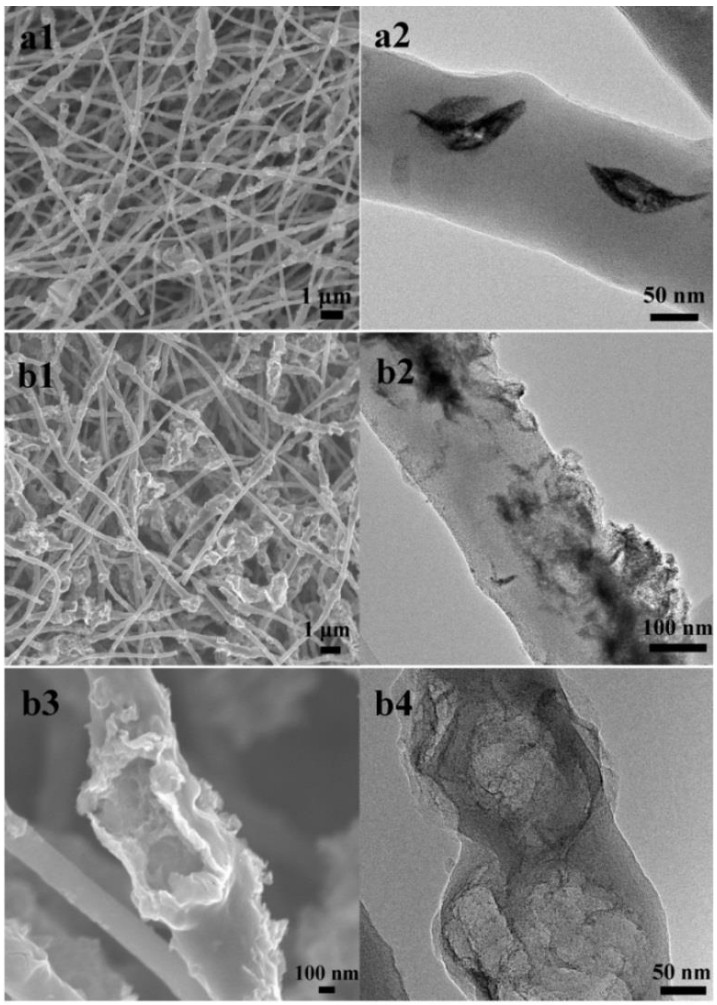

Figure 5.10 SEM (left) and TEM (right) images of (a) MoS_2/C-47 and (b) MoS_2/C-95 after cycling.

To further study the mechanism for the strong dependence of cycle capacity on MoS_2 content, the morphologies of MoS_2/C-47 and MoS_2/C-95 were examined after the cycling test. Before the examination, the electrodes were washed with ethanol for three times to

eliminate the residues. The SEM and TEM images in Figure 5.10a1-a2 show that the morphology of MoS_2/C-47 is intact after cycling, indicating effective confinement of active materials by the carbon matrix and thus excellent structure stability. By contrast, the surface of MoS_2/C-95 becomes smoother with lesser aggregated MoS_2 on surface after cycling, although the nanofibrous morphology remains (Figure 5.10b1-b2). Some partially embedded MoS_2 nanosheets are peeled off from the carbon nanofibers because the carbon matrix is unable to anchor the expanded nanosheets during cycling, leaving some large cavities on the nanofiber surface (Figure 5.10b3-b4). Such detachment induces severe capacity fading. Indeed, better electrochemical performance can be achieved by introducing a very thin carbon coating onto the surface of MoS_2/C-95 nanofibers (Figure 5.11). In this case, the carbon coating effectively prevents the detachment of MoS_2 nanosheets since they are well protected by carbon. The surface of MoS_2/C-95 becomes smoother after coating with a thickness of 5~10 nm. The cycling and rate capabilities are significantly improved compare to MoS_2/C-95, while still lower than that of MoS_2/C-47, which indicates that the well dispersion of MoS_2 within an electron and Li^+ ion conductive medium is crucial to achieve high electrochemical performance.

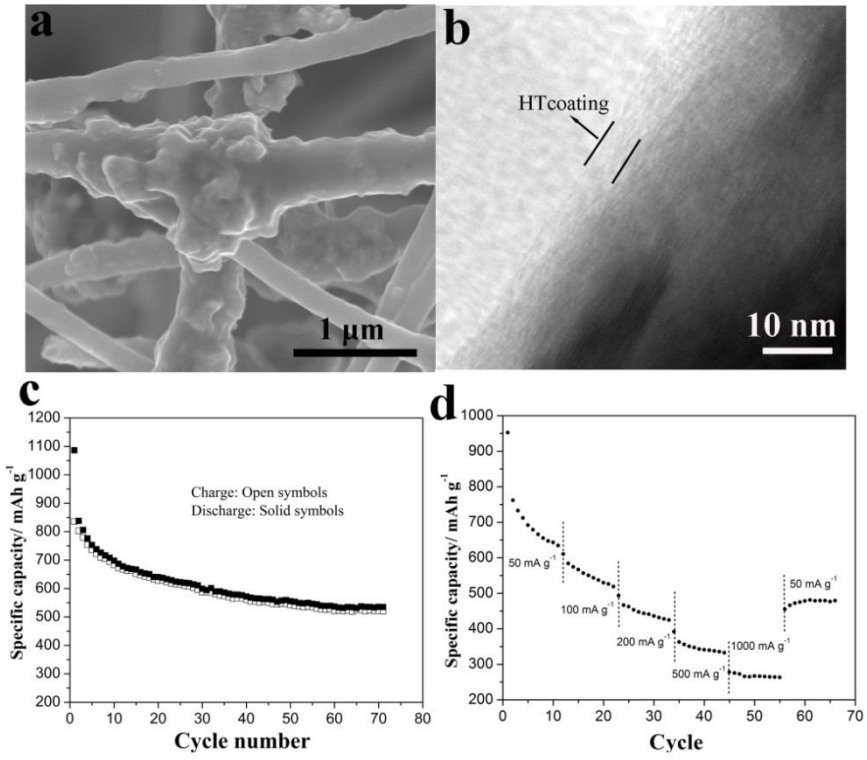

Figure 5.11 Morphologies and electrochemical characterization of MoS_2/C-95 with a thin layer of carbon coating: (a) SEM, (b) TEM, (c) cycling performances with a current density of 50 mA/g and (d) rate capability.

5.4 Conclusions

In this work, flexible and free-standing MoS_2/C hybrid nanofibrous mats were fabricated by electrospinning followed by carbonization for the first time, and their excellent performnce as anode materials for lithium ion batteries were demonstrated. Among the three MoS_2/C hybrids, MoS_2/C-47 shows the best electrochemical properties with a stable capacity of 1000-1200 mAh/g and a reversible capacity of ~350 mAh/g at a high current density of 1000 mA/g. The expansion of the interlayer *d* spacing of MoS_2 nanosheets, the effective confinement of the active material by the carbon matrix, the good electron transport provided by the high aspect ratio of the electrospinning-derived carbon nanofibers and the robustness of the hybrid nanofibrous structure are believed to be the main reasons for the high specific capacity, excellent cycling and rate stability achieved. The approach enables large-scale preparation of high-performance MoS_2 electrodes, and also provides a general strategy to immobilize soluble polysulfide intermediates in lithium-sulfur batteries. The highly flexible mats will also facilitate flexible LIBs.

References:

[1] Z. Wang, T. Chen, W. Chen, K. Chang, L. Ma, G. Huang, D. Chen and J. Y. Lee. *J. Mater. Chem. A*. **2013**, 1, 2202-2210.

[2] K. Bindumadhavan, S. K. Srivastava and S. Mahanty. *Chem. Commun.* . **2013**, 49, 1823-1825.

[3] K. Chang and W. Chen. *ACS Nano*. **2011**, 5, 4720-4728.

[4] S.-K. Park, S.-H. Yu, S. Woo, B. Quan, D.-C. Lee, M. K. Kim, Y.-E. Sung and Y. Piao. *Dalton Trans.* **2013**, 42, 2399-2405.

[5] K. Chang and W. Chen. *J. Mater. Chem.* **2011**, 21, 17175-17184.

[6] K. Chang, W. Chen, L. Ma, H. Li, H. Li, F. Huang, Z. Xu, Q. Zhang and J.-Y. Lee. *J. Mater. Chem.* **2011**, 21, 6251-6257.

[7] J. Xiao, D. Choi, L. Cosimbescu, P. Koech, J. Liu and J. P. Lemmon. *Chem. Mater.* **2010**, 22, 4522-4524.

[8] J. Xiao, X. Wang, X.-Q. Yang, S. Xun, G. Liu, P. K. Koech, J. Liu and J. P. Lemmon. *Adv. Funct. Mater.* **2011**, 21, 2840-2846.

[9] J. Xie, H. Zhang, S. Li, R. Wang, X. Sun, M. Zhou, J. Zhou, X. W. D. Lou and Y. Xie. *Adv. Mater.* **2013**, 25, 5807-5813.

[10] X. Fang, X. Yu, S. Liao, Y. Shi, Y.-S. Hu, Z. Wang, G. D. Stucky and L. Chen. *Microporous Mesoporous Mater.* **2012**, 151, 418-423.

[11] G. Du, Z. Guo, S. Wang, R. Zeng, Z. Chen and H. Liu. *Chem. Commun.* . **2010**, 46, 1106-1108.

[12] H. Hwang, H. Kim and J. Cho. *Nano Lett.* **2011**, 11, 4826-4830.

[13] S. Cavaliere, S. Subianto, I. Savych, D. J. Jones and J. Rozière. *Energy Environ. Sci.* **2011**, 4, 4761-4785.

[14] J. Kong, S. Y. Wong, Y. Zhang, H. R. Tan, X. Li and X. Lu. *J. Mater. Chem.* **2011**, 21, 15928-15934.

[15] L. Ji, Z. Lin, B. Guo, A. J. Medford and X. Zhang. *Chem. - Eur. J.* **2010**, 16, 11543-11548.

[16] L. Ji, K.-H. Jung, A. J. Medford and X. Zhang. *J. Mater. Chem.* **2009**, 19, 4992-4997.

[17] L. Ji and X. Zhang. *Energy Environ. Sci.* **2010**, 3, 124-129.

[18] J.-M. Tarascon and M. Armand. *Nature*. **2001**, 414, 359-367.

[19] E. Zussman, X. Chen, W. Ding, L. Calabri, D. Dikin, J. Quintana and R. Ruoff. *Carbon*. **2005**, 43, 2175-2185.

[20] M. Wang, G. Li, H. Xu, Y. Qian and J. Yang. *ACS Appl. Mater. Interfaces*. **2013**, 5, 1003-1008.

[21] H. Li, W. Li, L. Ma, W. Chen and J. Wang. *J. Alloys Compd.* **2009**, 471, 442-447.

[22] M. A. Santa-Ana, V. Sanchez and G. Gonzalez. *Electrochim. Acta*. **1995**, 40, 1773-1775.

[23] G. Huang, T. Chen, W. Chen, Z. Wang, K. Chang, L. Ma, F. Huang, D. Chen and J. Y. Lee. *Small*. **2013**, 9, 3693-3703.

[24] Q. Wang and J. Li. *J. Phys. Chem. C*. **2007**, 111, 1675-1682.

[25] M.-R. Gao, Y.-F. Xu, J. Jiang and S.-H. Yu. *Chem. Soc. Rev.* **2013**, 42, 2986-3017.

[26] X. Huang, Z. Zeng and H. Zhang. *Chem. Soc. Rev.* **2013**, 42, 1934-1946.

[27] T. Stephenson, Z. Li, B. Olsen and D. Mitlin. *Energy Environ. Sci.* **2014**, 7, 209-231.

[28] C.-H. Lai, M.-Y. Lu and L.-J. Chen. *J. Mater. Chem.* **2012**, 22, 19-30.

[29] S. Ding, J. S. Chen and X. W. Lou. *Chem. - Eur. J.* **2011**, 17, 13142-13145.

[30] X. Ji, K. T. Lee and L. F. Nazar. *Nat. Mater.* **2009**, 8, 500-506.

[31] D. Li, F. Han, S. Wang, F. Cheng, Q. Sun and W.-C. Li. *ACS Appl. Mater. Interfaces*. **2013**, 5, 2208-2213.

Chapter 6

Complexation-assisted Large-scale Aqueous Synthesis of SL-MoS_2/C Sandwich Structure as Advanced Anode Material for Lithium Ion Batteries*

In the work presented in this chapter, a novel SL-MoS_2/C sandwich structure is facilely prepared via a complexation-assisted aqueous route. A rufous complex is formed by simply mixing DOPA and Na_2MoO_4 aqueous solutions, which induces oligomerization of DOPA, yielding small complex domains dispersed in DOPA oligomers. The subsequent hydrothermal growth of MoS_2 is thus confined by this strong covalent bonding, giving small and disordered SL-MoS_2 crystals; while polydopamine is trapped in the van der Waals gap of MoS_2 and converted to carbon, forming a unique sandwich structure. The structural features, large interlayer spacing, sandwich structure and crumpled nanosheet morphology, render the SL-MoS_2/C excellent rate capability and cycle life as a LIB anode. Furthermore, this solvent-free synthesis strategy is proved to be a universal method to prepare other metal oxide/sulfide ultrafine crystals embedded in carbon matrix.

*This chapter published substantially as reference: **Zhao, C**.; Kong, J.; Yang, L.; Yao, X.; Phua, S.; Lu, X. Chem. Commun. 2014, 50, 9672.

6.1 Introduction

Chapter 5 has shown that the encapsulation of MoS_2 within electrospinnig-derived CNF can greatly imprved the cycling stability of MoS_2-based anode. The rate capability, however, is still limited because of the relatively thick carbon shell, as Li^+ have to pass through this "barrier" before they reach the MoS_2 core. The absulte capacities of the hybrid mats is also lower than 1000 mAh/g, probably due to the high carbon contents, which shows relatively low Li^+ storage capacity, and the mutilayer structure of hydrothermal synthesized MoS_2. Therefore, on one hand, though the rate performance of MoS_2 could also be greatly improved by integrating with carbonaceous materials,[1-6] the thickness of carbon phase should be carefully controlled. On the other, compared to MoS_2 with muitilayer structure, the SL-MoS_2 should be an ideal candidate for LIBs because of its largest surface area and shortest ionic diffusion length, let alone the abundant defects and interfaces.[7,8] The synthesis of SL-MoS_2/C, however, is still a big challenge due to the spontaneous restacking of SL-MoS_2.[9] Hydrothermal growth of MoS_2 with glucose typically yields few-layer MoS_2 in carbon.[10,11] Though the decomposition of $(NH_4)_2MoS_4$ under certain conditions gives SL-MoS_2,[12] large-scale aqueous synthesis of SL-MoS_2/C has not yet been realized.

DOPA has been widely used to prepare biomimetic adhesive coatings on various substrates via self-polymerization of DOPA in aqueous media.[13,14] A recent study revealed that polydopamine (PDOPA) coatings could be cacinated to layered carbon with electrical conductivities close to that of nitrogen-doped graphene.[15] Another interesting feature of DOPA is its complexation ability with various ligands, including molybdate, a widely used precursor in MoS_2 synthesis. Enlightened by these findings, we developed a DOPA-Mo^{VI} complexation-assisted approach for large-scale aqueous synthesis of SL-MoS_2/C. By simply mixing DOPA-HCl and Na_2MoO_4 aqueous solutions, DOPA-Mo^{VI} complex (DMC) are formed, which induces oligomerization of DOPA, yielding small DMC domains dispersed in DOPA oligomers. Subsequent hydrothermal growth of MoS_2 is thus confined, giving disordered SL-MoS_2 embedded in polydopamine-derived carbon. The distance between adjacent SL-MoS_2 layers is ~1.0 nm with a thin layer of carbon in between. Herein we report the structures and morphologies of the complex and resultant

SL-MoS_2/C as well as the formation mechanisms. Electrochemical properties of SL-MoS_2/C-based LIB anode, including rate capability and cycling stability, are also demonstrated.

6.2 Experimental Section

6.2.1 Materials

Dopamine hydrochloride (DOPA-HCl), TAA $Na_2MoO_4.2H_2O$, sodium tungstate dihydrate ($Na_2WO_4.2H_2O$) and ferric chloride hexahydrate ($FeCl_3.6H_2O$) were purchased from Sigma-Aldrich (USA) and used as received.

6.2.2 Synthesis

Seen in section 3.3.3

6.2.3 Characterization

The morphologies and structure of the hybrid nanofibers were studied by FESEM, TEM and XRD as described section 4.2.3. XPS measurements were conducted on a Kratos Analytical AXIS His spectrometer with a monochromatized Al Ka X-ray source (1486.6 eV photons). FTIR measurements were performed using a Shimadzu FTIR IR Prestige-21 using KBr pellets. The compositions of the samples were determined by thermogravimetric analysis (TA Q500). All the samples were heated from room temperature to 600 ^oC in air. The UV absorption spectra were measured using a Shimadzu UV-3600 UV–vis–NIR spectrophotometer. Raman spectra were obtained by using WITec CRM200 confocal Raman microscopy system (WITec, Germany) with a laser wavelength of 532 nm.

The electrochemical performances were evaluated with a standard CR2032 coin cell as described in section 5.2.3. The working electrode was composed of 70 wt% composites, 20 wt% Super P carbon black, and 10 wt% polyvinylidene fluoride. . The typical loading of the anode in the electrode was 2 to 3 mg. The specific capacity and current density were calculated based on the weight of the SL-MoS_2/C composite.

6.3 Results and discussion

6.3.1 Structural and morphological evolution

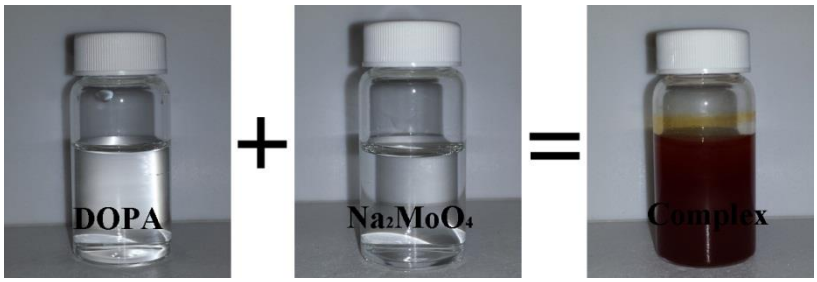

Figure 6.1 Photo images of DOPA-HCl, Na_2MoO_4 and DMC solutions.

SL-MoS_2/C was prepared by firstly mixing Na_2MoO_4 and DOPA-HCl aqueous solutions. Upon mixing the two colorless solutions, an orange-red suspension was formed (Figure 6.1). The DOPA-HCl and Na_2MoO_4 solutions do not show any absorption in the wavelength region of 300 to 700 nm, whereas a broad absorption band is observed at 407.5 nm for the suspension (Figure 6.2a), confirming the formation of DMC with Mo/DOPA ratio of 1:2,[16] i.e., the coordination number of Mo^{VI} is increased from four to six,[17] despite the feed molar ratio of Na_2MoO_4 to DOPA-HCl is ~1:3.5. FTIR spectra of DOPA-HCl, Na_2MoO_4 and DMC are shown in Figure 6.2b. Na_2MoO_4 does not have characteristic absorption band in 1100-1650 cm^{-1} region, while for DOPA, absorption bands at 1342, 1320, 1189 and 1174 cm^{-1} are observed, which can be assigned to CH_2, C-O-H bending vibration and C-O, C-C stretching vibration, respectively. All these bands are absent in the DMC spectrum while new bands emerge at 1537 cm^{-1} and 1429 cm^{-1}, indicating the formation of indole structure.[18,19] XPS studies show that the binding energiy of N 1s in DOPA is 402.1 eV (Figure 6.2c), while the single peak splits into two peaks at 398.6 and 401.5 eV, respectively, for DMC (Figure 6.2d), indicating the existence of secondary and tertiary amine groups.[20] The FTIR and XPS analyses indicate that oligomerization of DOPA occurs in the suspension, which involves cyclization of DOPA and assembly of DOPA units by covalent and non-covalent interactions.[21] Commonly PDOPA is spontaneously formed by pH-induced oxidative polymerization of DOPA at pH = 8.3. In this case, the pH of the suspension is only 6. Thus, it is likely that while DOPA donates its electrons to Mo^{VI} in DMC, the electron

density on DOPA is reduced, inducing oxidative oligomerization of DOPA. It is also striking to see that DMC exhibits sea-island morphology with evenly distributed Mo-rich islands of ca. 4 nm (Figure 6.2e). The islands are surrounded by wrinkled layer structure, suggesting the sea is composed of DOPA oligomers,[15] as illustrated in Figure 6.2f.

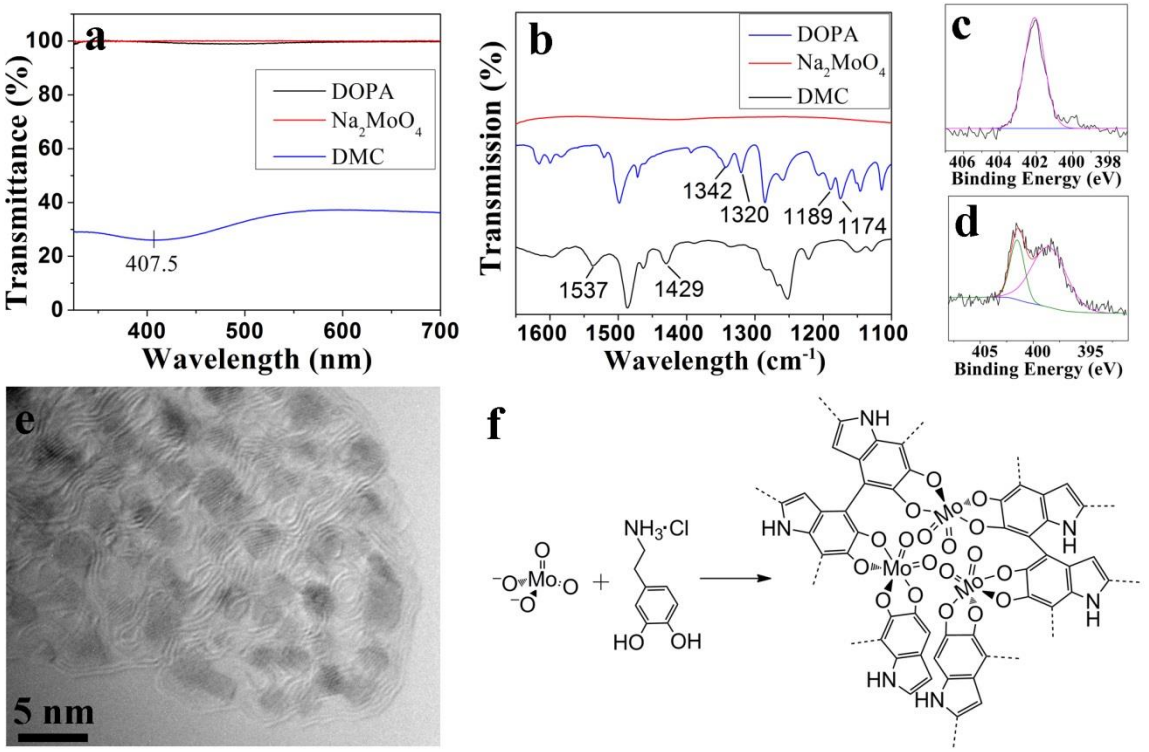

Figure 6.2 (a) UV-Vis and (b) FTIR spectra of DOPA-HCl, Na_2MoO_4 and DMC; XPS N 1s spectra of (c) DOPA-HCl and (d) DMC; (e) TEM image and (f) structural illustration of DMC.

The suspension was then mixed with TAA and hydrothermally treated at 200 ^oC for 16 h. TAA acts as both reducing and vulcanizing agent to convert molybdate to MoS_2, while PDOPA were partially carbonized under hydrothermal conditions (Figure 6.3a). The hydrothermal product (DMC-HT) was annealed at 700 ^oC in Ar to yield SL-MoS_2/C. The mass fractions of MoS_2 in DMC-HT and SL-MoS_2/C are 72 and 76 wt%, respectively, as determined by TGA (Figure 6.3b). The large weight loss between 200-450 ℃ is caused by the combustion of carbon and conversion of MoS_2 to MoO_3 in air.

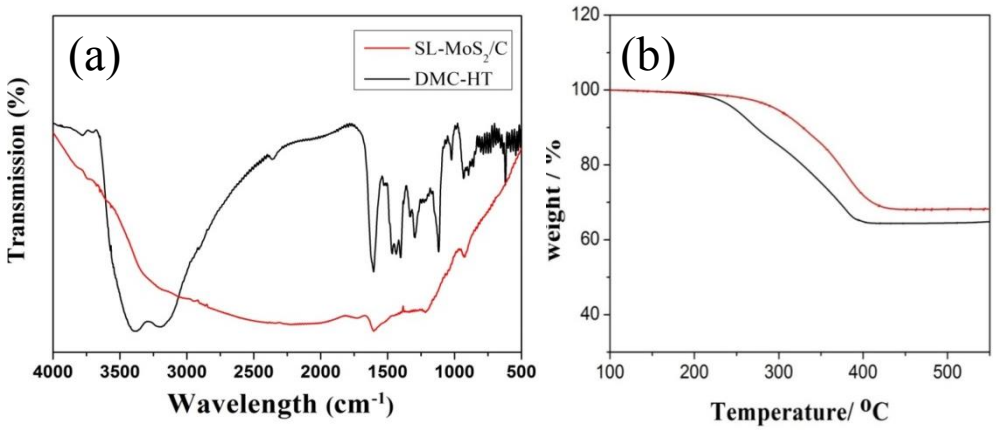

Figure 6.3 (a) FTIR spectra and (b) TGA curves of the DMC-HT and SL-MoS_2/C.

The morphology and structure of the DMC-HT and SL-MoS_2 were investigated by SEM, TEM and XRD. Both DMC-HT (Figure 6.4a) and SL-MoS2/C (Figure 6.4b) are porous agglomerates composed of crumpled nanoplates, similar to the morphology of reduced graphene oxide. TEM studies show that each nanoplate consists of 3-5 layers of disordered SL-MoS_2 embedded in carbon (Figure 6.4c and Figure 6.4d). In DMC-HT, the distance between adjacent SL-MoS_2 is around 1.05 nm, between which a fine line can be observed. This distance is much larger than that of bulk MoS_2, which is only 0.62 nm. It implies that some DOPA molecules intercalate into MoS_2 interlayer space, leading to a PDOPA-derived carbon layer sandwiched by SL-MoS_2. The length of each SL-MoS_2 is only 5 to 10 nm (Figure 6.4e). After annealing, the sandwich structure can be observed more clearly. The length of SL-MoS_2 is increased to 15-20 nm while the interlayer spacing is reduced to ~1.02 nm (Figure 6.4d). The XRD patterns of DMC-HT and SL-MoS_2/C are shown in Figure 6.5a. For SL-MoS_2/C, three distinct peaks at 2θ = 8.65^o, 33.1^o and 58.5^o correspond to (002), (100) and (110) planes of MoS_2, respectively. These peaks are at slightly higher angle and much stronger than that of DMC-HT, indicating annealing-induced shrinkage in interlayer spacing and perfection of MoS_2 crystallites. Compared to JCPDS 37–1492, the peak attributed to (002) plane of MoS_2 shifts from 14.4^o (d = 0.62 nm) to a much lower angle, 8.65^o (d = 1.01 nm), indicating an interlayer expansion of 0.39 nm, in accordance with the TEM results. It is worth noting that there is a weak peak at 2θ =17.9^o and its *d*-spacing (0.50 nm) is about half of that of MoS_2 interlayer spacing. This could be attributed to the spacing between adjacent SL-MoS_2 and carbon layer, confirming the sandwich structure.[22] No peak corresponding to carbon is

observed, implying the amorphous nature of the PDOPA-derived carbon. The Raman spectrum of SL-MoS_2/C is shown in Figure 6.5b. Two characteristic peaks at 388 and 410 cm^{-1} are observed for the MoS_2 with a Δ value of 22 cm^{-1}, which indicating that the nanosheets have either single-layer or few layer structure.[23]

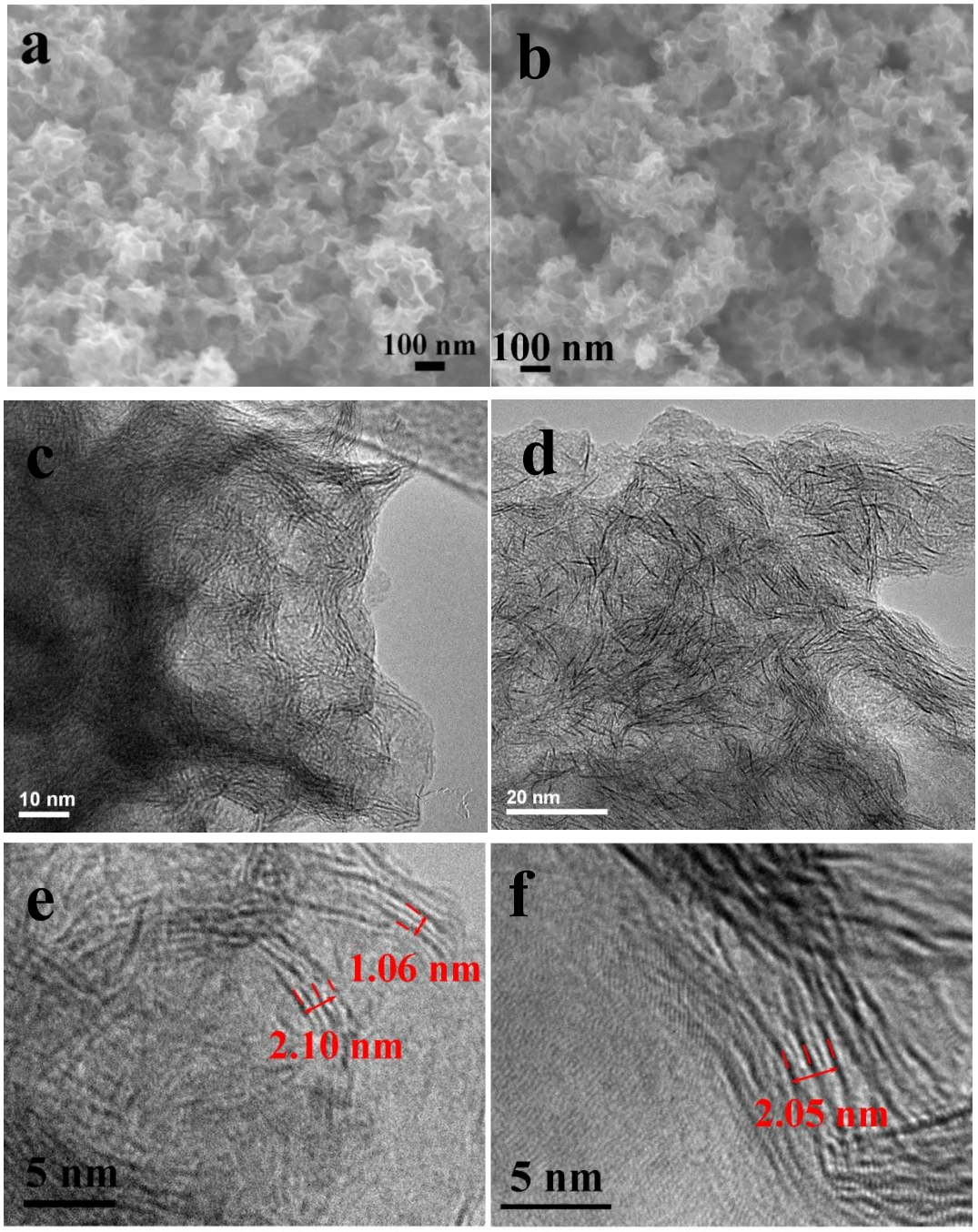

Figure 6.4 (a, b) SEM and (b-f) TEM images of DMC-HT and SL-MoS_2/C. (left column, DMC-HT; right column, SL-MoS_2/C)

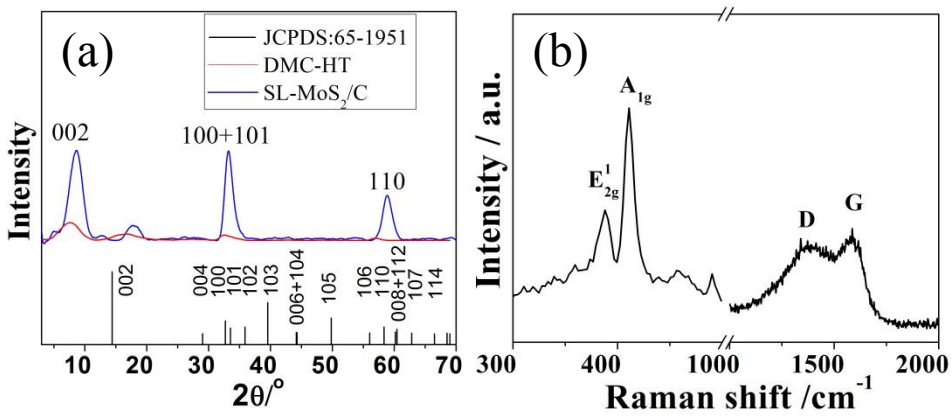

Figure 6.5 (a) XRD patterns and (b) Raman spectra of SL-MoS_2/C and DMC-HT.

6.3.2 Growth mechanism

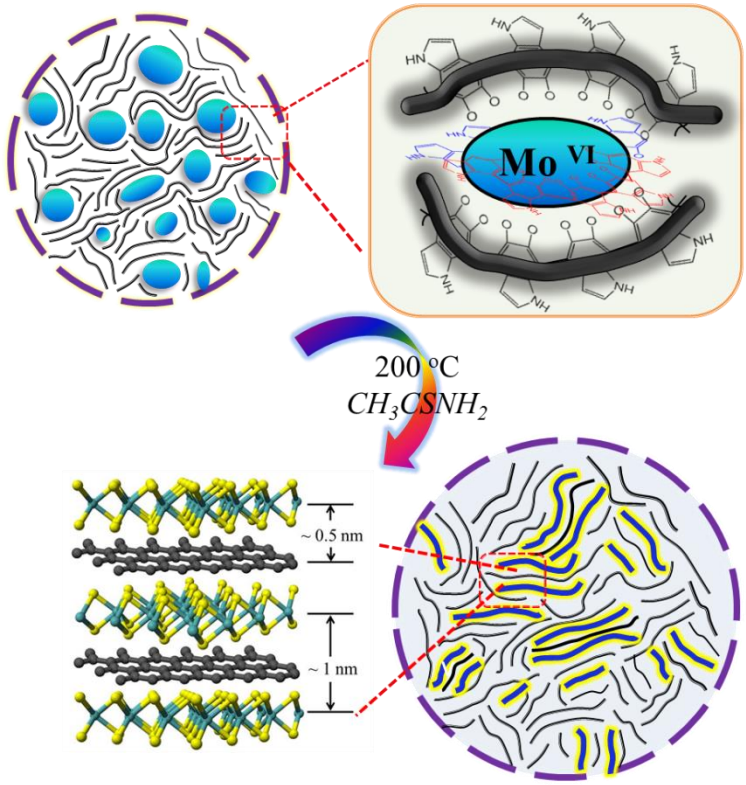

Figure 6.6 Schematic illustration of the growth mechanism of SL-MoS_2/C sandwich structure.

Based on the data presented above, a structural evolution mechanism is proposed, as illustrated in Figure 6.6. With the excessive amount of DOPA-HCl in the solution, MoO_4^{2-} form complex with DOPA, inducing oxidative oligmorization of DOPA because

of the electron transfer (from DOPA-Mo^{VI}) and leading to a precipitate in which DMC species are dispersed in PDOPA. In the subsequent hydrothermal process, PDOPA is partially carbonized under high temperature and pressure, while the growth of MoS_2 is confined by the strong chemical bonding and surrounding PDOPA, facilitating the formation of disordered SL-MoS_2 with limited size. Furthermore, some DOPA molecules in vicinity of Mo species intercalate into van de Walls gap of MoS_2 and are converted to carbon, enabling the formation of SL-MoS_2/C sandwich structure. It is worth mentioning that the synthesis strategy used here is not only feasible for large-scale aqueous production, but also can be transferred to other material systems to preparing untrafine metal oxides/sulphides crystals embedded in carbon matrix. For verification, the complexation-assisted syntheses of Fe_3O_4/C and WO_2/C composites were conducted. Their XRD patterns are shown in Figure 6.7. Obviously, the "sea-island" structure is perfectly reserved after hydrothermal reaction (Figure 6.8), indicating an *in-situ* conversion of Fe^{3+} and WO_4^{2-} to Fe_3O_4 and WO_2, respectively, as well as the carbonization of DOPA. The particles sizes of Fe_3O_4 and WO_2 are 5-10 nm and 3-5 nm, respectively. This is probably caused by the different precursor concentrations and/or metal-ligand ratios of Fe^{3+} (1:3) and WO_4^2 (1:2) with DOPA.

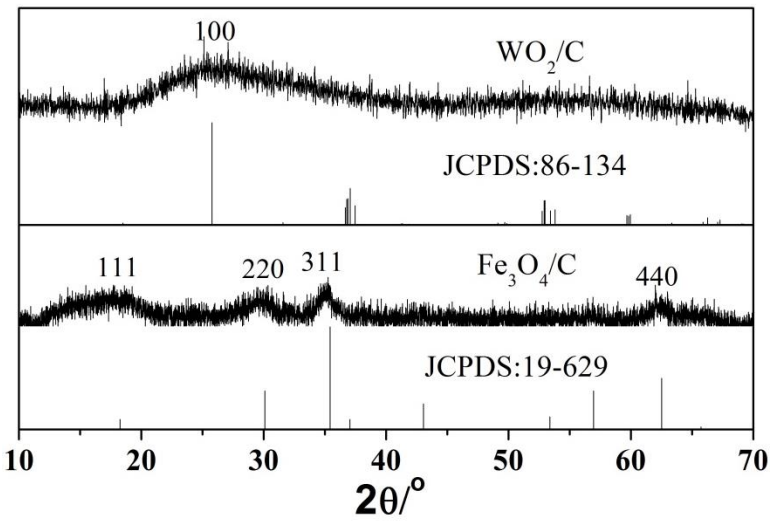

Figure 6.7 XRD patterns of Fe_3O_4/C and WO_2/C nanocomposites.

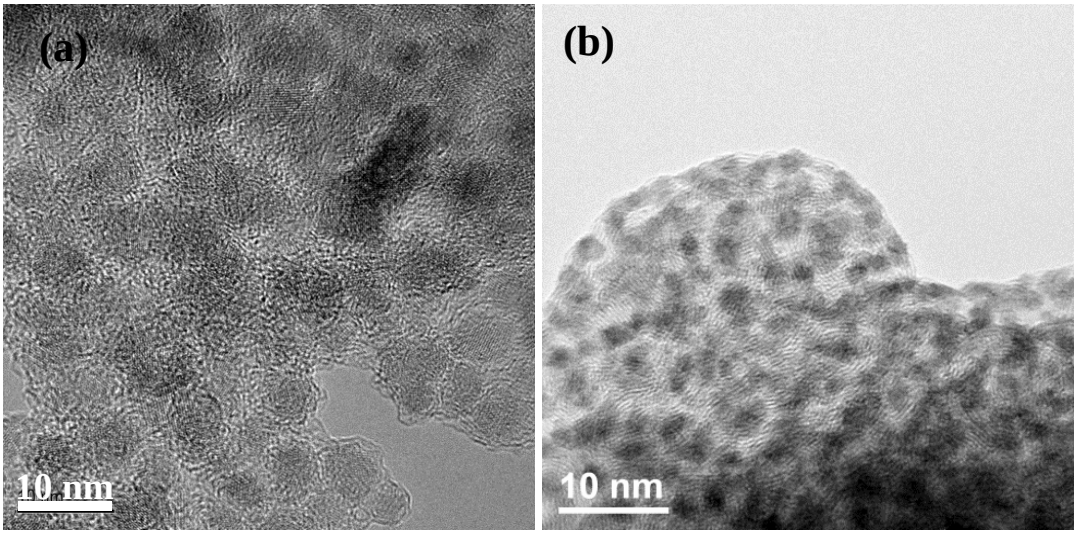

Figure 6.8 TEM images of (a) Fe_3O_4/C and (b) WO_2/C composites after annealing.

6.3.3 Electrochemical characterization

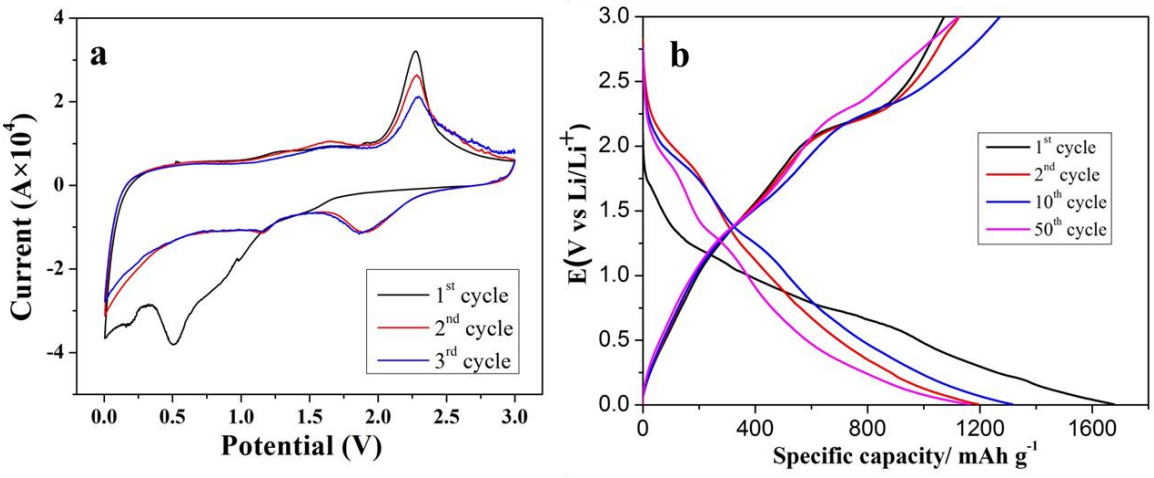

Figure 6.9 (a) CV between 0.01-3V with a can rate of 0.1 mV/s, and (b) GCD profiles at 50 mAh/g of the SL-MoS_2/C anode.

The electrochemical properties of the SL-MoS_2/C composite were evaluated with a standard CR2032 coin cell. The lithiation/delithiation behaviors of SL-MoS_2/C electrode were firstly examined via CV, as shown in Figure 6.9a. In the first discharge, a slope starts at about 1.5 V is indicative of the formation of Li_xMoS_2. The inconspicuous conversion is caused by the expanded (002) spacing, low crystallinity and disordered structure of SL-MoS_2.[8,24,25] The Li_xMoS_2 then decomposes into Mo nanoparticles embedded in Li_2S matrix, giving a cathodic peak at about 0.5 V. The slope below 0.25 V

is assigned to the formation of a SEI film. During the anodic scanning, Li^+ stored within the carbon and defects of SL-MoS_2 are firstly released, together with the partially oxidation of Mo, leading to broad oxidation peaks centered at about 0.5 V and 1.3 V, respectively. The pronounced peak at about 2.3 V is associated with the oxidation of Li_2S to sulfur.[26] Therefore, MoS_2 converts to a mixture of sulfur and Mo metal after the first cycle. Accordingly in the following cycles, the reduction peak at 2.0 V can be attributed to the formation of Li_2S, and the association of Li^+ ions with Mo is found at 1.0 V.[27] The GCD profiles of the SL-MoS_2/C electrode are shown in Figure 6.9b. In the first cycle, the electrode delivers an initial discharge capacity of 1678 mAh/g and charge capacity of 1072 mAh/g. A large capacity loss between the 1st and the following cycles is observed, which could be attributed to the formation of SEI layer and the structure conversion during the first discharge process.[20] These are consistent with the CV results.

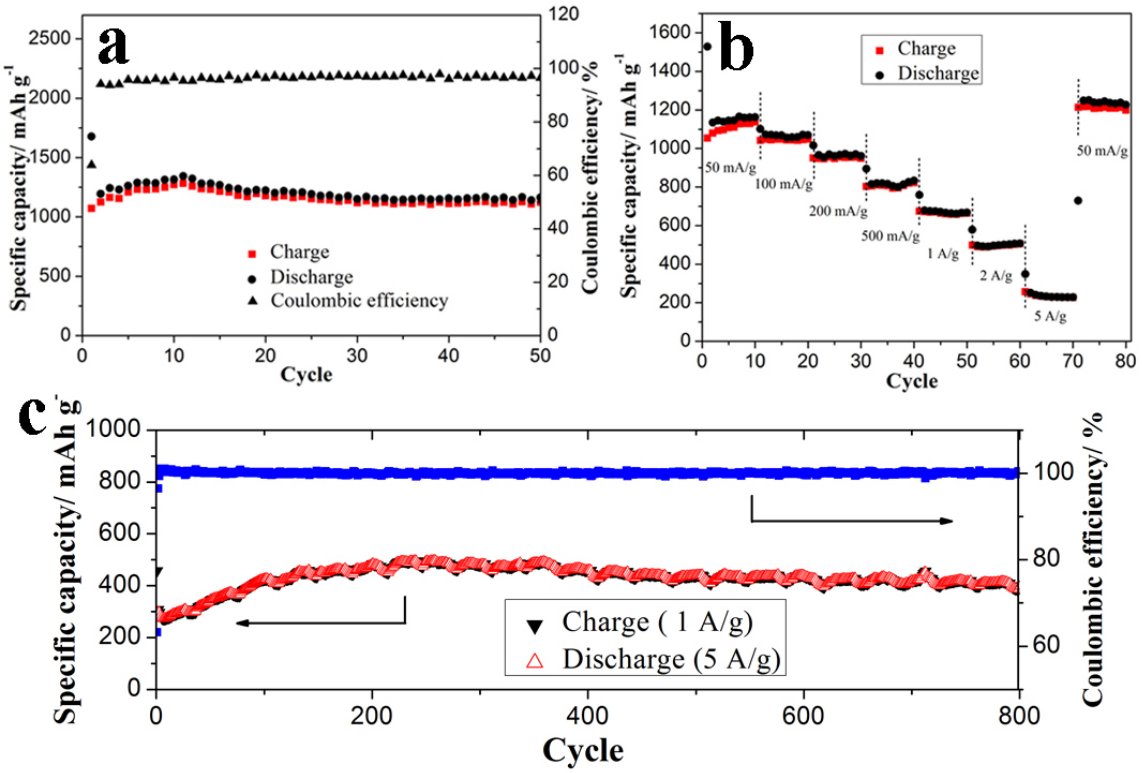

Figure 6.10 (a) Cycling stability at 50 mAh/g (b) rate capability and (c) high rate cycling performance at discharge rate of 5 A/g and charge rate of 1 A/g of the SL-MoS_2/C anode.

The cycling and rate capabilities of the SL-MoS_2/C electrode are shown in Figure 6.10. As can be seen form Figure 6.10a, the charge and discharge capacities are rapidly stabilized form the 2nd cycle onwards with coulombic efficiency of almost 100%, indicating excellent cycling stability. This is mainly due to the ultrafine crystal size of MoS_2 and thin nanosheet morphology, which ensures complete Li^+ alloying and de-alloying during cycling. The discharge and charge capacities maintain as high as 1164 mAh/g and 1123 mAh/g respectively at the 50th cycle, which is superior to other MoS_2-based electrodes.[1,28-30] The rate capability of the SL-MoS_2/C anode is shown in Figure 6.10b. It delivers charge capacities of 1130, 1050, 955, 820, 675, 505 and 230 mAh/g at 0.05, 0.1, 0.2, 0.5 1.0, 2.0, 5.0 A/g, respectively, demonstrating an excellent high-rate capability. The charge capacity rebounds to 1210 mAh/g when the current is reset to 50 mA/g. The superior cycling stability at high current densities is further demonstrated in Figure 6.10c. High coulombic efficiency of above 99 % is observed throughout the cycling regime. The reversible capacity increases continuously and reaches 500 mAh/g at the 260th cycle. This increment may be ascribed to the cycling-induced activation of Li^+ pathway and expansion of defect sites that facilitates intercalation of more Li^+.[5,7,25,27] The charge capacity keeps above 400 mAh/g at the 800th cycle. The excellent electrochemical performances are due to its unique structure and morphology. The small crystal size of SL-MoS_2 shortens the Li^+ diffusion distance, and the large interlayer distance facilitates fast Li^+ intercalation and helps to relieve the strain caused by Li^+ intercalation. The sandwich structure enhances electron conduction and structural stability.[3] The crumpled nanosheet morphology provides large surface area, benefiting fast electron/ion transport.

6.4 Conclusions

With the assistance of DMC, large-scale aqueous synthesis of SL-MoS_2/C is readily realized for the first time. Disordered SL-MoS_2, with length of 20 nm, are randomly oriented in PDOPA-derived carbon matrix. The distance between adjacent SL-MoS_2 is about 1.0 nm, with a carbon layer in between. These structural characteristics make SL-MoS_2/C an excellent LIB anode material. A reversible capacity of 400 mAh/g can be achieved after cycling at a discharge rate of 5 A/g for 800 cycles. More importantly, this

synthesis strategy is simple and scalable, and could be extended to prepare a series of metal oxides/sulfides and carbon composites, Fe_3O_4/C and WO_2/C for instance, where defects-rich structures with ultrafine crystals are crucially needed.

References:

[1] H. Yu, C. Zhu, K. Zhang, Y. Chen, C. Li, P. Gao, P. Yang and Q. Ouyang. *J. Mater. Chem. A*. **2014**, 2, 4551-4557.

[2] C. Lu, W.-w. Liu, H. Li and B. K. Tay. *Chem. Commun.* . **2014**, 50, 3338-3340.

[3] K. Chang and W. Chen. *Chem. Commun.* . **2011**, 47, 4252-4254.

[4] S. K. Das, R. Mallavajula, N. Jayaprakash and L. A. Archer. *J. Mater. Chem.* **2012**, 22, 12988-12992.

[5] C. Zhao, J. Kong, X. Yao, X. Tang, Y. Dong, S. L. Phua and X. Lu. *ACS Appl. Mater. Interfaces*. **2014**, 6, 6392-6398.

[6] X. Cao, Y. Shi, W. Shi, X. Rui, Q. Yan, J. Kong and H. Zhang. *Small*. **2013**, 9, 3433-3438.

[7] K. Chang, D. Geng, X. Li, J. Yang, Y. Tang, M. Cai, R. Li and X. Sun. *Adv. Energy Mater.* **2013**, 3, 839-844.

[8] K. Chang and W. Chen. *J. Mater. Chem.* **2011**, 21, 17175-17184.

[9] G. Du, Z. Guo, S. Wang, R. Zeng, Z. Chen and H. Liu. *Chem. Commun.* . **2010**, 46, 1106-1108.

[10] K. Chang and W. Chen. *ACS Nano*. **2011**, 5, 4720-4728.

[11] K. Chang, W. Chen, L. Ma, H. Li, H. Li, F. Huang, Z. Xu, Q. Zhang and J.-Y. Lee. *J. Mater. Chem.* **2011**, 21, 6251-6257.

[12] C. Zhu, X. Mu, P. A. van Aken, Y. Yu and J. Maier. *Angew. Chem., Int. Ed.* **2014**, 53, 2152-2156.

[13] H. Lee, S. M. Dellatore, W. M. Miller and P. B. Messersmith. *Science*. **2007**, 318, 426-430.

[14] L. Yang, S. L. Phua, J. K. H. Teo, C. L. Toh, S. K. Lau, J. Ma and X. Lu. *ACS Appl. Mater. Interfaces*. **2011**, 3, 3026-3032.

[15] J. Kong, W. A. Yee, L. Yang, Y. Wei, S. L. Phua, H. G. Ong, J. M. Ang, X. Li and X. Lu. *Chem. Commun.* . **2012**, 48, 10316-10318.

[16] K. Kustin and S.-T. Liu. *J. Am. Chem. Soc.* **1973**, 95, 2487-2491.

[17] A. K. Duhme-Klair. *Eur. J. Inorg. Chem.* **2009**, 2009, 3689-3701.

[18] M. J. Sever, J. T. Weisser, J. Monahan, S. Srinivasan and J. J. Wilker. *Angew. Chem.* **2004**, 116, 454-456.

[19] L. Wang, D. Wang, Z. Dong, F. Zhang and J. Jin. *Small*. **2014**, 10, 998-1007.

[20] Z. Li, Z. Xu, X. Tan, H. Wang, C. M. B. Holt, T. Stephenson, B. C. Olsen and D. Mitlin. *Energy Environ. Sci.* **2013**, 6, 871-878.

[21] S. Hong, Y. S. Na, S. Choi, I. T. Song, W. Y. Kim and H. Lee. *Adv. Funct. Mater.* **2012**, 22, 4711-4717.

[22] R. Bissessur and P. K. Liu. *Solid state ionics*. **2006**, 177, 191-196.

[23] K.-K. Liu, W. Zhang, Y.-H. Lee, Y.-C. Lin, M.-T. Chang, C.-Y. Su, C.-S. Chang, H. Li, Y. Shi, H. Zhang, C.-S. Lai and L.-J. Li. *Nano Lett.* **2012**, 12, 1538-1544.

[24] Z. Wang, T. Chen, W. Chen, K. Chang, L. Ma, G. Huang, D. Chen and J. Y. Lee. *J. Mater. Chem. A*. **2013**, 1, 2202-2210.

[25] H. Hwang, H. Kim and J. Cho. *Nano Lett.* **2011**, 11, 4826-4830.

[26] X. Fang, X. Yu, S. Liao, Y. Shi, Y.-S. Hu, Z. Wang, G. D. Stucky and L. Chen. *Microporous Mesoporous Mater.* **2012**, 151, 418-423.

[27] J. Xiao, X. Wang, X.-Q. Yang, S. Xun, G. Liu, P. K. Koech, J. Liu and J. P. Lemmon. *Adv. Funct. Mater.* **2011**, 21, 2840-2846.

[28] L. Yang, S. Wang, J. Mao, J. Deng, Q. Gao, Y. Tang and O. G. Schmidt. *Adv. Mater.* **2013**, 25, 1180-1184.

[29] M. Wang, G. Li, H. Xu, Y. Qian and J. Yang. *ACS Appl. Mater. Interfaces*. **2013**, 5, 1003-1008.

[30] U. K. Sen and S. Mitra. *ACS Appl. Mater. Interfaces*. **2013**, 5, 1240-1247.

Chapter 7

Self-assembly-induced Alternately Stacked Single-layer MoS_2 and *N*-doped graphene: a Novel van der Waals Heterostructure for Lithium-Ion Batteries*

In this chapter, we present a facile self-assembly strategy for fabricating van der Waals heterostructures from isolated two-dimensional single layer crystals for the first time. Specifically, a novel nitrogen-doped graphene/MoS_2 nanocomposites with well-defined alternating structure was prepared through electrostatic attraction-induced self-assembly. When used as an anode for the LIBs, it exhibits excellent cycling stability and high rate capability because the alternating structure, which triggers synergistic effect between the two components. This self-assembly approach may also be adopted for surface modification of MoS_2 or fabrication of MoS_2-based nanocomposites. The resultant nanocomposites with unique alternating structure can also be used in other electrochemical applications.

*This chapter published substantially as reference: **Zhao, C**.; Wang, X.; Kong, J.; Ang, J. M.; Lee, P. S.; Liu, Z.; Lu, X. ACS Appl. Mater. Interface s 2016, 8, 2372.

7.1 Introduction

Chapter 6 has shown that the electrochemical performance of MoS_2-based anodes could be greatly improved through novel morphology and structure design. It also indicates that the presence of atomic interfaces plays an important role in Li^+ storage. In this regard, the stacking of SL-MoS_2 with other 2D monolayers (graphene for example) is an ideal superstructure for high electrochemical performance. Heterostructures made by stacking of different atomic layers (van der Waals heterostructure) are a class of materials with fascinating properties.[1] The structural similarity of MoS_2 and graphene provides a high possibility to fabricate MoS_2/graphene heterostructures. It is believed that the intimate face-to-face contact between MoS_2 and graphene may trigger synergistic effects and maximize the Li^+ storage potential of both components. Self-assembly of monolayers of two different types of 2D materials is a facile strategy for fabrication of van der Waals nanocomposites with well-defined alternating structure. However, although both exfoliated MoS_2[2-4] and graphene oxide (GO) can be suspended in aqueous solutions, owing to their negatively charged surfaces, direct assembly of MoS_2 monolayers and GO into alternately stacked MoS_2/GO heterostructure is hampered by the electrostatic repulsion between the two components; simply mixing the two components would lead to restacked MoS_2 dispersed in GO. Besides, the mismatch in lateral dimensions of MoS_2 and GO also makes the preparation of stable MoS_2/GO heterostructure difficult. Previous work has shown that PDOPA, a biomimetic adhesive polymer,[5,6] can be easily coated on various material surfaces by covalent polymerization of DOPA as well as non-covalent self-assembly.[7,8] The carbonized thin PDOPA coatings have similar structure and electrical conductivity to those of multilayered graphene doped with heteroatoms.[9] Inspired by the self-assembly potential of DOPA and intercalation chemistry of MoS_2,[10,11] in this work, for the first time a nitrogen-doped graphene (NDG)/MoS_2 van der Waals heterostructure with well-defined alternating NDG/MoS_2 layers was fabricated via a facile electrostatic attraction-induced self-assembly approach. Bulk MoS_2 was first exfoliated to monolayers through intercalation with Li^+. Positively charged DOPA monomers were then attached and adsorbed on the negatively charged MoS_2 surfaces

through electrostatic interaction, triggering spontaneous self-assembly of the DOPA-modified MoS_2 monolayers to form a new intercalated compound, $(DOPA)_xMoS_2$. Without the need of DOPA polymerization, the intercalated DOPA can be directly *in-situ* converted to NDG in the confined 2D space by carbonization, giving rise to the NDG/MoS_2 van de Waals heterostructure. The unique feature of the NDG/MoS_2 heterostructure lies in its alternately stacked structure with largely expanded interlayer space. It not only well addresses the issue of poor electron and Li^+ conductivity of MoS_2-based anodes, but also provides additional Li^+ storage sites at the MoS_2-NDG interface, effectively protects the active materials and accommodates the volume change during cycling. These endow the NDG/MoS_2 heterostructure with low charge-transfer resistance, high sulfur reservation and structural robustness, rendering it an advanced LIB anode material with excellent cycling stability and high rate capability.

7.2 Experimental Section

7.2.1 Materials

The n-butyllithium solution (1.6 M in hexane) were purchased from Sigma-Aldrich (USA) and used as received.

7.2.2 Synthesis

Seen in section 3.3.4

7.2.3 Characterization

The morphologies and structure of the hybrid nanofibers were studied by FESEM, TEM, XPS, XRD, FTIR, Roman and TGA as described section 6.2.3.

The electrochemical performances were evaluated with a standard CR2032 coin cell. The working electrode was composed of 70 wt% composites, 20 wt% Super P carbon black, and 10 wt% polyvinylidene fluoride. The capacities are calculated based on the mass of NDG/MoS_2.

7.3 Result and Discussion

7.3.1 Fabrication of the NDG/MoS_2 Van der Waals heterostructure

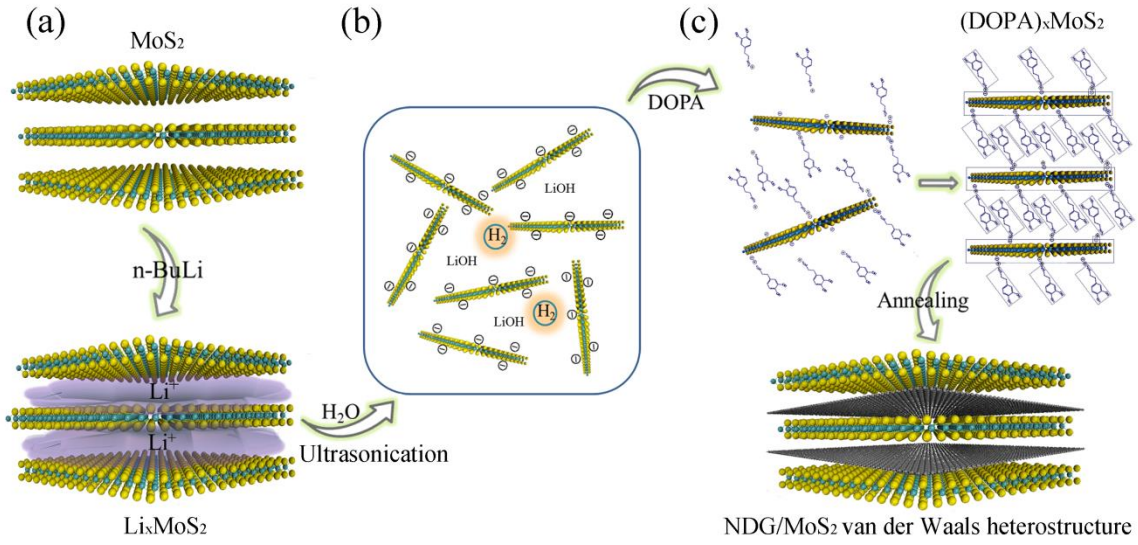

Figure 7.1 Schematic illustration detailing the fabrication process of NDG/MoS_2 van der Waals heterostructure.

The fabrication process for the NDG/MoS_2 heterostructure is illustrated in Figure 7.1. Bulk MoS_2 was firstly intercalated by Li^+ due to the weak interlayer interaction, forming the Li_xMoS_2 intermediate (Figure 7.1a). Once in contact with water, the Li^+ ions were hydrated, causing an expansion of the interlayer space, while water was reduced to H_2 and OH^- by the negatively charged MoS_2.[12] The microbubbles formed further pushed the expanded MoS_2 layers apart, yielding a stable colloidal suspension of MoS_2 monolayers (Figure 7.1b). The negative charges on the MoS_2 surface hindered restacking of the MoS_2 monolayers, which was confirmed by the zeta potential test result (> -25 mV). When the DOPA-HCl aqueous solution was added, the positively charged ammonium groups (NH_3^+) of DOPA was attracted and adsorbed onto the surfaces of the MoS_2 monolayers due to electrostatic interaction. This "neutralization" of surface charges destabilized the colloidal particles and caused flocculation of the suspension immediately, during which DOPA monomers were sandwiched by MoS_2 monolayers and self-assembly into an intercalated intermediate $(DOPA)_xMoS_2$ (Figure 7.1c). It is noted that, the composition of the $(DOPA)_xMoS_2$ changed only slightly when varying the feed ratio of DOPA to MoS_2,

implying the electrostatic attraction-induced self-assembly dominated in this process. When annealed, DOPA molecules were polymerized in the confined MoS_2 interlayer space and *in-situ* carbonized to NDG, while the MoS_2 preserved its monolayer morphology due to the separation by NDG, forming a novel NDG/MoS_2 nanocomposite with well-defined alternating structure.

7.3.2 Structural verification

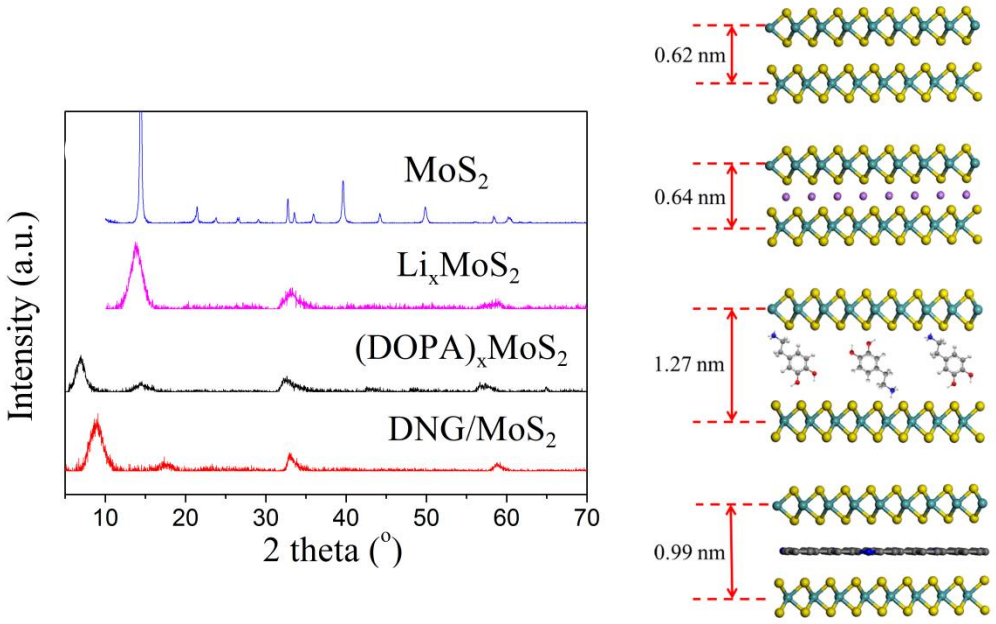

Figure 7.2 XRD patterns and schematics of pristine MoS_2, Li_xMoS_2, $(DOPA)_xMoS_2$ and NDG/MoS_2.

The extent of intercalation and carbonization could be monitored by the interlayer distance of MoS_2 derived from the position of its (*002*) XRD peak (Figure 7.2). The XRD pattern of original MoS_2 matches well with hexagonal 2H-MoS_2 (JCPDS: 65-1951), which shows a strong diffraction peak at 14.4^o with an interlayer distance of 0.62 nm. This distance increases slightly to 0.64 nm (13.9^o) after the Li^+ intercalation, accompanied by a phase transition from 2H to 1T MoS_2.[13] After the intercalation of DOPA, the (*002*) peak moves significantly to a lower angle (7.0^o), indicating a further expansion of 0.65 nm along the *c*-axis and the formation of a new intercalated compound, $(DOPA)_xMoS_2$. The increased interlayer spacing is smaller than the length of DOPA monomer (0.75-8.0 nm). It thus can be speculated that with the -NH_3^+ group interacting

with the MoS_2 monolayer, the benzenediol tail of DOPA may adopt a tilted arrangement to increase the structural stability of $(DOPA)_xMoS_2$.[14,15] It is reported that DOPA can self-polymerize under mild basic condition and this process usually takes hours.[6] Due to the existence of hydrolyzed LiOH, the PH of the exfoliated MoS_2 suspension is around 11.4, which may induce oxidative polymerization of DOPA. To confirm this, FTIR measurement was conducted and the spectra are shown in Figure 7.3a. The characteristic bands of DOPA can be found at 1603/1488 cm^{-1}, 1270 cm^{-1} and 1192 cm^{-1}, corresponding to the in-plane skeletal vibration of aromatic ring, C-N and O-H stretching vibration, respectively. The small shoulder peak at 1717 cm^{-1} can be assigned to the stretching vibration of C=O, which derived from the oxidation of DOPA.[8] The absence of indole structure indicates DOPA polymerization doesn't take place.[16] Therefore, DOPA exists in both original and oxidized forms between MoS_2 monolayers probably due to the anchoring of its $-NH_3^+$ groups and the very fast "neutralization" between DOPA and MoS_2 (within minutes). All the aforementioned FTIR bands almost could not be observed after annealing. Meanwhile, the (*002*) diffraction peak shifts to 8.9^o, indicating that the expansion in *c*-axis direction shrinks to 0.37 nm (Figure 7.2). This increment is close to the interlayer distance of graphite (0.34 nm), implying the *in situ* conversion of DOPA to NDG lying parallel between MoS_2.[16,17] In addition, after annealing, a high order (*00l*) peak is also observed at 17.6^o with an interlayer distance of 0.50 nm, which is exactly half of the MoS_2 interlayer spacing. This can be attributed to the distance between NDG and MoS_2 monolayers and confirms the successful fabrication of the NDG/MoS_2 heterostructure. The average thickness of the heterostructure is calculated to be ~7.9 nm based on the full width at half maximum (FWHM) of the (*002*) diffraction peak, corresponding to 8 pairs of alternately stacked MoS_2 and NDG.

The conversion from $(DOPA)_xMoS_2$ to the NDG/MoS_2 is further studied by Raman. As shown in Figure 7.3b, the $(DOPA)_xMoS_2$ shows two peaks at 378 and 401 cm^{-1}, corresponding to the in-plane (E^1_{2g}) and out of plane (A_{1g}) vibration of MoS_2. These two peaks are well retained after carbonization, indicating the restacking of MoS_2 does not occur,[18] while two characteristic peaks of carbon materials, the D and G bands, emerge at 1386 and 1576 cm^{-1}, respectively, with an intensity ratio of 0.9, indicating the defect-rich nature of NDG.

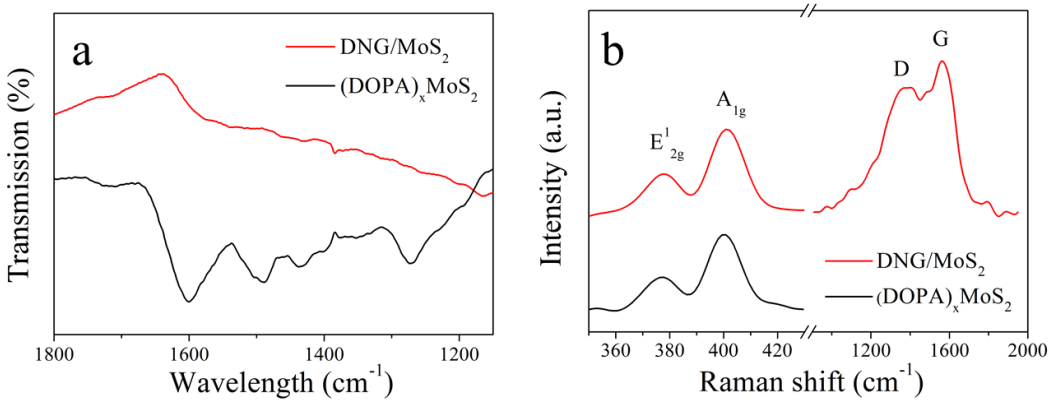

Figure 7.3 (a) FTIR and (b) Roman spectra of the $(DOPA)_xMoS_2$ and NDG/MoS_2.

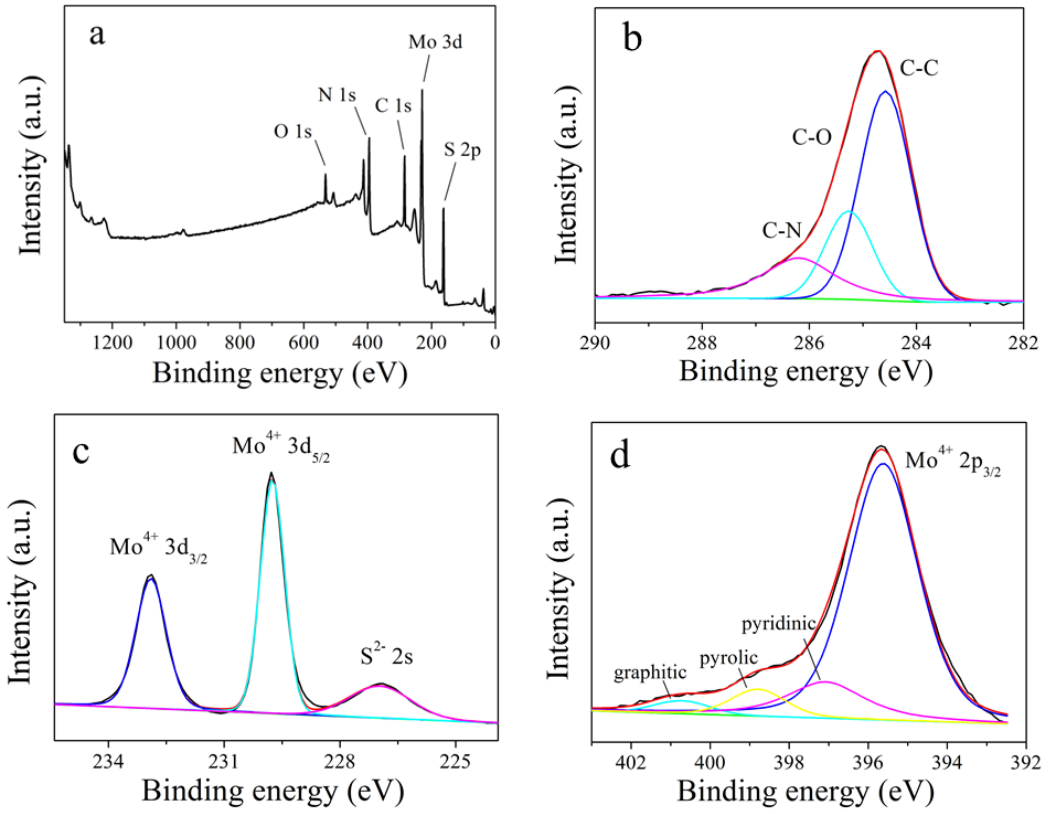

Figure 7.4 (a) XPS survey (b) C 1s, (c) Mo 3d and (d) N 1S spectra of the NDG/MoS_2 nanocomposite.

The XPS measurement was conducted to probe the chemical states of Mo, N and C. The XPS survey spectrum of the NDG/MoS_2 heterostructure is shown in Figure 7.4a. As can be seen from Figure 7.4b, the C 1s spectrum can be deconvoluted into 3 components at

284.6, 285.3 and 286.2 eV, corresponding to the sp2 C and sp3 C in C-O and C-N, respectively.[19] The C-N configuration accounts for 21% of all carbon. Figure 7.4c shows the Mo 3d region with high resolution. The peaks at 232.9 and 229.8 eV could be assigned to the $3d_{3/2}$ and $3d_{5/2}$ of Mo^{4+} in MoS_2, while the lower energy peak at 227.0 eV could be assigned to the 2s of S^{2-}. No oxidation and reduction of Mo^{4+} is observed, indicating the MoS_2 is stoichiometric. Due to the strong overlapping of Mo $2p_{3/2}$ and shielding effect of MoS_2, only weak N 1s signal is detected.[20] Three types of N, i.e., pyridinic, pyrolic and graphitic N, are found at 397.1, 398.8 and 400.7 eV, respectively (Figure 7.4d).

The composition of the NDG/MoS_2 nanocomposites was determined by TGA, as shown in Figure 7.5. The contents of NDG and MoS_2 are 16 wt% and 84 wt%, respectively, assuming all the NDG is combusted in air while the MoS_2 is converted to MoO_3.

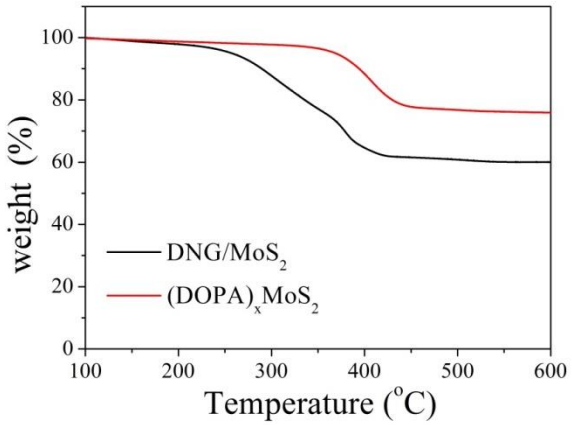

Figure 7.5 TGA curves of the $(DOPA)_xMoS_2$ and NDG/MoS_2.

7.3.3 Morphology of the NDG/MoS_2 heterostructure

The morphology of the NDG/MoS_2 nanocomposite was characterized by SEM and TEM. As shown in Figure 7.6a, the NDG/MoS_2 exhibits porous, distorted plate-like morphology. Each "plate" is comprised of numerous crumpled nanosheets with a thickness of less than 20 nm (Figure 7.6b). The morphology of NDG/MoS_2 is almost the same as that of $(DOPA)_xMoS_2$ (Figure 7.6c-d), indicating a good reservation of the layered structure during annealing. The absence of charging (without coating) indicates good electrical conductivity of the heterostructure. The TEM images of the NDG/MoS_2

are shown in Figure 7.7. The NDG/MoS_2 nanosheets are randomly scrolled and entangled with each other, showing typical morphology of 2D nanomaterials. The corrugation and scrolling increase the thermodynamic stability of the heterostructure and also allow the observation of the alternately stacked structure. Figure 7.7b shows a HRTEM image of a nanoflake with its basal plane in edge region parallel to the beam direction. It can be seen that dark and gray lines are alternately arranged at the edge of the nanoflake, which can be identified as MoS_2 and NDG, respectively, due to their difference in atomic number. This clearly verifies the well-defined alternating structure fabricated by this electrostatic attraction-induced self-assembly approach. The distance between adjacent MoS_2 monolayers is measured to be 0.98 nm, indicating the single-layered nature of MoS_2 with enlarged interlayer distance, in good consistence with the above XRD results. The NDG is almost parallel to the neighboring MoS_2, indicating the formation of NDG is confined in the 2D inter-layer space with MoS_2 monolayers as the template, therefore replicating the shape of MoS_2.

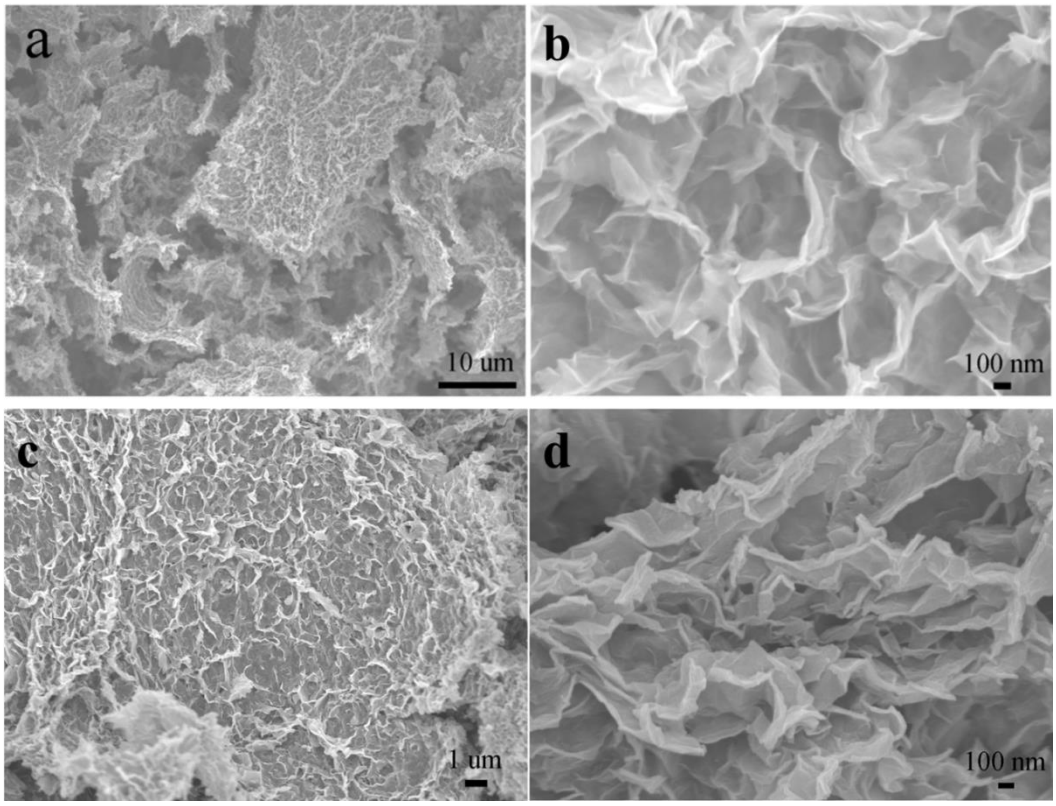

Figure 7.6 SEM images of the (a, b) NDG/MoS_2 and (c, d) $(DOPA)_xMoS_2$.

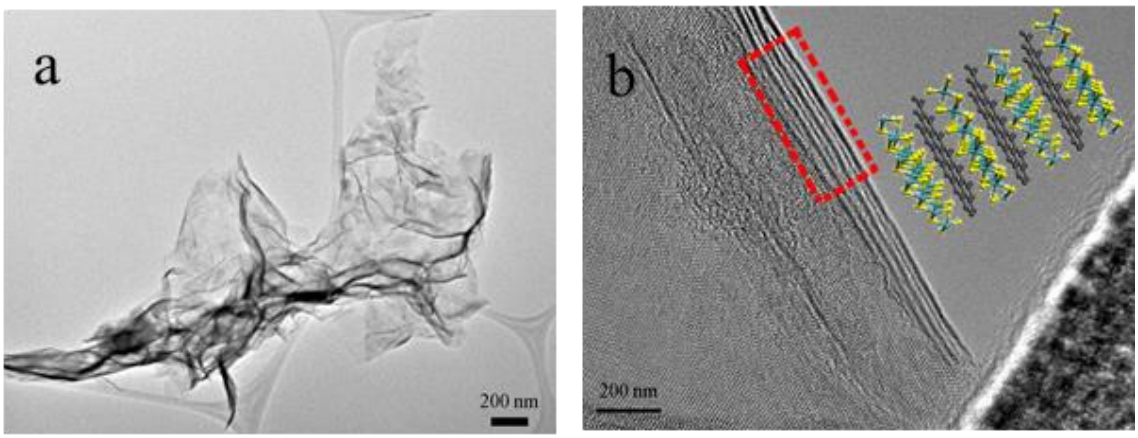

Figure 7.7 TEM images of the NDG/MoS_2 heterostructure.

To further confirm the formation of NDG from DOPA in the annealing process, the morphology of the NDG is investigated by dissolving NDG/MoS_2 in aqua regia. The successful removal of MoS_2 is confirmed by EDX (Figure 7.8), which shows negligible S and Mo contents after the aqua regia treatment. The morphology of the NDG is shown in Figure 7.9a. Though partially merged together due to the strong oxidation of aqua regia, the NDG still exhibits irregular sheet-like morphology with smooth surface, similar to that of graphene. Figure 7.9b shows a typical TEM image of a few partially overlapped flat NDG nanosheets with distinguishable edges, demonstrating their ultrathin nature.

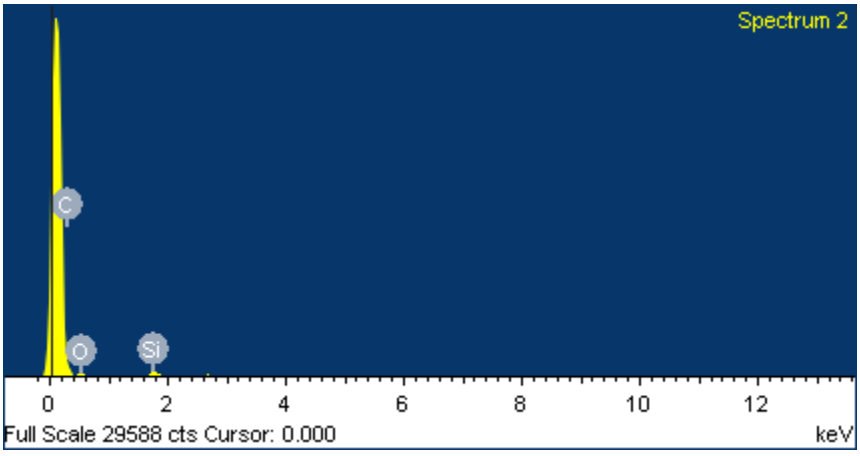

Figure 7.8 EDX spectrum of the NDG, showing negligible S and Mo contents after the removal of MoS_2.

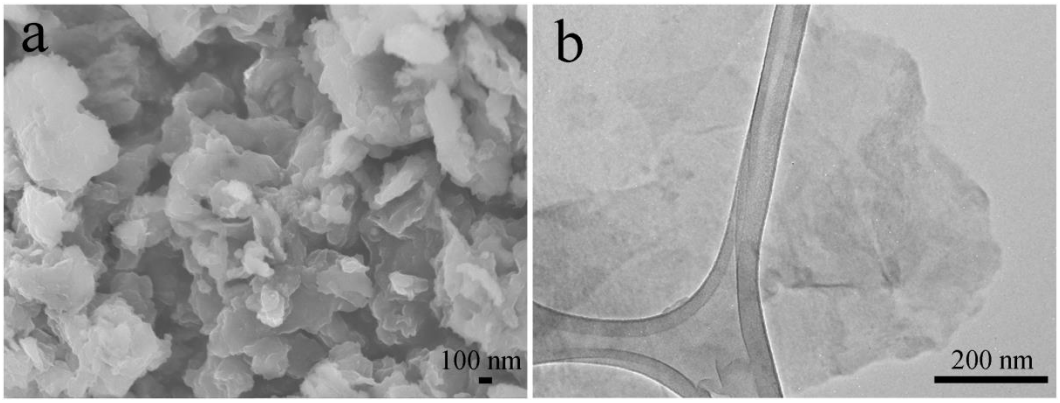

Figure 7.9 SEM and f) TEM images of the NDG after the removal of MoS_2 in in aqua regia.

7.3.4 Electrochemical performances of the NDG/MoS_2 heterostructure

The NDG/MoS_2 heterostructure was evaluated as an anode material for LIBs. Its lithiation/delithiation behaviors were firstly investigated via CV. As shown in Figure 7.10a, three reduction peaks are observed in the first cathodic scanning. The peak at 1.0 V is indicative of the formation of Li_xMoS_2, which decomposes into Mo nanoparticles embedded Li_2S matrix when further discharged, giving a cathodic peak at about 0.55 V. The slope starts from 0.8 V could be assigned to the insertion of extra Li^+ into the expanded interlayer space or the defects of MoS_2.[21,22] The formation of a SEI on the NDG is observed at 0.55 V, similar to that formed on reduced GO,[23,24] indicating their structural similarity. The capacity below 0.5 V is mainly attributed to the binding of Li^+ on the basal plane of the NDG nanosheets. During the anodic scanning, Li^+ stored on the surfaces of NDG are first released, giving a broad peak at about 1.2 V. The weak peak at 1.7 V is attributed to the partially oxidation of Mo to MoS_2.[25] The pronounced peak at 2.3 V is associated with the oxidation of Li_2S to sulfur. Therefore, the majority of MoS_2 is converted to sulfur and Mo after the first cycle. In the following scanning, the newly emerged cathodic peak at 1.9 V is indicative of the lithiation of S to Li_2S, while the anodic peak at 2.3 V remains, indicating the Li_2S/S couple dominates the redox process.

Figure 7.10b shows the galvanostatic discharge/charge curves of the NDG/MoS_2 anode for the 1st, 2nd, 5th, 10th and 50th cycles. The evolution of the plateaus matches well with the CV plot, indicating the redox reaction between Li^+ and S instead of MoS_2. The initial charge and discharge capacities are 750 and 1000 mAh/g, respectively, with a

Coulombic efficiency of 75%. The capacity loss is mainly caused by the formation of SEI film and the irreversible conversion from MoS_2 to Mo/Li_2S. After the first cycle, the reversible (charge) capacity quickly increases to 1040 mAh/g with Coulombic efficiency of above 97%. This quick stabilization can be attributed to the ultrathin nature of the NDG/MoS_2 heterostructure, which shortens the electron and Li^+ pathway and ensures complete lithiation/delithiation.

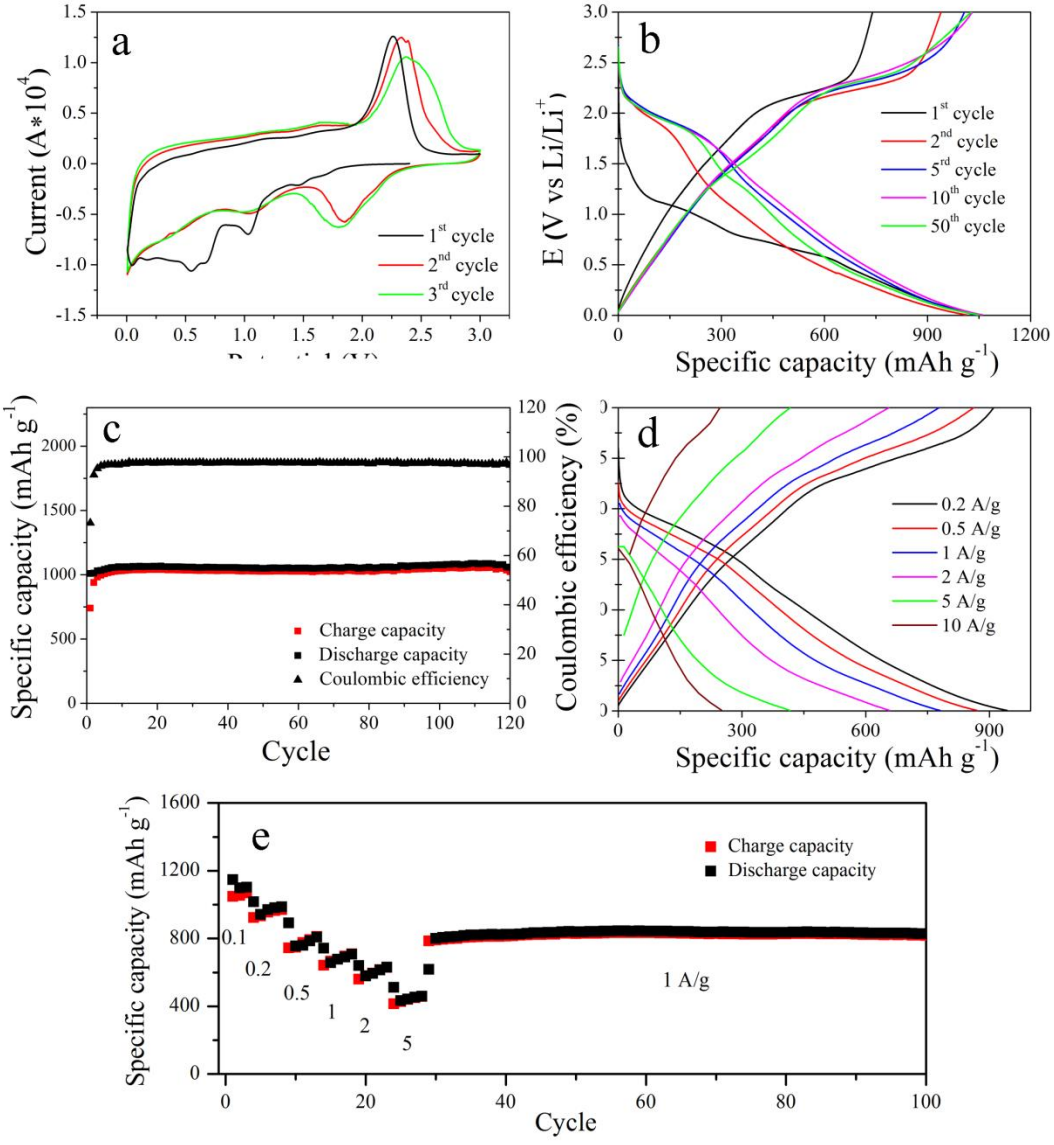

Figure 7.10 Electrochemical properties of the NDG/MoS_2 anode: (a) CV curve, (b) GCD profiles at 0.1 A/g, (c) cycling stability at 0.1 A/g, (d) rate profiles and (e) high rate capabilities at various current densities.

The pristine bulk MoS_2 exhibits rather poor cycling stability (Figure 5.8). The initial capacity is only 600 m Ah/g and the reversible capacity decreases quickly to 100 mAh/g after 50 cycles, with a capacity retention of only 17%. The lower conductivity and dissolution of polysulfide intermediates are believed to account for the lower activity and fast capacity decay, similar to that of the Li-S battery. Instead, excellent cycling stability is achieved for the NDG/MoS_2 anode, as shown in Figure 7.10c. A slightly increase in the reversible capacity is observed from the second cycle onward. This "activation" process is observed for all the samples tested and may be attributed to the cycling-induced penetration of electrolyte and expansion of defect sits and vacancies.[16,20,21,26] Clearly, the NDG/MoS_2 heterostructure can effectively alleviate the diffusion of soluble polysulfide, which could be ascribed to the physical protection and chemical adsorption functions of the NDG nanosheets. The MoS_2 monolayers are sandwiched between the neighboring NDG nanosheets. This face-to face intimate contact helps to confine the as-formed polysulfide within the framework. Moreover, doping of carbon with heteroatoms, nitrogen for example, could improve its interactions with the sulfur-containing species at the electron-modified interface.[27,28] Thus, the nitrogen atoms in the NDG may immobilize the polysulfide anions and hinder their diffusion, leading to higher sulfur utilization and cycling stability.

The rate capabilities of the NDG/MoS_2 anode are shown in Figure 7.10d-e. The reversible capacities at 0.1, 0.2, 0.5 1.0, 2.0, and 5.0 A/g are 1050, 970, 810, 700, 630, and 460 mAh/g, respectively, demonstrating superior rate performance. The reversible capacity fully rebounds (830 mAh/g) when the current density is reset to 1 A/g, indicating the robustness of the van der Waals heterostructure. The NDG/MoS_2 anode shows excellent high rate stability afterwards. The reversible capacity is still above 820 mAh/g till the 100^{th} cycle at 1A/g.

The superior rate and cycling performance is validated by the electrochemical impedance measurement, as shown in Figure 7.11a. The equivalent circuit model and fitted parameters are listed in Figure 7.12 and Table 7.1.[29] In comparison with the pristine MoS_2, the diameter of the semicircle at high/medium frequencies is greatly reduced for the NDG/MoS_2 anode before cycling, indicating its significantly lowered charge-transfer

resistance (R_{ct}) at the electrode-electrolyte interface. The Warburg impedance (Z_w), which is related to the solid-state diffusion resistance of Li^+, is also dramatically decreased as indicated by the larger slope of the oblique line at low-frequency. Therefore, a much improved electrochemical performance is expected because of the enhanced electron and Li^+ transport. A new semicircle appears at high frequency after cycling, which corresponds to the resistance (R_f) and constant phase element (CPE_2) of the SEI film. The total resistance, however, is almost unchanged, indicating the excellent cycling stability of the NDG/MoS_2 heterostructure.

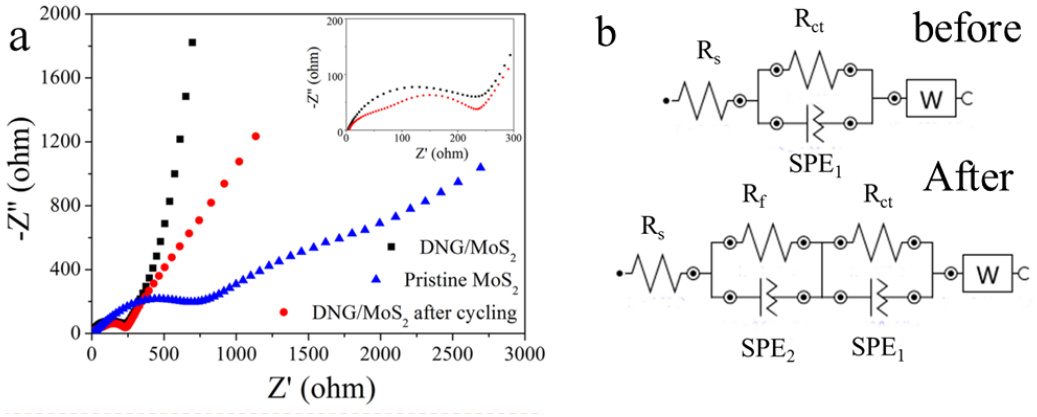

Figure 7.11 (a) Nyquist plots of the pristine MoS_2 and NDG/MoS_2 anode before and after cycling and (b) the equivalent circuit models of the Nyquist plots before and after cycling.

Table 7.1 Impedance parameters derived from Figure 7.11b.

Electrode	Rs (Ω)	Rf(Ω)	CPE2 (μF)	Rct (Ω)	CPE1 (μF)
Pristine MoS2 before cycling	5.86			773	25.5
NDG/ MoS2 before cycling	3.09			146	9.27
NDG/ MoS2 after cycling	4.58	72.2	8.91	107	18

Clearly, the excellent electrochemical performance of the NDG/MoS_2 anode could be attributed to its unique structure and the synergistic effect between the two components, as illustrated in Figure 7.12. Firstly, the *in-situ* formed NDG is intimately face-to-face contacted with the neighboring MoS_2 monolayers, which not only prevents the restacking of MoS_2, but also greatly enhances the electrical conductivity of the heterostructure. The

NDG serves as excellent conductive channels and transfers electrons to the MoS_2 monolayers, resulting in fast lithiation/delithiation kinetics. Moreover, the abundant MoS_2-NDG interfaces provide additional active sites for Li^+ storage, which contributes to the high reversible capacity. Secondly, the expanded interlayer spacing reduces the diffusion resistance of Li^+ into the interspace, thus ensuring sufficient utilization of MoS_2 with improved dynamics. Meanwhile, the voids between the NDG and MoS_2 accommodate the local volume expansion/contraction during cycling and protect the heterostructure from pulverization, increasing the long-term cycling stability of the MoS_2-NDG heterostructure even under high current densities. Thirdly, the NDG play dual functions in the alleviation of shuttle effect, thus overcoming the intrinsic capacity fading of the electrode. On one hand, the NDG nanosheets sandwich the MoS_2 monolayers and hence can act as physical barriers to confine the soluble "products" formed in charging/discharging processes not to diffuse into the electrolyte. On the other hand, owing to the improved interactions between the nitrogen atoms and sulfur containing species, the NDG can help to anchor the polysulfide anions at electron-modified interfaces by chemical adsorption. The above factors endow the unique NDG/MoS_2 van der Waals heterostructure with good conductivity, fast Li^+ diffusion, high sulfur utilization and structural robustness, resulting in its excellent cycling stability and rate capacities as an advanced anode for LIBs.

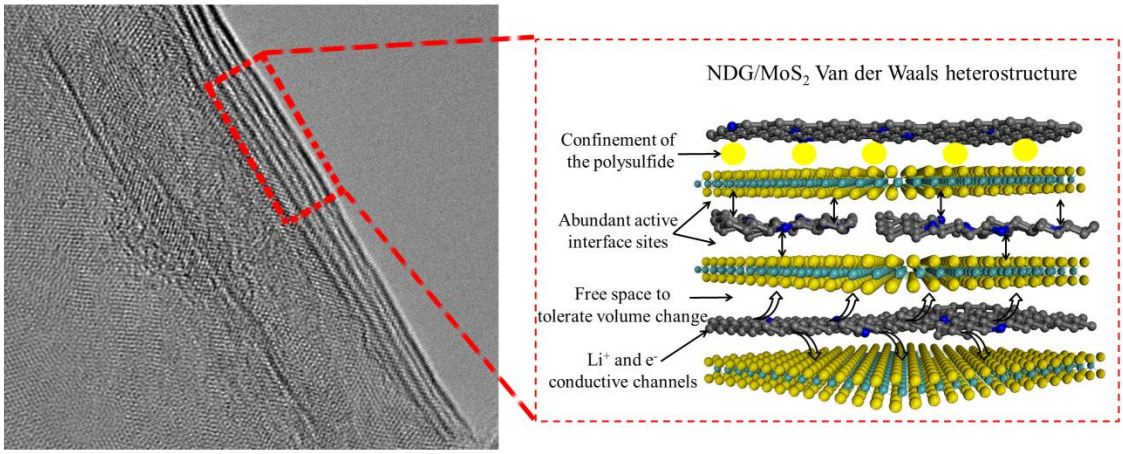

Figure 7.12 An illustration of the synergistic effect between the two components in the NDG/MoS_2 van der Waals heterostructure.

7.4 Conclusions

In this work, for the first time we demonstrate a facile self-assembly approach for synthesis of a novel NDG/MoS_2 van der Waals heterostructure. The *in-situ* formed NDG/MoS_2 nanosheets with an overall thickness of only ~8 nm are composed of alternately stacked NDG and MoS_2 monolayers. Thus, it is not only an excellent Li^+ and electron conductor, but also a good host to immobilize the soluble polysulfide anions. When studied as a LIB anode, the NDG/MoS_2 shows excellent rate capabilities and cycling stability. The reversible capacity is above 820 mAh/g at 1 A/g after high-rate charge-discharge. Moreover, this self-assembly approach may also be adopted for synthesis of other NDG-intercalated 2D materials. The corresponding van der Waals heterostructures may exhibit a variety of unique properties arising from the synergistic effect between the two components.

References:

[1] A. K. Geim and I. V. Grigorieva. *Nature*. **2013**, 499, 419-425.

[2] Y. Yao, L. Tolentino, Z. Yang, X. Song, W. Zhang, Y. Chen and C.-p. Wong. *Adv. Funct. Mater.* **2013**, 23, 3577-3583.

[3] K.-G. Zhou, N.-N. Mao, H.-X. Wang, Y. Peng and H.-L. Zhang. *Angew. Chem., Int. Ed.* **2011**, 50, 10839-10842.

[4] W. Liu, C. Zhao, R. Zhou, D. Zhou, Z. Liu and X. Lu. *Nanoscale*. **2015**, 7, 9919-9926.

[5] L. Yang, J. Kong, D. Zhou, J. M. Ang, S. L. Phua, W. A. Yee, H. Liu, Y. Huang and X. Lu. *Chem. - Eur. J.* **2014**, 20, 7776-7783.

[6] H. Lee, J. Rho and P. B. Messersmith. *Adv. Mater.* **2009**, 21, 431-434.

[7] L. Yang, W. A. Yee, S. L. Phua, J. Kong, H. Ding, J. W. Cheah and X. Lu. *RSC Adv.* **2012**, 2, 2208-2210.

[8] S. Hong, Y. S. Na, S. Choi, I. T. Song, W. Y. Kim and H. Lee. *Adv. Funct. Mater.* **2012**, 22, 4711-4717.

[9] J. Kong, W. A. Yee, L. Yang, Y. Wei, S. L. Phua, H. G. Ong, J. M. Ang, X. Li and X. Lu. *Chem. Commun.* . **2012**, 48, 10316-10318.

[10] W. Divigalpitiya, R. Frindt and S. R. Morrison. *Science*. **1989**, 246, 369-371.

[11] R. Bissessur and P. K. Liu. *Solid state ionics*. **2006**, 177, 191-196.

[12] K. E. Dungey, M. D. Curtis and J. E. Penner-Hahn. *Chem. Mater.* **1998**, 10, 2152-2161.

[13] L. Wang, Z. Xu, W. Wang and X. Bai. *J. Am. Chem. Soc.* **2014**.

[14] Y. Jing, Q. Pan, Z. Cheng, X. Dong and Y. Xiang. *Mater. Sci. Eng., B*. **2007**, 138, 55-59.

[15] Y. Li, Y. Xiang, X. Dong, J. Xu, F. Ruan and Q. Pan. *J. Solid State Chem.* **2009**, 182, 2041-2045.

[16] C. Zhao, J. Kong, L. Yang, X. Yao, S. L. Phua and X. Lu. *Chem. Commun.* . **2014**, 50, 9672-9675.

[17] H. Jiang, D. Y. Ren, H. F. Wang, Y. J. Hu, S. J. Guo, H. Y. Yuan, P. J. Hu, L. Zhang and C. Z. Li. *Adv. Mater.* **2015**, 27, 3687-3695.

[18] Z. Wang, T. Chen, W. Chen, K. Chang, L. Ma, G. Huang, D. Chen and J. Y. Lee. *J. Mater. Chem. A*. **2013**, 1, 2202-2210.

[19] Y. Zhang, K. Fugane, T. Mori, L. Niu and J. Ye. *J. Mater. Chem.* **2012**, 22, 6575-6580.

[20] K. Chang, D. Geng, X. Li, J. Yang, Y. Tang, M. Cai, R. Li and X. Sun. *Adv. Energy Mater.* **2013**, 3, 839-844.

[21] J. Xiao, X. Wang, X.-Q. Yang, S. Xun, G. Liu, P. K. Koech, J. Liu and J. P. Lemmon. *Adv. Funct. Mater.* **2011**, 21, 2840-2846.

[22] J. Xie, H. Zhang, S. Li, R. Wang, X. Sun, M. Zhou, J. Zhou, X. W. D. Lou and Y. Xie. *Adv. Mater.* **2013**, 25, 5807-5813.

[23] J. Kong, C. Zhao, Y. Wei, S. L. Phua, Y. Dong and X. Lu. *J. Mater. Chem. A*. **2014**, 2, 15191-15199.

[24] G. Wang, X. Shen, J. Yao and J. Park. *Carbon*. **2009**, 47, 2049-2053.

[25] L. Yang, S. Wang, J. Mao, J. Deng, Q. Gao, Y. Tang and O. G. Schmidt. *Adv. Mater.* **2013**, 25, 1180-1184.

[26] H. Hwang, H. Kim and J. Cho. *Nano Lett.* **2011**, 11, 4826-4830.

[27] H.-J. Peng, T.-Z. Hou, Q. Zhang, J.-Q. Huang, X.-B. Cheng, M.-Q. Guo, Z. Yuan, L.-Y. He and F. Wei. *Adv. Mater. Interfaces*. **2014**, 1, 1400227.

[28] F. Sun, J. Wang, H. Chen, W. Li, W. Qiao, D. Long and L. Ling. *ACS Appl. Mater. Interfaces*. **2013**, 5, 5630-5638.

[29] K. Chang and W. Chen. *J. Mater. Chem.* **2011**, 21, 17175-17184.

Chapter 8

Conclusions and Outlook

In this chapter, the thread running through the whole thesis is connected. Firstly, the findings presented in Chapter 4-7 are summarized to answer the questions raised in Chapter 1 (the original hypotheses) and the main conclusions are drawn. The key outcomes of this PhD work are then highlighted. In addition, the outlook and recommendations for future work are proposed. Some reconnaissance work that did not warrant a complete chapter are also included.

8.1 Conclusions

In this work, aimed to overcome the inherent weaknesses, sluggish kinetics and capacity fading of MoS_2-based anodes, and explore its potential as an alternative anode material for LIBs, factors that may affect the electrochemical performance of MoS_2, including layer numbers, interlayer distance, conductive additives (carbon) and crystal interfaces are investigated through a few novel morphology and structure design of MoS_2-based nanocomposites.

Firstly, the influence of layer numbers is studied in the work presented in chapter 4, utilizing AL as an exfoliation agent. It is verified that the addition of AL greatly increases the exfoliation efficiency and the stability of the MoS_2 dispersion. Bulk MoS_2 can be effectively exfoliated in aqueous solution via sonication with the assistant of AL. Stable multilayer MoS_2 dispersion are obtained with high concentration, which could be ascribed to the electrostatic repulsion and steric hindrance of the negatively charged AL macromolecules. When the exfoliated MoS_2 nanosheets are applied as electrode materials for LIBs, they show much improved electrochemical performance compared with the pristine MoS_2 mineral because of the enhanced ion and electron transfer kinetics, especially along the thickness direction. Due to the dissolution of polysulfide, however, the cycling stability of the exfoliated MoS_2 nanosheets is still not satisfied.

To address this issue, in the work described in chapter 5, thin MoS_2 nanoflakes encapsulated in carbon nanofibers were fabricated through electrospinning and carbonization. It is verified that the combination of 1D electrospinning-derived CNF with 2D thin MoS_2 nanosheets could be an effective way to overcome the shortcomings of MoS_2-based anodes. The carbon matrix enhances the conductivity of MoS_2, tolerates local volume change during cycling, and most importantly, confines the active materials within the carbon matrix from dissolution, as evidenced by the TEM observation after the cycling test. As a result, stable cycling performance is achieved for the MoS_2/C hybrid mat. The effect of interlayer spacing on the electrochemical performance of MoS_2 is investigated by comparing the specific capacities of the MoS_2 nanosheets and MoS_2 powder. Both electrodes suffered rapid capacity fading due to loss of active materials.

However, the MoS_2 nanosheets sample showed a higher capacity at all cycles, which could be ascribed, though not exclusive, to its larger interlayer spacing.

Advanced electrode materials require not only stable cycling performance, but excellent rate capability to meet the growing demand on fast charge and high power devices. The rate capability of the MoS_2/C hybrid mat, however, is limited by the relatively thick carbon shell and MoS_2 nanosheets. The Li^+ have to pass through the carbon "barrier" first before they reach the MoS_2 core, and the ionic and electronic conductivity of MoS_2 along the thickness direction is orders of magnitude lower than that alone the basal plane. To further enhance the performance of MoS_2-based electrodes, the SL-MoS_2 is an ideal candidate as it possesses the largest surface area, shortest diffusion length and abundant active sites. The integration of carbonaceous materials is also indispensable but the thickness of carbon phase should be carefully controlled. Due to its spontaneous restacking nature, however, the large-scale synthesis of SL-MoS_2/C is still not realized. The absorption of surfactants on the surface of MoS_2 or MoS_2 precursors can facilitate the formation of ultrathin MoS_2 nanosheets, typically few layers because of the weak van de Walls interaction.[1-4].

Enlightened by this, a complexation-assisted large-scale aqueous synthesis of SL-MoS_2/C sandwich structure is developed and used as advanced anode material for LIBs. It is verified the stable covalent bonds formed greatly restrict the growth of MoS_2 crystals. The coordination bonding formed between DOPA and Mo^{VI} is believed crucial for the formation of this novel sandwich structure, as the growth of MoS_2 is confined by this strong covalent bonding, giving small and disordered SL-MoS_2 crystals; while polydopamine in the vicinity is trapped in the van der Waals gap of MoS_2 and converted to carbon. As a result, SL-MoS_2/C with large interlayer spacing, sandwich structure and crumpled nanosheet morphology is obtained. These structural features render the SL-MoS_2/C excellent rate capability and cycle life as a LIB anode.

As a 2D material, the stacking of SL-MoS_2 with other atomic layers may generate a new class of 2D composite materials with fascinating properties.[5] In term of LIBs, graphene may be the best choice as it not only enhance the conductivity of MoS_2, but restrict the dissolution of polysulfide into the electrolyte. In chapter 7, a simple self-assembly

strategy for fabricating van der Waals heterostructures from isolated two-dimensional atomic crystals is presented. Specifically, DOPA, which serves as an excellent self-assembly agent and carbon precursor, is adsorbed on exfoliated MoS_2 monolayers through electrostatic interaction, and then the surface-modified monolayers self-assemble spontaneously into DOPA-intercalated MoS_2. The subsequent *in-situ* conversion of DOPA to highly conductive NDG in the interlayer space of MoS_2 leads to the formation of a novel NDG/MoS_2 nanocomposite with well-defined alternating structure. It is verified that this intimate "face-to-face" contact between MoS_2 and NDG trigger synergistic effects and maximize the Li^+ storage potential of both components when the NDG/MoS_2 is studied as an anode for LIBs. The results show that alternating arrangement of NDG and MoS_2 triggers synergistic effect between the two components. The kinetics and cycle life of the anode are greatly improved due to the enhanced electron and Li^+ transport as well as the effective immobilization of soluble polysulfide by NDG. A reversible capacity of more than 460 mAh/g could be delivered even at 5 A/g. Moreover, the abundant voids created at the MoS_2-NDG interface also accommodate the volume change during cycling and provide additional active sites for Li^+ storage. These endow the NDG/MoS_2 heterostructure with low charge-transfer resistance, high sulfur reservation and structural robustness, rendering it an advanced anode material for LIBs.

Table 8.1 The comparison of structure, method, performance and cost of MoS_2 nanostructures.

Structure	Method	Performance	Cost
MoS_2 nanosheets	Aqueous exfoliation and annealing	190 mAh/g at 1A/g Capacity fading	Low
oS_2/C hybrid mats	Hydrothermal, electrospinning and annealing	250 mAh/g at 1A/g Stable but low rate	
SL-MoS_2/C sandwich structure	Hydrothermal and annealing	675 mAh/g at 1A/g Stable and high rate	
NDG/MoS_2 heterostructure	Chemical-exfoliation, self-assembly and annealing	820 mAh/g at 1A/g Stable and high rate	High

For comparison, the structure, method, performance and cost of the MoS_2-based anodes are listed in Table 8.1. The objectives of this thesis are realized by engineering the morphology and structure of MoS_2. Compared to pristine MoS_2, which suffers sluggish

kinetics and capacity fading, the cycling and rate performance of MoS_2 can be greatly enhanced by reducing the number of layers, enlarging the interlayer distance, adding carbon additives and creating crystal interfaces.

8.2 Significant Contributions

This research also leads to several novel findings and outcomes.

Firstly, it is discovered for the first time that AL, a low-cost, environmentally benign and bio-renewable feedstock, is an excellent surfactant for direct aqueous exfoliation of 2D materials via sonication. Graphene, MoS_2, BN and WS_2 can be effectively exfoliated in water and stable dispersions with high concentrations can be obtained. This facile, scalable and eco-friendly aqueous-based process in combination with renewable and ultra-low-cost lignin opens up possibilities for large-scale fabrication of MoS_2 or other 2D-based nanocomposites and devices.

Secondly, highly flexible and free-standing nanofibrous mats are produced by combining 1D electrospinning-derived CNF with 2D thin MoS_2 nanosheets. The hybrid mats the highly flexible and can maintain the structural integrity even after repeated bending, enabling the realization of low-cost, light weight and flexible devices.

Thirdly, a DOPA-Mo^{VI} complexation-assisted approach for large-scale aqueous synthesis of SL-MoS_2/C is developed for the first time. The important implication of this work is that the formation of complex (strong coordination bonding) between DOPA and MoS_2 precursor can greatly restrict the growth of MoS_2 crystals and benefits the formation of highly disordered SL-MoS_2. Furthermore, this method may be extended to prepare a many other metal oxide/sulfide and carbon nanocomposites, where defect-rich and ultrafine crystals are crucially needed.

Finally, the presence of atomic interfaces is believed playing an important role in Li^+ storage. In this regard, the stacking of MoS_2 with graphene is an ideal superstructure for maximizing its electrochemical performance. Different from the approaches reported by other groups, in this work, an electrostatic attraction-induced self-assembly strategy is adopted for the fabrication of MoS_2-based van der Waals heterostructures. This novel

self-assembly approach is facile and scalable, and may be applied to other systems for surface modification of MoS_2 or fabrication of MoS_2-based nanocomposites. Other than LIBs, such novel nanocomposites with unique alternating structure may be good candidate materials for other electrochemical applications.

8.3 Reconnaissance Results and Future works

8.3.1 Cathode

Although most of the current work on MoS_2 for LIBs is focused on the use of MoS_2 as anodes, MoS_2 cathode is an emerging and highly promising area that needs to be paid special attention.[6] Compared to $LiCoO_2$, the MoS_2 cathode (without modification) may offer little in the way of capacity enhancement. However, the material is still worth considering because of its good rate performance and cycling stability. What's more, the electrochemical performance could be much enhanced through proper morphology and structure design, just as what presented above for anodes. As a demonstration, the AL exfoliated MoS_2 nanosheets (chapter 4) were tested between 1-3V as the cathode and the results are shown blow.

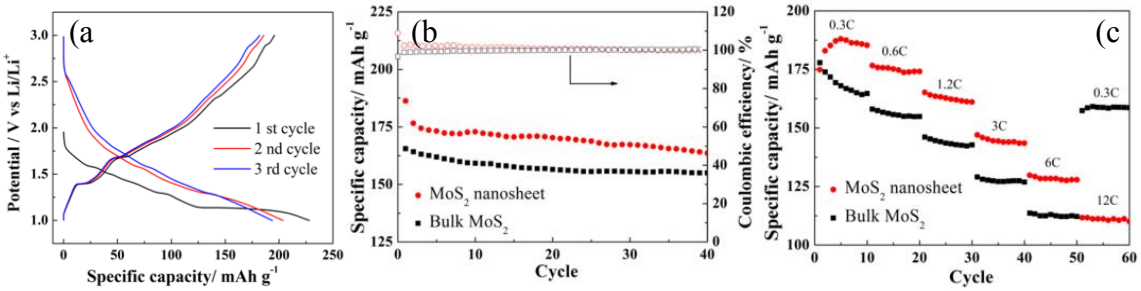

Figure 8.1 (a) discharge-charge profiles at 0.1C, (b) cycling performance at 0.6C and (c) rate capabilities of the exfoliated MoS_2 nanosheets between 1-3V (carbon black 30 wt%).

The first 3 discharge-charge curves in the potential range between 1 and 3V were shown in Figure 8.1a. The electrode contains 60wt% of AL exfoliated MoS_2 nanosheets, 30wt% carbon black and 10wt% PVDF. The initial charge capacity is 196 mAh/g at 0.1C (1C = 167 mAh/g) with a Coulombic efficiency as high as 85%. In the following cycles, the efficiency quickly stabilized at 100% and a reversible capacity of 164 mAh/g is reached at the 40^{th} cycle (Figure 8.1b). The exfoliated MoS_2 nanosheets exhibit excellent rate

capability compare to its bulk counterpart (Figure 8.1c). The reversible capacities at 0.3C, 0.6C, 1.2C, 3C and 6C are 185, 175, 160, 144 and 128 mAh/g, respectively. The capacity maintains above 110 mAh/g even at 12C, which is 60% retention of the highest capacity corresponding to 3 min charge/discharge. This outstanding performance could be explained by the ultra-thin nature of MoS_2 nanosheet, which greatly increases the contact surface area with electrolyte and shortens the electron and ion migration length. The relatively smaller lateral size of MoS_2 nanosheets may also contribute to the high capacity and rate capability because more edge sulfur atoms are exposed as redox centers. The variation in electrode composition has little effect on the electrochemical performance, as shown in Figure 8.2. For the electrode contains only 10 wt% of carbon black, the reversible capacity is still above 110 mAh/g at 1C after 100 cycles (Figure 8.2a). Excellent rate capability can also be achieved (Figure 8.2b). Given the facile and scalable fabrication process, it is believed that this exfoliated MoS_2 nanosheet could be a promising cathode material for low-cost LIBs.[6] Further attempts may be focused on the surface medication with conducting agents, combination with other cathode materials, expansion of the interlayer spacing, etc.

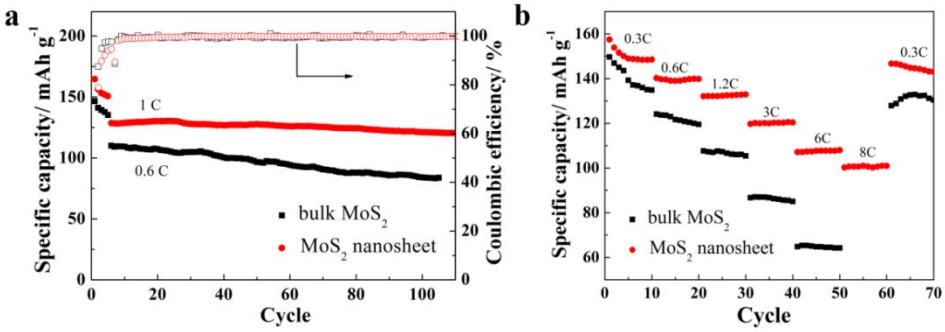

Figure 8.2 (a) Cycling stability and (b) Rate capabilities of the AL exfoliated MoS_2 nanosheets between 1-3V with a carbon black content of 10 wt%.

8.3.2 Flexible electrode

As mentioned above, the electrospinning-derived MoS_2/C hybrid mats exhibit high potential as flexible electrodes. This not only benefits from the electrospinning technique, but from the nature of MoS_2 (layered structure with excellent lubricant property). As a 2D layer material, the membrane composed of random orientated MoS_2 nanosheets is able to

resist a certain deformation due to the relative movement between the nanosheets, similar to that of graphene membrane. What is more, the external stress can also be released through the slip of layers. However, the mechanical strength of the MoS_2 membrane is poor, probably because of the lack of interactions and relatively small dimensions, which limits its practical application. To prepare robust MoS_2 membranes, some pioneer works have been done, including mixing with other rigid materials and compressing on flexible substrates,[7-9] which showed promise in the enhancement of flexibility. With the popularity of flexible and wearable electronic devices, I believe the MoS_2-based flexible electrode will be a hot research topic.

8.3.3 Other electrochemical applications

8.3.3.1 Sodium ion battery

Beyond LIBs, the unique properties of MoS_2 make it a versatile material which enables its use in a wide range of scientific fields. Because of the insufficient reserve and safety issue of lithium, plenty of research has turned to other batteries system. Sodium ion battery (SIB) is one of them. The operating principle of SIB is similar to that of LIBs, except the replacement of Li^+ with Na^+. The ionic radius of sodium, however, is 34% (0.102 nm) larger than that of lithium (0.076 nm). As a result, electrode materials are required to possess larger channels or sites for Na^+ storage. For example, the commercial Li+ anode, graphite, which has a theoretical capacity of 372 mAh/g to Li^+ (LiC_6), barely reacts with Na^+ and delivers a capacity of only 32 mAh/g based on NaC_{70}. Compare to other materials, the 2D layered structure of MoS_2 and its large interlayer spacing (0.62nm) make it a very good candidate for SIBs. The intensive research on LIBs also indicates the highly reversible property of the MoS_2 electrode. As a demonstration, the effect of layer numbers on the SIB performance is investigated by employing the AL exfoliated MoS_2 nanosheets.

As shown in Figure 8.3, the cell exhibits excellent rate and cycling stability between 0.01 -2.7 V vs Na/Na^+. Reversible capacities of 280, 260, 230, 180, 125 mAh/g can be reached at 50, 100, 200, 500 and 1000 mAh/g, respectively. After 50 cycles, the capacity is still above 210 mAh/g. When the content of carbon black is lowered to 10 wt%, the cell shows similar rate and cycling capabilities. A sudden change in current density (50 to 1000 mAh/g) will not damage the structure

of the MoS_2 nanosheet, indicating excellent rate retention. Similar to the LIBs, the electrochemical performance of MoS_2-based anode could be improved through novel morphology and structure design, while the effect of interlayer spacing may be critical because of the large ionic radius of Na^+.

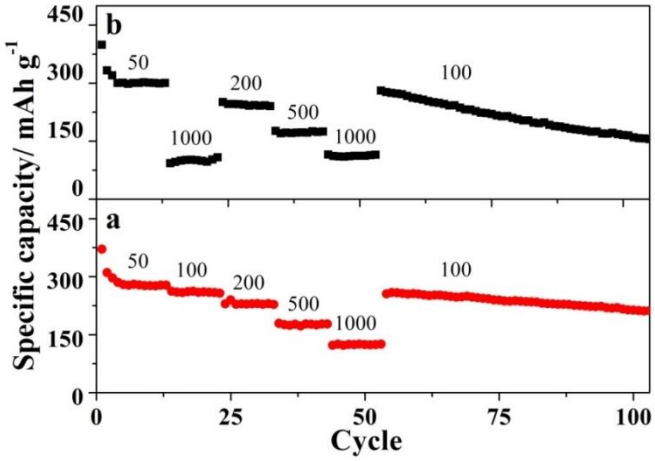

Figure 8.3 The rate and cycling performances of the exfoliated MoS_2 nanosheets in sodium ion batteries with (a) 10 wt% and (b) 30 wt% of carbon black.

8.3.3.2 Supercapacitor

Supercapacitors, which exhibit relatively high power density and long cycle life, are effective complements to batteries in energy storage. Recently, metallic 1T phase MoS_2 nanosheets were explored as supercapacitor electrode materials and exhibited much enhanced electrochemical response.[10] Compared to 2H-MoS_2, the 1-T phase is hydrophilic and 10^7 times more conductive, making it a better candidate for high performance supercapacitors.

In chapter 7, we develop a self-assembly strategy to fabricate the MoS_2-based nanocomposites. Here, as a demonstration, nanosheets composed of alternately stacked metallic 1T MoS_2 and polyaniline monolayers were fabricated using the same strategy for supercapacitor allocation. The chemical exfoliated SL-MoS_2 was first mixed with PANI solution followed by acidification. The colour of the mixture became dark green, indicating the successful doping of PANI with HCl. The colloidal suspension was destabilized due to the electrostatic attraction between SL-MoS_2 and the NH_2^+ group of

PANI, causing flocculation of the mixture, during which PANI was sandwiched between SL-MoS_2, forming the alternating structure.

The morpholoy and structure of the PANI-MoS_2 nanocomposites are shown in Figure 8.4. As shown in Figure 8.4a, the SL-MoS_2 and PANI monolayers stack together, forming thin nanosheets due to the neutralization of surface charges. The number of layers can be discerned from the edge of the nanosheets (Figure 8.4b). From the side view, it is striking to see that the nanosheets indeed consist of well-defined alternately stacked SL-MoS_2 and PANI monolayers. The outer surface of the nanosheets is covered by a thin layer of PANI. An enlargement of Figure 8.4b clearly shows that PANI monolayers (light grey line) are sandwiched by MoS_2 (dark line). The intercalation of PANI is also confirmed by XRD, as shown in Figure 8.4c. The *(002)* moves to a much lower angle ($2\theta = 8.1^{o}$), indicating an expansion of 0.47 nm of the interlayers spacing.

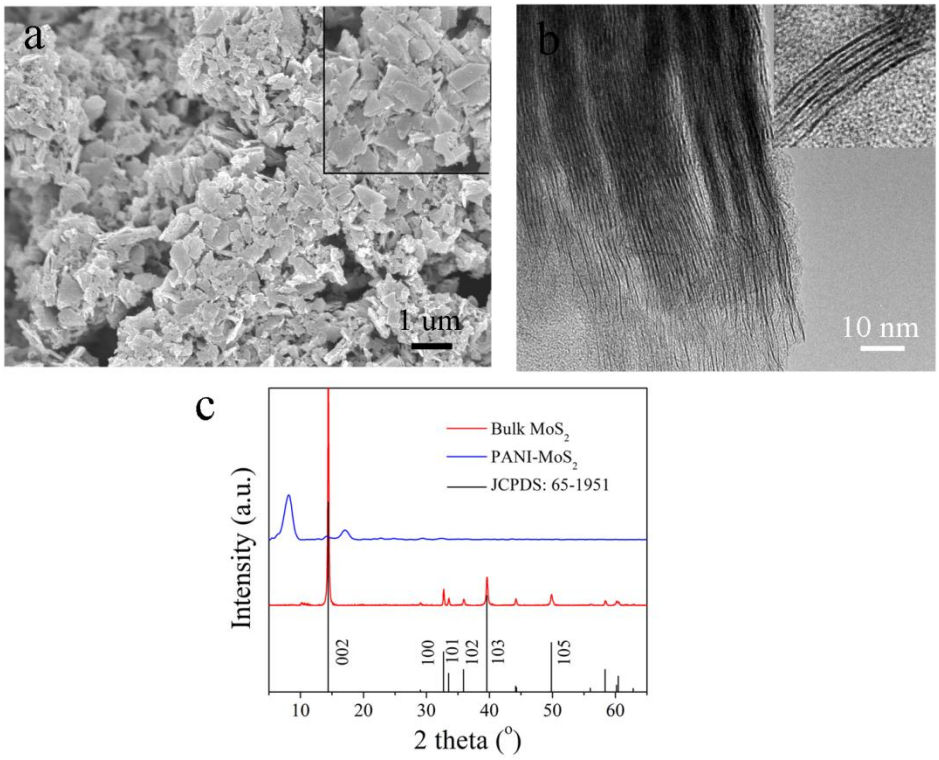

Figure 8.4 (a) SEM, (b) TEM and (c) XRD of the PANI-MoS_2 nanocomposites.

The electrochemical properties of the PANI-MoS_2 were evaluated by CV and GCD, as shown in Figure 8.5. A redox pair located at around 0.1 and 0.25 V is observed, which could be attributed to the emeraldine/leucoemeraldine transformation of PANI.[11] The

voltage gaps of the redox pair increase slightly with the scan rate, while the shapes of CV curve are well maintained. For GCD tests (Figure 8.5b), no obvious voltage drops are observed, indicating very small internal resistance. The specific capacitances at 0.5, 1, 2, 5, 10, 20 A/g are 470, 440, 370, 340, 310 F/g, respectively, demonstrating excellent rate capabilities. In the next step, the long cycling stability of the PANI-MoS_2 nanocomposites will be evaluated. The effect of composition variation on the capacitance will also be investigated to optimize the electrochemical performance.

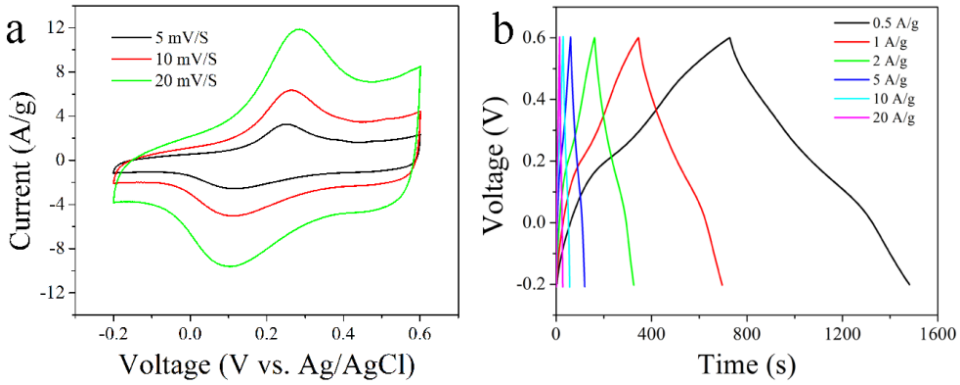

Figure 8.5 (a) CVs at scan rates of 5, 10 and 20 mV/s and (b) GCD from 0.5 to 20 A/g of the PANI-MoS_2 nanocomposites.

References:

[1] Z. Wang, T. Chen, W. Chen, K. Chang, L. Ma, G. Huang, D. Chen and J. Y. Lee. *J. Mater. Chem. A.* **2013**, 1, 2202-2210.

[2] L. Ma, J. Ye, W. Chen, D. Chen and J. Yang Lee. *Nano Energy*. **2014**, 10, 144-152.

[3] G. Huang, T. Chen, W. Chen, Z. Wang, K. Chang, L. Ma, F. Huang, D. Chen and J. Y. Lee. *Small*. **2013**, 9, 3693-3703.

[4] K. Chang and W. Chen. *Chem. Commun.* . **2011**, 47, 4252-4254.

[5] A. K. Geim and I. V. Grigorieva. *Nature*. **2013**, 499, 419-425.

[6] T. Stephenson, Z. Li, B. Olsen and D. Mitlin. *Energy Environ. Sci.* **2014**, 7, 209-231.

[7] Y. Yang, H. Fei, G. Ruan, C. Xiang and J. M. Tour. *Adv. Mater.* **2014**, 26, 8163-8168.

[8] Y.-T. Liu, X.-D. Zhu, Z.-Q. Duan and X.-M. Xie. *Chem. Commun.* . **2013**, 49, 10305-10307.

[9] J. Z. Wang, L. Lu, M. Lotya, J. N. Coleman, S. L. Chou, H. K. Liu, A. I. Minett and J. Chen. *Adv. Energy Mater.* **2013**, 3, 798-805.

[10] M. Acerce, D. Voiry and M. Chhowalla. *Nat. Nanotechnol.* **2015**, 10, 313-318.

[11] Q. Wu, Y. Xu, Z. Yao, A. Liu and G. Shi. *ACS nano*. **2010**, 4, 1963-1970.

List of publications:

1. **Zhao, C**.; Wang, X.; Kong, J.; Ang, J. M.; Lee, P. S.; Liu, Z.; Lu, X*. Self-Assembly-Induced Alternately Stacked Single-Layer MoS_2 and N-doped Graphene: A Novel van der Waals Heterostructure for Lithium-Ion Batteries. ***ACS Appl. Mater. Interfaces*** 2016, 8, 2372.
2. Liu, W.#; **Zhao, C**.#; Zhou, R.; Zhou, D.; Liu, Z.; Lu, X*. Lignin-assisted Exfoliation of Molybdenum Disulfide in Aqueous Media and its Application in Lithium Ion Batteries. ***Nanoscale*** 2015, 7, 9919. (Co-first author)
3. Kong, J.#; **Zhao, C**.#; Wei, Y.; Phua, S.; Dong, Y; Lu, X*. Nanocups-on-Microtubes: a Unique Host towards High-Performance Lithium Ion Batteries. ***J. Mater. Chem. A*** 2014, 2, 15191. (Co-first author)
4. **Zhao, C**.; Kong, J.; Yao, X.; Tang, X.; Dong, Y.; Phua, S. L.; Lu, X*. Thin MoS_2 Nanoflakes Encapsulated in Carbon Nanofibers as High-performance Anodes for Lithium-ion Batteries. ***ACS Appl. Mater. Interfaces*** 2014, 6, 6392
5. **Zhao, C**.; Kong, J.; Yang, L.; Yao, X.; Phua, S.; Lu, X*. The Dopamine-Mo^{VI} Complexation-assisted Large-scale Aqueous Synthesis of a Single-layer MoS2/Carbon Sandwich Structure for Ultrafast, Long-life Lithium-ion Batteries. ***Chem. Commun.*** 2014, 50, 9672.